

Scalable integration of 2D semiconductors into photonic systems

Dissertation
zur Erlangung des akademischen Grades
Dr. rer. nat.

eingereicht an der
Mathematisch-Naturwissenschaftlich-Technischen Fakultät
der Universität Augsburg

von

Sebastian Hammer

Augsburg, Dezember 2019

Erstgutachter: Prof. Dr. Hubert J. Krenner
Zweitgutachter: apl. Prof. Dr. Helmut Karl
Datum der mündlichen Prüfung: 6. März 2020

Abstract

After the great success of graphene in the field of electronics, the class of monolayer transition metal dichalcogenides (TMDs) has gained significant impact in the field of photonics due to their direct bandgap. Transparency and mechanical flexibility of two-dimensional (2D) semiconductors as well as other unique TMD properties like non-linearity and enormous spin-orbit splitting promise an extensive amount of possible applications. The latter, in particular, has become of great interest in the field of spin- and valleytronics. We demonstrate the scalable integration of monolayer TMDs into two different kinds of optical devices.

In the first part of this thesis, we demonstrate selective enhancement of monolayer molybdenum disulfide (MoS_2) photoluminescence (PL) in hybrid, free-standing, one-dimensional (1D) photonic crystal cavities. These are based on a SiO_2 platform with chemical vapor deposition (CVD)-grown monolayer MoS_2 on top. The cavity in these “ladder-shaped” devices is realized by a gradual period decrease in the center of the device. In micro-photoluminescence (μ -PL) spectroscopic measurements, we observe three distinct modes at the majority of the investigated devices, that show a strong transverse-electric (TE) polarization and good spatial confinement. With an increase of the crystal period, we are able to tune the mode wavelength within the whole MoS_2 PL bandwidth. At larger periods $p > 285 \text{ nm}$, we even observe a fourth mode emerging at small wavelengths within the emission spectrum. Almost every investigated mode exhibits a quality factor between 1000 and 4000. All findings are in good agreement with finite-difference time-domain (FDTD) simulations.

In the second part of this thesis, we employ temperature as a further control parameter by introducing the phase change material vanadium dioxide (VO_2), which is applicable to a variety of different devices. VO_2 is a solid that switches from an insulating to a semi-conducting phase at a critical temperature of 68°C . If VO_2 material is present in form of nanoclusters, this temperature varies. Moreover, it depends on the initial phase, which causes a large temperature dependent hysteresis ($> 50^\circ\text{C}$) in phase-sensitive observables. This is, for example, applicable to the refractive index. We demonstrate refractive index temperature control by manipulating the focusing abilities of so-called Fresnel zone plate (FZP) lenses fabricated from VO_2 nanoclusters. FZP lenses are devices that are closely related to the field of “flat optics” and consist of concentric rings of well-defined width (the Fresnel zones) and alternating opacity. The blocking of destructively interfering components of an incident plane wave yields a focusing effect only by diffraction. In our experiments, FZP lenses are illuminated by off-chip LEDs as well as on-chip monolayer

MoS₂ PL emission. In order to fabricate temperature-sensitive FZP lenses, we deactivate the VO₂ nanoclusters in every second Fresnel zone, leaving the residual zones active. During illumination at wavelengths in the infrared and red regime, we observe distinct changes in the lenses' focusing behavior emerging at the critical temperature, which allow the precise reproduction of a temperature dependent hysteresis curve. We find these changes in the interference patterns in agreement with FDTD simulations. Furthermore, we achieve on-chip MoS₂ PL focusing. Although some effects emerge at on-chip illumination that are not completely understood, we are able to demonstrate proof-of-principle temperature dependent contrast changes between interference maxima and minima and to reproduce a hysteresis curve.

Zusammenfassung

Nach dem großen Erfolg von Graphen auf dem Gebiet der Elektronik hat die Klasse der monolagigen Übergangsmetall-Dichalcogenide (TMDs) signifikanten Einfluss im Bereich der Photonik gewonnen. Transparenz und mechanische Flexibilität zweidimensionaler (2D) Halbleiter sowie weitere einzigartige TMD-Eigenschaften wie Nichtlinearität und eine immense Spin-Bahn-Aufspaltung versprechen weitreichende Anwendungsmöglichkeiten. Insbesondere letztere Eigenschaft hat auf dem Gebiet der Spin- und Valleytronik großes Interesse geweckt. Wir demonstrieren die skalierbare Integration von TMD-Monolagen in zwei verschiedenen Arten optischer Bauteile.

Im ersten Teil dieser Arbeit zeigen wir eine selektive Erhöhung der Photolumineszenz (PL) von Molybdändisulfid (MoS_2) in hybriden, freistehenden, eindimensionalen photonischen Kristallkavitäten. Diese basieren auf einer Siliziumdioxid (SiO_2)-Plattform, auf die eine MoS_2 -Monolage mittels chemischer Gasphasenabscheidung (CVD) aufgewachsen ist. Die Kavität dieser „leiterartigen“ Strukturen ist durch eine gradielle Periodenverkleinerung in der Mitte des Kristalls realisiert. In Mikrophotolumineszenz (μ -PL)-Spektroskopie-Messungen beobachten wir drei deutliche Moden bei einem Großteil der untersuchten Kristalle, die sowohl eine starke transversal-elektrische Polarisierung als auch räumliche Einschränkung aufweisen. Durch eine Vergrößerung der Kristallperiode ist es möglich, die Modenwellenlänge auf der gesamten Bandbreite des MoS_2 -PL-Spektrums durchzustimmen. Bei größeren Perioden $p > 280 \text{ nm}$ beobachten wir sogar eine vierte Mode, die im kurzwelligen Bereich des Emissionsspektrums auftaucht. Fast jede untersuchte Mode weist einen Gütefaktor zwischen 1000 und 4000 auf. Alle Ergebnisse befinden sich in guter Übereinstimmung mit Simulationen, die mithilfe der Finite-Differenzen-Methode im Zeitbereich (FDTD) durchgeführt worden sind.

Im zweiten Teil dieser Arbeit verwenden wir die Temperatur als weiteren Kontrollparameter, indem wir das Phasenwechselmaterial Vanadiumdioxid (VO_2) einführen, welches in einer Vielzahl von Bauteilen eingesetzt werden kann. VO_2 ist ein Feststoff, der bei einer kritischen Temperatur von $68 \text{ }^\circ\text{C}$ von einer isolierenden in eine halbleitende Phase übergeht. Wenn das Material in Form von Nanokristalliten vorliegt, verändert sich diese Temperatur. Zudem hängt sie von der Anfangsphase ab, wodurch eine große temperaturabhängige Hysterese ($> 50 \text{ }^\circ\text{C}$) in phasensensitiven Observablen erzeugt wird. Dies trifft zum Beispiel auf den Brechungsindex zu. Wir demonstrieren die temperaturgetriebene Kontrolle des Brechungsindex durch die Manipulation des Fokussierungsvermögens sogenannter Fresnel'scher Zonenplatten (FZP)-Linsen, hergestellt aus Vanadiumdioxid-Nanokristalliten. FZP-Linsen gehören zur Gruppe der „flachen optischen Bauteile“ und

bestehen aus konzentrischen Ringen bestimmter Breite (den Fresnel-Zonen) und alternierender Opazität. Die Abschirmung destruktiv interferierender Komponenten einer einfallenden ebenen Welle führt zu einem Fokussierungseffekt, der allein auf Beugung beruht. In unseren Experimenten werden FZP-Linsen sowohl durch LEDs außerhalb des Chips beleuchtet als auch durch PL-Emission durch monolagiges MoS₂ auf dem Chip. Um temperatursensitive FZP-Linsen herzustellen, deaktivieren wir die VO₂-Nanokristallite in jeder zweiten Fresnel'sche Zone, wobei die restlichen Zonen aktiv bleiben. Bei der Beleuchtung im infraroten und roten Wellenlängenbereich beobachten wir deutliche Veränderungen im Fokussierungsverhalten der Linsen bei der kritischen Temperatur, die die präzise Reproduktion einer temperaturabhängigen Hysteresekurve erlauben. Diese Veränderungen im Interferenzmuster finden wir in Übereinstimmung mit FDTD-Simulationen. Außerdem erzielen wir eine PL-Fokussierung des auf dem Chip integrierten MoS₂. Obwohl einige Effekte, die bei der Beleuchtung durch integriertes MoS₂ auftreten, noch nicht vollständig verstanden sind, ist es uns möglich, temperaturabhängige Kontrastveränderungen zwischen Maxima und Minima zu messen und eine Hysteresekurve zu reproduzieren.

Contents

Abstract	i
Zusammenfassung	iii
1. Introduction	1
2. Fundamentals	5
2.1. 2D Transition metal dichalcogenides	5
2.2. Photonic crystal cavities	12
2.2.1. Photonic crystals	12
2.2.2. Defects in photonic crystals	15
2.2.3. Characterization of optical modes	17
2.3. Optical coupling	18
2.4. Vanadium dioxide - a phase change material	19
2.4.1. Vanadium dioxide nanoclusters	22
2.5. Fresnel zone plates	25
3. Methods	29
3.1. FDTD Simulation	29
3.1.1. Photonic crystal cavities	30
3.1.2. Fresnel zone plates	33
3.2. Fabrication	35
3.2.1. Chemical vapor deposition	35
3.2.2. Electron beam lithography	38
3.2.3. Reactive ion etching	40
3.2.4. Silicon etching	42
3.2.5. Ion implantation	43
3.3. Optical measurements	45
3.3.1. Photoluminescence spectroscopy	45
3.3.2. Raman spectroscopy	49
3.3.3. Direct transmission measurements	55
4. Photonic crystal cavities	57
4.1. Fabrication of hybrid devices	58
4.2. Optical mode characterization	61
4.3. Geometric mode tuning	66

4.4. Conclusion	67
4.5. Outlook	69
5. Tunable Metasurfaces	75
5.1. Fabrication of hybrid devices	75
5.2. Optical measurements	79
5.3. Measurement results	81
5.3.1. Infrared LED illumination	82
5.3.2. Red LED illumination	84
5.3.3. Molybdenum disulfide photoluminescence illumination	87
5.4. Conclusion	93
5.5. Outlook	94
6. Conclusion and Outlook	97
A. Appendix	99
A.1. Fabrication parameters	99
A.2. PCC sample layout	102
A.3. Type 2 Fresnel zone plate lenses	102
Bibliography	105
Acronyms	121

1 | Introduction

In recent years, 2D semiconductors have become of great interest in the field of optoelectronics. They are part of the so-called van-der-Waals (vdW) materials, that consist of individual one or few atoms thin layers that are weakly bonded by vdW attraction. Their probably most prominent and most studied representative is graphene, which is of major interest for electronic applications due to its extremely high charge carrier mobilities [1, 2]. Its zero electron volt (eV) bandgap, however, makes it less interesting for optical applications. Fortunately, there is an entire class of vdW materials that show a finite bandgap which becomes even direct when thinned down to a monolayer. The most prominent materials among this group are transition metal dichalcogenides (TMDs) with the structure formula MX_2 , consisting of a transition metal M like molybdenum (Mo) or tungsten (W) and two chalcogen atoms X like sulfur (S), selenium (Se), or tellurium (Te).

From micro-electronics' point of view, these ultrathin materials are extremely interesting for flexible and transparent electronic circuits [3, 4] and they naturally define the limits of miniaturization in, at least, one dimension. Additionally, their unique optical properties make them highly attractive for opto-electronic applications like single photon sources [5–9], light-emitting diodes (LEDs) [10], photo detectors [11, 12], solar cells [13, 14], plasmon sources [15, 16], and pump sources for optical resonators [17–22] and lasers [23–27]. As non-linear crystals, they are even applicable for second harmonic generation [28–31].

Due to their direct bandgap, TMDs monolayers show a strong photoluminescence (PL) emission of internal quantum efficiencies up to 45 % at 83 K or 8.3 % at room temperature [32]. Depending on the components, the bandgap ranges from energies in the visible spectrum to the near infrared regime. Alloys of more than two components with varying ratios, e. g. $\text{MoS}_{2(1-x)}\text{Se}_{2x}$, even allow us to carefully tune the emission frequency [33]. Additionally, TMDs show a large spin-orbit coupling [34] that leads to two different kinds of valleys in the band structure with opposite angular momentum and, thus, opposite helicity of their photoluminescence. These unique properties can be exploited in the fields of valleytronics and spintronics to independently populate and read-out different spin states [35–38].

Of capital importance for the integration of 2D materials into state-of-the-art on-chip optical technology is their scalable fabrication and their integration into established material systems in the silicon industry. Although the first 2D materials were fabricated by top-down methods like exfoliation [39, 40], bottom-up techniques like CVD have emerged

being able to provide wafer-scale monolayer films [41–47]. Depending on the method you choose, the device fabrication has to be accomplished in different order.

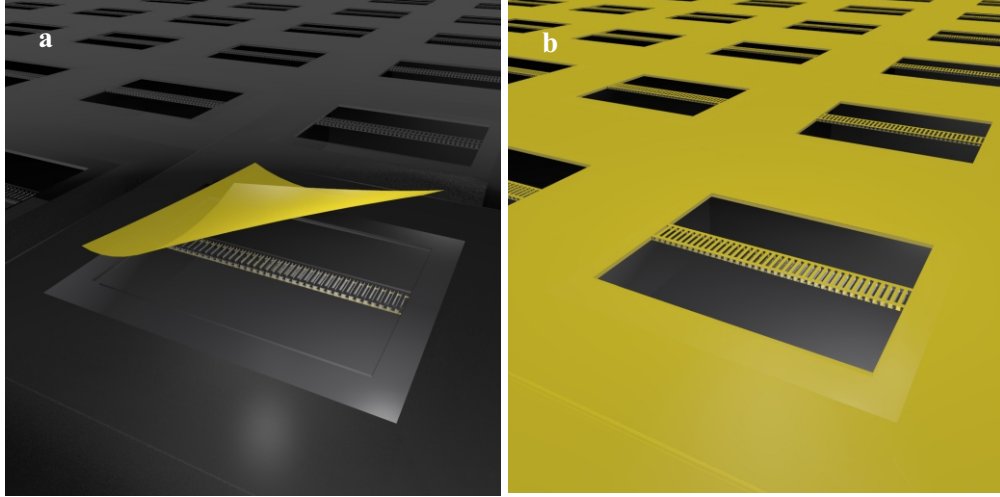


Figure 1.1.: **a** | Exfoliation of a TMD monolayer onto a single photonic crystal. **b** | Photonic crystal fabrication into CVD prefabricated TMD layer.

Figure 1.1 depicts the difference between postfabrication and prefabrication monolayer TMD integration. Exfoliation, as shown in Figure 1.1 **a**, is an easy to use method, but not scalable and flake sizes are hard to reproduce. In order to build hybrid devices, a flake has to be precisely and carefully positioned onto a prefabricated device. In Figure 1.1 **b**, monolayer TMD is grown onto the substrate via CVD previously to appropriate device postprocession.

On the basis of two examples of optical devices, we want to demonstrate the variety of scalable optical applications with CVD grown monolayer MoS_2 in this thesis. In the following, we briefly introduce two different types of devices that are fabricated and investigate in Chapters 4 and 5. For a more detailed introduction into the theoretical background, we refer to Chapter 2.

Photonic crystal cavities A photonic crystal is a periodic array of materials with different refractive indices that is based on the principles of a Bragg mirror - a mirror that is highly reflective for certain, distinct wavelengths and transmissive for others. Photonic crystal cavities (PCCs) are photonic crystals with carefully engineered “defects” in the periodicity. Thus, light of appropriate wavelengths can propagate in the defect area, but is reflected from the surrounding crystal. They, thereby, form an optical resonator that is capable of light enhancement for designated frequencies.

PCCs are potential elements of photonic circuits, networks of various photonic devices. The idea is to provide an extension of present-day high-speed information transmission

via optical fibers by integration of photonic elements into electronic circuits [48]. Such integrated systems require, at least, on-chip electrically pumpable light sources, detectors, and, ideally, optical (frequency-) selective modules.

In this thesis, we employ monolayer MoS₂ as light source that is directly coupled to a SiO₂, ladder-shaped PCC to selectively enhance certain wavelengths of the broad MoS₂ emission spectrum. An impression of a PCC array is depicted in Figure 1.1. By changing the crystal periodicity, we are able to linearly tune the enhancement peaks in wavelength. The 1D beam design, that is depicted in Figure 1.1, provides a configuration as waveguide, as well. We choose SiO₂ as platform for our PCCs due to its large bandgap of 9.3 eV [49] in order to minimize absorption losses. It is, furthermore, excellently compatible to silicon - as its natural oxide - and the most established substrate for TMD growth. With respect to future applications, the optical isotropy and non-birefringence of SiO₂ makes it a promising platform for exploiting the unique spin- and valleytronic properties of TMDs.

Metasurfaces and phase-change materials Metasurfaces or so-called “flat optics” are two-dimensionally structured surfaces or 2D patterns of nanostructures. In contrast to refractive optics, they are able to change phase, amplitude or polarization of light on a sub-wavelength scale thickness [50] and are, therefore, considered as “promising candidate[s] for realizing the next generation of miniaturized optical components” [51]. By nano-engineering of ultrathin layers of high refractive index materials, optical elements like lenses and gratings can be constructed [52]. In fact, there is an enormous variety of 2D patterns, ranging from super-oscillatory lenses (allowing sub-wavelength focusing) [53, 54] to holographic patterns (allowing reproduction of arbitrary three-dimensional (3D) structures) [55].

Phase-change materials are materials that rapidly change their (optical) properties under external influences due to a phase change of their crystal structure. A common example of this class of materials is germanium antimony telluride (Ge₂Sb₂Te₅, GST) which is used in rewritable optical discs and memory applications [56]. The phase change from an amorphous to a crystalline state is induced by a laser of sufficient power (usually femtosecond pulses) which leads to a change of its complex refractive index [57]. These properties can be used to build all-optical switches [58] or to write and erase arbitrary 2D patterns and metasurfaces in a GST film [55]. A second prominent example of phase-change materials is vanadium dioxide (VO₂). VO₂ undergoes a temperature driven metal-insulator transition (MIT) at a critical temperature $T_c = 68^\circ\text{C}$ (for bulk material) leading to a large change in both its conductivity [59] and dielectric function [60]. Apart from temperature change, the MIT can be also induced by external pressure [61], voltage [62], and laser pulses [63]. For laser induced MIT, remarkable sub-picosecond switching times have been measured [64, 65].

Implanted VO₂ nanoclusters are able to shift the reverse MIT (once heated above T_c) down to almost room temperature. This leads to a hysteresis featuring two critical tem-

peratures depending on the present phase. When the sample is heated to a temperature near T_c , it is possible to write reconfigurable 2D patterns similar to GST into a layer of implanted nanoclusters [66]. If the implant process is conducted with a prefabricated shadow mask, permanent patterns like gratings can be fabricated that change their complex refractive index with temperature [67]. In contrast to VO₂ film or bulk, embedded nanoclusters endure repetitive mechanical stress introduced by the MIT much better and excellent durability over thousands of cycles has been shown [68].

Apart from the broad field of photonics, VO₂ is also employed in many other fields of research such as (commercial) smart windows and coatings [55, 69–73], thermal actuators [74, 75], plasmonic switches [62, 76], infrared detectors [77], and gas sensors [78].

In this work, we want to focus on FZP lenses - flat optical elements consisting of concentric rings of varying width that has been already invented by Augustin Jean Fresnel (1788-1827) in the early 19th century. Today, they are predominantly used for soft X-ray focusing [79], but there are also more exceptional applications in the visible regime like FZP lenses fabricated on a fiber head for micro-focusing [80]. Non-optics related FZP applications have emerged, for example, in the field of acoustics for ultrasound focusing [81]. In Chapter 5, we implement FZP lenses in a SiO₂ matrix by site-selective VO₂ nanocluster implantation. With lateral sizes of several ten μm and focal lengths ranging from 5 μm to 20 μm , we will demonstrate the feasibility of on-chip focusing of MoS₂. In future works, more complex patterns like arbitrary holographic patterns are thinkable. We will, furthermore, demonstrate temperature dependent optical switching of their focusing ability and reproduce the characteristic refractive index hysteresis of VO₂ nanoclusters through investigation of the focal spot intensities.

2 | Fundamentals

2.1. 2D Transition metal dichalcogenides

Transition metal dichalcogenide (TMD) monolayers are triple atomic layers with the stoichiometry MX_2 . M is a transition metal (for example Mo, W, Nb, Ta) located in the middle which is surrounded by two chalcogene atoms X (for example S, Se, Te). The monolayer thickness is about 6.7 \AA [82]. Figure 2.1 **a** shows its stoichiometry in top and side view in the two common phases, the trigonal prismatic (2H) and the octahedral (1T) phase. A possible distorted phase with lower periodicity is the dimerized 1T (1T') phase with additional bonds between the transition metal atoms [83]. The 2H phase shows an A-B-A stacking and is the thermodynamically stable phase for TMD monolayers with transition metals Mo and W [83]. In the metastable 1T phase, the top and bottom layer are shifted against each other which yields an A-B-C stacking. The red arrows in Figure 2.1 symbolize one possible set of base lattice vectors which are equal for the 2H and 1T phase.

While the 1T and 1T' phases are always metallic, the 2H is semiconducting when the transition metal is either Mo or W. For that reason, we will, in the following, consider the term TMD to be a Mo or W compound in the 2H phase. All devices that will be introduced and investigated in this thesis (see Chapters 4 and 5) are implemented with MoS_2 .

Figure 2.1 **b** depicts the first Brillouin zone of a TMD. It appears to be similar to graphene, but with an important difference. There are two distinguishable K points, K and K' (equivalently, a M and M' point and a Σ and Σ'), which originates from the lack of an inversion center in the monolayer [34]. In contrast, a bilayer owns an inversion center as shown in the sideview sketch in Figure 2.1 **c**. The consequences of two distinguishable K points influencing the physical properties will be discussed later in this section.

Band structure Figure 2.2 depicts band structure calculations by Splendiani *et al.* [40] of bulk, four-layer, two-layer, and monolayer MoS_2 . The conduction band (CB) minimum and valence band (VB) maximum - in the following, only referred to as CB and VB - are highlighted in red and blue, respectively. Bulk MoS_2 shows an indirect transition between the Γ and Σ point, represented by the black arrow, that slightly increases when the material is thinned down to four and two layers, eventually. For monolayers, this indirect transition increases drastically with the result that a direct transition emerges

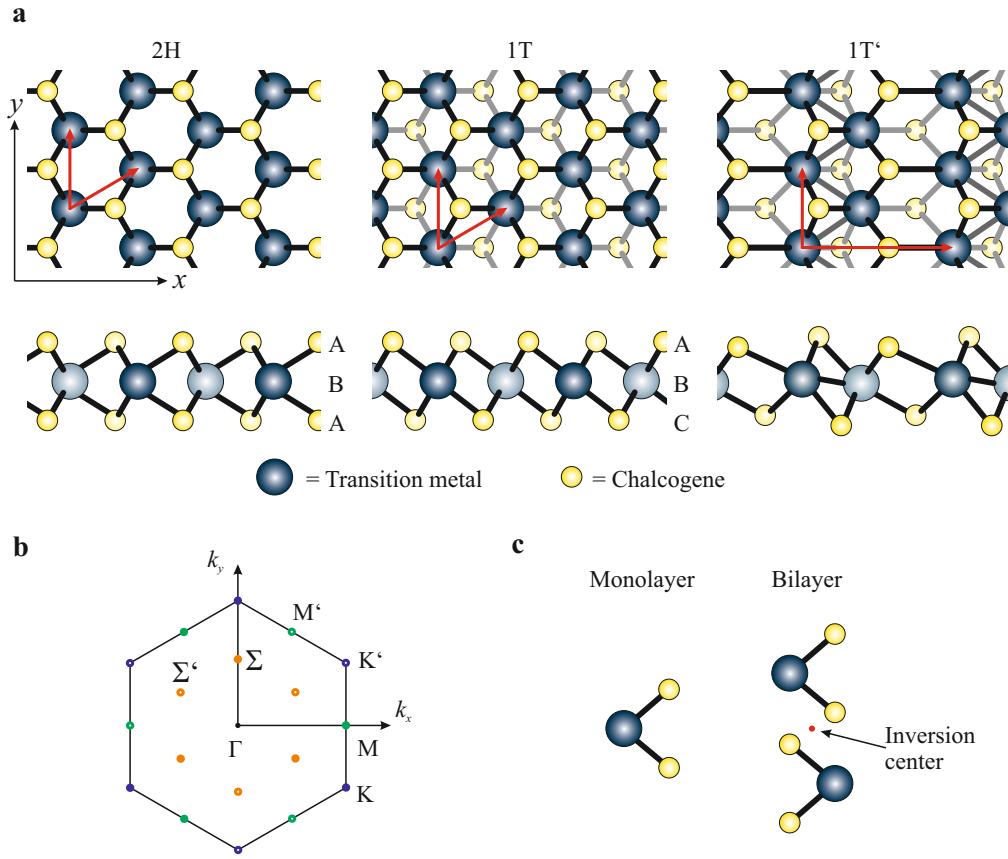


Figure 2.1.: **a** | Stoichiometry (top and side view) of TMD monolayers in three different phases. The red arrows depict the lattice vectors. **b** | First Brillouin zone of the 2H phase. **c** | Sideview of a TMD monolayer and bilayer. The former shows no inversion center while the latter does.

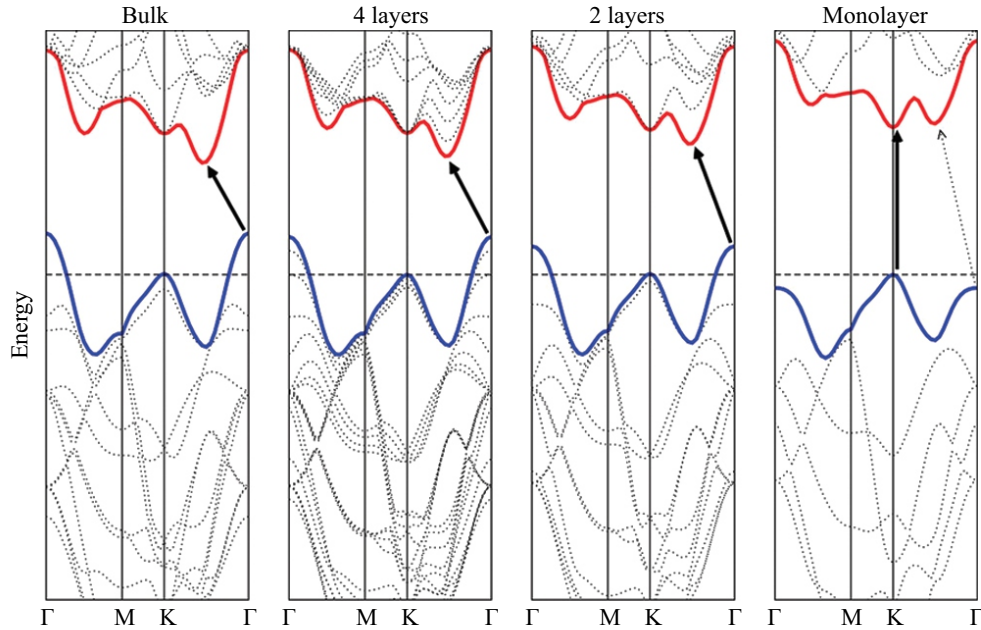


Figure 2.2.: Bandstructure calculations for bulk, few layers and one layer, adapted from [40]. The conduction band minimum is highlighted in red, the valence band maximum in blue. The arrows depict the energy gap which changes from indirect to direct for a monolayer.

at the K point. The strong decrease of the VB at the Γ point can be attributed to the change of atomic orbital hybridization due to (increased) quantum confinement in the monolayer [40, 84]. The band structure at the K points is found to be primarily consisting of strongly localized Mo d-orbitals. Due to their central position in the monolayer, interband coupling is minimal and the band structure stays rather unaffected for layer number variations. States at the Γ point and at the indirect transition, on the other hand, comprise high contributions of p_z orbitals stemming from S atoms. Their strong interlayer coupling results in a sensitive dependence on the layer number. The simulated observations in Figure 2.2 have been directly verified by angle-resolved photoemission spectroscopy (ARPES) measurements of the bandstructure [85]. As a consequence of the direct bandgap, monolayer MoS_2 shows, in contrast to bulk or even few layer MoS_2 , extremely high optical activity.

Excitons and optical transitions Figure 2.3 a shows a bandstructure calculation by Zhu *et al.* [86] that includes the spin degree of freedom. As a result, we observe a very large spin-orbit coupling (SOC), which, in particular, leads to a large VB splitting at the K point. The band splitting of MoS_2 is about 150 meV, while other TMDs like molybdenum diselenide (MoSe_2), tungsten disulfide (WS_2), and tungsten diselenide (WSe_2) show even higher values exceeding 450 meV (WSe_2) [86]. Figure 2.3 b shows a simplified

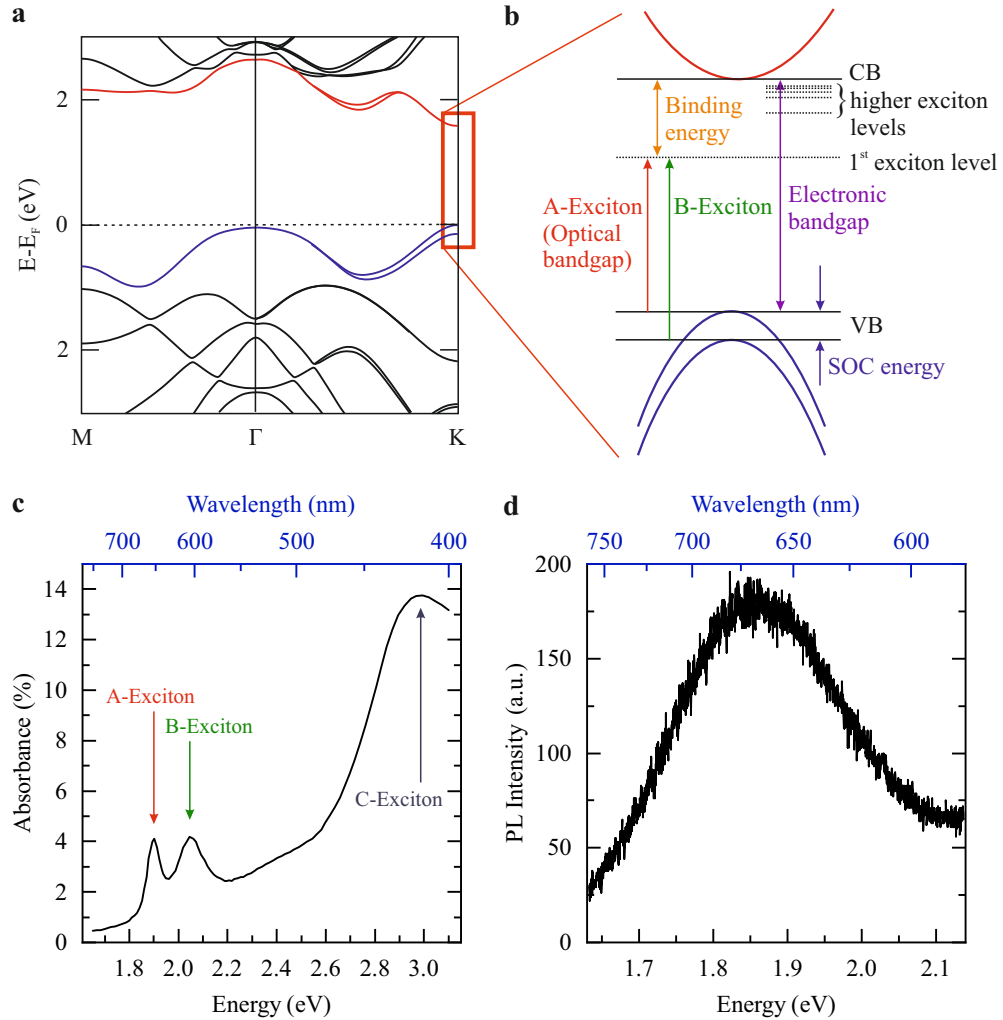


Figure 2.3: **a** | Bandstructure simulation of monolayer MoS₂ under consideration of SOC, adapted from [86]. The CB and VB are highlighted in red and blue, respectively. A distinct band splitting of the valence band emerges at the K point. **b** | Simplified sketch of the bandstructure at the K point. While the VB splitting is significant, we can neglect the CB splitting. The arrows label the A and B exciton transition as well as certain energies. **c** | Absorbance spectrum of monolayer MoS₂, adapted from [87]. The three exciton absorption lines are labelled. **d** | PL spectrum of monolayer MoS₂.

sketch of the bandstructure at the K point. In contrast to the significant VB splitting (blue arrows), the CB splitting is only a few meV [88–90] and, therefore, neglected in the sketch. While the electronic bandgap (violet arrow) is the energy difference between CB and VB, the smaller “optical bandgap” (red arrow) is the energy that we are able to observe in optical measurements. This discrepancy emerges from the formation of electron-hole pairs, so-called “excitons”, that are bound by their Coulomb interaction in the semiconductor. Depending on the binding energy, the emitted photon energy is reduced. In order to calculate higher energy levels, excitons in bulk semiconductors are usually treated equally to hydrogen atoms. In this model, the n -th binding energy level is $E_{3D}(n) = R_y/n^2$ with R_y the excitonic Rydberg constant. In 2D materials, however, binding energies are stronger due to reduced screening of the out-of-plane electric field. This results in an adapted model for two dimensions [91], in which the energy levels are described by

$$E_{2D}(n) = \frac{R_y}{(n - \frac{1}{2})^2}, \quad (2.1)$$

exhibiting four times stronger binding energies. The exciton levels are also indicated in Figure 2.3 **b**. For MoS₂, experimental values range from 200 to over 500 meV [92–94] (predicted theoretical values are even higher [89]) which is extremely large compared to bulk MoS₂ with 56 meV [95] or conventional direct semiconductors like gallium arsenide (GaAs) with <5 meV [96]. WSe₂ and MoSe₂ show similar or slightly higher values [89], while for WS₂, exciton binding energies of up to even 700 meV [97] have been measured. The optical bandgap is, therefore, the electronic bandgap reduced by the exciton binding energy. Apart from the first exciton level that is labeled in Figure 2.3 **b**, even higher exciton states up to the 5s shell have been measured [91]. The band splitting in the valence band leads to two exciton transitions of different energy at the K point, the so-called A (red arrow) and B (green arrow) excitons.

Figure 2.3 **c** shows the optical absorption spectrum of MoS₂ obtained from ellipsometric measurements by Funke *et al.* [87]. The two labeled peaks at 1.90 eV and 2.05 eV arise from the A and B exciton transition. The prominent and rather broad C exciton peak at about 3.0 eV can be attributed to a high joint density of states in the band structure, that leads, according to Fermi’s Golden Rule, to an increase in the optical transition rate (see also Section 3.3.1). It combines both bright and dark transitions stemming, on the one hand, from a high joint density of states near the Γ point and, on the other hand, from a region between Γ and M points with nearly parallel CB and VB [98, 99]. The PL spectrum of MoS₂, measured on a CVD grown film, is shown in Figure 2.3 **d**. At room temperature, it is rather broad and primarily emerges from the A exciton transition. The B exciton usually arises as a shoulder of the more dominant A exciton peak [100]. The concepts of PL will be explained in detail in Section 3.3.1.

Table 2.1 depicts the bandgap energies of the most common TMDs that are of particular interest in current photonic research. As shown in Figure 2.2, the bulk bandgap of those

TMD	Bulk bandgap	Monolayer bandgap (A exciton)	
	Energy (eV)	Energy (eV)	PL wavelength (nm)
MoS ₂	1.2	1.87	663
MoSe ₂	1.1	1.56	795
MoTe ₂	1.0	1.1	1127
WS ₂	1.4	1.95	636
WSe ₂	1.2	1.67	742
WTe ₂	-	1.1	1127

Table 2.1.: Bandgap energies of the most common TMDs and the corresponding PL wavelengths [46, 101].

materials is indirect. The energies of the (direct) monolayer bandgap in Table 2.1 are those of the A exciton transition and their corresponding emission wavelength. Sulfide and selenide compounds are mostly located in the visible regime whereas tellurids show PL emission predominantly in the near infrared regime, which is especially suitable and highly interesting for telecommunication applications.

Spin-valley coupling and further properties In Figure 2.1, we have already seen that the TMD Brillouin zone exhibits two distinguishable K points. The broken inversion symmetry of the monolayer crystal structure and spin-orbit splitting at the K points results in coupled spin and valley physics that enable optical addressing and independent control of the K or K' valley and its related spin [34, 36, 37]. Figure 2.4 **a** shows a 3D illustration of the CB (dark red) and VB (blue) at the K (K') points of the Brillouin zone. The spin states in the VB are directly coupled to one of the split bands (bright and dark blue). Due to time reversal symmetry, K and K' valleys show an inverted spin configuration [36, 37]. Optical selection rules arising from angular momentum conservation lead to transitions of only specific allowed helicities in each valley, as indicated by the black and red arrows. We, therefore, can address the K valley directly by right-handed (σ^+) polarized light and the K' valley by left-handed (σ^-) polarized light. Hence, circular polarized excitation of the TMD will result in circular polarized PL of equal helicity. Figure 2.4 **b** shows circular polarization resolved MoS₂ PL under right- (black symbols) and left-handed excitation (red symbols), which has been measured by Zeng *et al.* [38]. The graph emphasizes the contrary helicity shown by the positive and negative y scale. The degree of circular polarization $P = (I(\sigma^+) - I(\sigma^-))/(I(\sigma^+) + I(\sigma^-))$ was found to be $(32 \pm 2)\%$ in both cases.

Eventually, we want to briefly highlight some further TMD properties of high interest that are currently treated in research with respect to light-matter interactions. One exceptional finding is the existence of single photon quantum emitters that have been investigated by several groups [5–9]. Quantum emitters are essential for any kind of optical quantum information transmission or computing. Furthermore, TMDs show non-linear

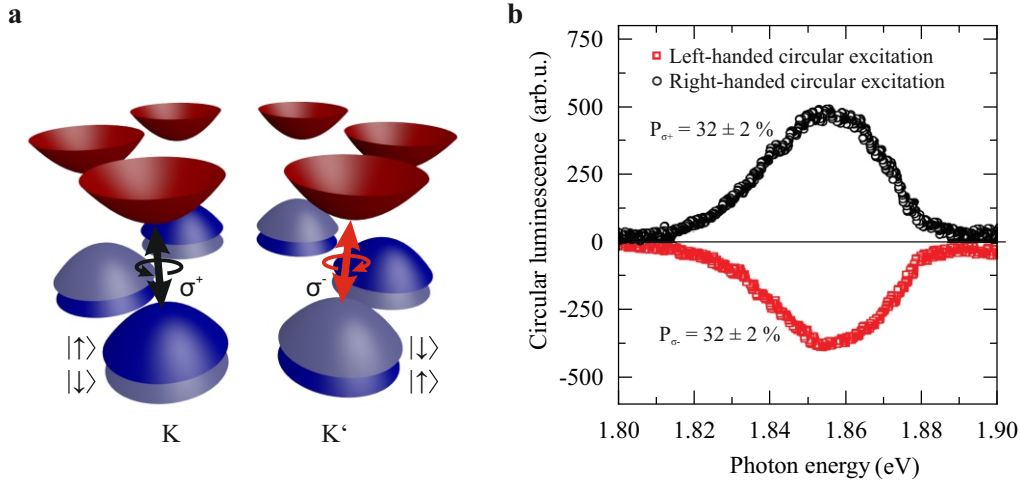


Figure 2.4: **a** | 3D sketch of the band structure near the K points. While the CB (red) splitting is very small (not visible), the VB (blue) splitting due to SOC is significant. Inversion symmetry breaking in monolayer TMDs leads to a coupling of the spin and valley degree of freedom in the two distinguishable valleys, K and K'. This permits optical addressing of a distinct valley by circularly polarized light, here, right-handed (σ^+) polarization for the K valley (black arrow transition) and left-handed (σ^-) polarization for the K' valley (red arrow transition). **b** | Circular polarization resolved PL for σ^+ (black symbols) and σ^- (red symbols) polarized excitation. The degree of polarization P is $(32 \pm 2)\%$ in both cases.

crystal properties, which implies that polarization of the crystal, introduced by electromagnetic radiation, cannot be approximated as linear for high electric fields [28]. This non-linearity leads to the generation of higher harmonics of the incident light frequency. Especially, second harmonics generation can be of high technical relevance for frequency converted lasers.

Fabrication and characterization methods Since recently, many monolayer fabrication methods have been emerged. Top-down fabrication, such as exfoliation via viscoelastic stamping [102], liquid exfoliation [103, 104], or chemical intercalation [105, 106], is usually less costly and yields good crystal quality, however, large films or reproducible flake sizes for scalable fabrication are hardly accessible. Bottom-up fabrication, such as diverse types of chemical vapor deposition (CVD) [105, 107] or vdW epitaxy [108], is scalable, but usually costly and can suffer from lower crystal quality due to grain boundaries between crystallites. In this thesis, we exclusively deal with CVD grown MoS₂. For that reason, this fabrication method is explained in detail in Section 3.2.1.

Since basically every standard characterization method in material and semiconductor research (based on interactions between electrons, ions, photons, or phonons) can be applied to TMDs as well, we will restrict ourselves to the necessary methods and only

treat PL spectroscopy and Raman spectroscopy (see Sections 3.3.1 and 3.3.2). Both methods are common for determining crystal quality and layer number (Raman).

2.2. Photonic crystal cavities

In this chapter, we will introduce the concepts of photonic crystals in general and then focus onto defects in such kind of crystals, that can operate as optical resonator: so-called photonic crystal cavities (PCCs). We will also introduce concepts for the quantification of the resonator quality and optical mode properties like the polarization.

2.2.1. Photonic crystals

A photonic crystal is a periodic arrangement of dielectric media with different refractive indices and a periodicity being comparable to the light wavelength. Depending on the number of dimensions in which this periodicity emerges, we obtain a 1D, 2D, or 3D photonic crystal as depicted in Figure 2.5 **a**.

In order to better illustrate the principles of photonic crystals, we start with a conceptual picture. Figure 2.5 **b** shows an light beam incident normally from the left side onto a 1D photonic crystal, two types of alternating layers with thicknesses d_1 and d_2 and refractive indices n_1 and n_2 . We assume lossless materials and, therefore, only have to consider reflections and transmissions at the interfaces. Our system is designed in a way that $n_1 d_1 = n_2 d_2 = \lambda_0/4$ for a specific wavelength λ_0 . Therefore, the wave undergoes a phase shift of $\pi/2$ in each layer. Assuming that $n_2 > n_1$, we additionally have to consider a phase change of π for reflections at $n_1 \rightarrow n_2$ interfaces. Thus, the total phase shift of every partial beam is $2\pi n$, $n \in \mathbb{N}$, which results in constructive interference of the reflected partial beams. Figure 2.5 **c** shows the reflectivity as a function of the wavelength for $\lambda_0 = 600 \text{ nm}$ and $N = 1, 5, \text{ and } 10$ double layers with $n_2 = 1.38$ (MgF_2) and $n_1 = 2.3$ (TiO_2) [110], which can be calculated by the so-called “wave-transfer matrix method” [111]. For larger N , the maximum reflection and its edge sharpness increase, as well as the number of local maxima. Since this spectral area, on the other hand, exhibits a transmission close to zero, it is called “stop band”. This 1D photonic crystal is called a “Bragg mirror” or “distributed Bragg reflector (DBR)”.

We now want to widen our point of view and describe light in materials with arbitrary refractive index distributions to be able to deal with photonic crystals of different designs. The behavior of electromagnetic waves in dielectric media with magnetic field $\mathbf{H}(\mathbf{r})$ and perpendicular electric field $\mathbf{E}(\mathbf{r})$ is described by the (generalized) Helmholtz equation [109, 111]

$$\nabla \times \left(\frac{1}{\epsilon(\mathbf{r})} \nabla \times \mathbf{H}(\mathbf{r}) \right) = \left(\frac{\omega}{c} \right)^2 \mathbf{H}(\mathbf{r}), \quad (2.2)$$

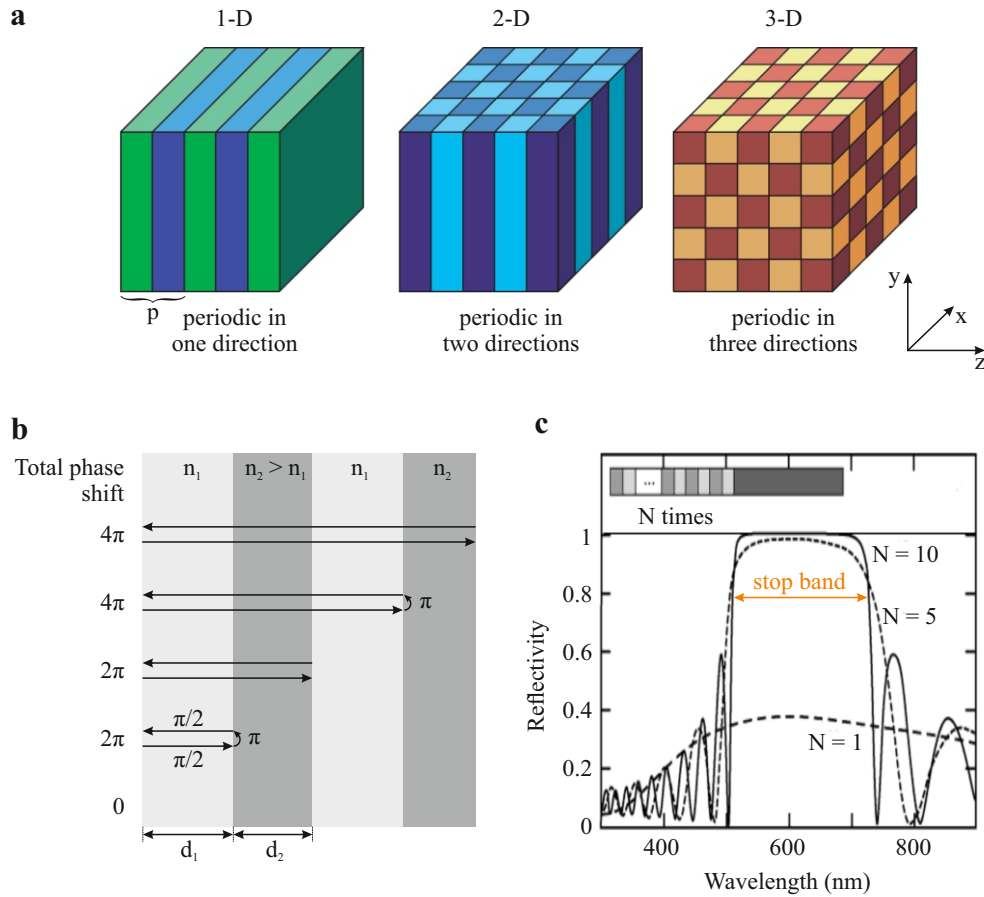


Figure 2.5: **a** | 1D, 2D, and 3D photonic crystal. The sketches are inspired from [109]. **b** | Conceptual image of multifold beam reflection and interference in a multilayer system. The alternating layers of refractive indices n_1 and $n_2 > n_1$, are chosen in a way that the thickness introduces a phase shift of $\pi/2$. Reflection at $n_1 - n_2$ interfaces causes an additional shift of π . The total phase shift of every partial beam is $2\pi n, n \in \mathbb{N}$ which results in constructive interference in reflection. Such a system is called a Bragg mirror. **c** | Calculated reflectivity of a Bragg mirror for $N = 1, 5,$ and 10 double layers with $n_1 = 2.3$ (TiO_2) and $n_2 = 1.38$ (MgF_2) [110]. Around the chosen design wavelength $\lambda = 600$ nm, the reflectivity is close to 100%. Since, on the other side, the transmission is close to zero, it is called the stop band.

with $\epsilon(\mathbf{r})$ being the relative permittivity, which directly follows from Maxwell's equations and the plane wave ansatz. It is defined by the relationship between dielectric displacement \mathbf{D} and electric field

$$\mathbf{D}(\mathbf{r}) = \epsilon_0 \epsilon(\mathbf{r}) \mathbf{E}(\mathbf{r}). \quad (2.3)$$

For gaining knowledge about the modes that propagate in any medium with well-known $\epsilon(\mathbf{r})$ function, we have to solve Equation (2.2). The relative permittivity of a photonic crystal with period \mathbf{p} satisfies the condition

$$\epsilon(\mathbf{r}) = \epsilon(\mathbf{r} + \mathbf{R}) \quad (2.4)$$

with $\mathbf{R} = n\mathbf{p}, n \in \mathbb{N}$. Hence, we choose the ansatz of Bloch's theorem [112] to solve Equation (2.2) as usually done for electronic structure calculations of atomic crystals in condensed matter physics. The magnetic field, therefore, can be expressed as

$$\mathbf{H}_{\mathbf{k}}(\mathbf{r}) = e^{i\mathbf{k}\cdot\mathbf{r}} \mathbf{u}_{\mathbf{k}}(\mathbf{r}), \quad (2.5)$$

a product of the plane wave function $e^{i\mathbf{k}\cdot\mathbf{r}}$ and a periodic function with the same periodicity as the lattice $\mathbf{u}_{\mathbf{k}}(\mathbf{r}) = \mathbf{u}_{\mathbf{k}}(\mathbf{r} + \mathbf{R})$.

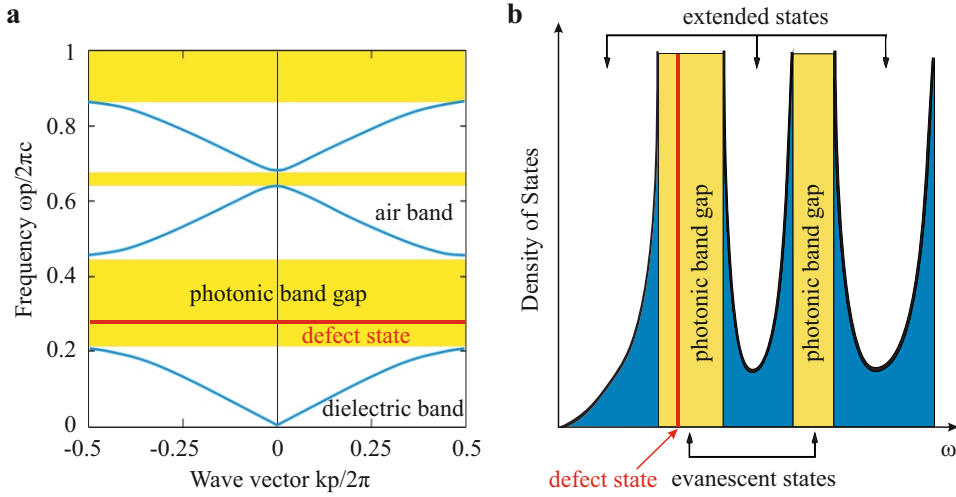


Figure 2.6.: **a** | Band structure and **b** | density of states of a photonic crystal. Yellow areas mark the photonic band gaps between the bands. The red lines depict a defect state within a bandgap that emerges from a crystal defect. Both figures are based on [109].

From the solution of Equation (2.2) for the 1D photonic crystal in Figure 2.5 **a** and the propagation direction z , we can calculate a dispersion relation, energy E as a function of wave vector k , as shown in Figure 2.6 **a**. Comparable with electrons in a semiconductor crystal, we observe photonic energy bands (representing the so-called “extended states”) which are separated by bandgaps, where only evanescent states can exist. These are states with an exponentially decreasing amplitude. For the moment, we neglect the red lines, which represent defect states. The electric field of a light wave in the energetically lowest band is predominantly located in the material of higher refractive index (usually a solid dielectric). This band is, therefore, called the “dielectric band”. The second lowest band is called the “air band” since the field is mainly located in the material of lower refractive index (usually air). The larger the refractive index difference between the two materials is, the larger is the bandgap.

Figure 2.6 **b** shows the density of states (DOS) of a typical photonic crystal. The underlying behavior follows the photon DOS per unit volume in free space

$$g(\omega) = \frac{\omega^2}{\pi^2 c^3}, \quad (2.6)$$

ω being the photon angular frequency and c the speed of light, which can be derived similarly to the free electron DOS [113]. The quadratic dependency on ω is especially visible for small frequencies, when the dielectric band nearly follows the dispersion relation of free photons $\omega = ck$. At the bandgap frequencies, the DOS is naturally zero. Near the bandgap edges, the band slopes approach zero and the DOS diverges. At these energies, the DOS shows so-called “Van Hove singularities” [114, 115].

2.2.2. Defects in photonic crystals

By introducing defects into the crystal, for example, by leaving out or changing the width of a single DBR layer, we locally change the crystal, so that localized modes can emerge. Depending on the frequency of these modes, they can form states inside the band gap. Figure 2.6 shows a defect state inside the bandgap, represented by the red line in both panels. Since light of that resonant frequency is basically trapped inside the crystal, such kind of defects are called “photonic crystal cavities”. In the following, we want to discuss the specific PCC layout that is employed in this work.

Figure 2.7 **a** shows our 1D ladder-type PCC design in top-view which has been put forward by Gong *et al.* [116]. In contrast to 2D or even 3D PCCs, this design is especially interesting for low-index materials since the light is confined in two dimensions by total internal reflection and in only one dimension by Bragg mirrors, which lower their efficiency for small refractive index differences. The crystal period p is in the order of half the wavelength of the cavity resonance and the hole width $h_x = p/2$ is kept constant in the entire PCC. The total width of the PCC is $w = 4.75p$, which has been successfully employed in [117]. A strongly decreased width would result in mode leaking, which

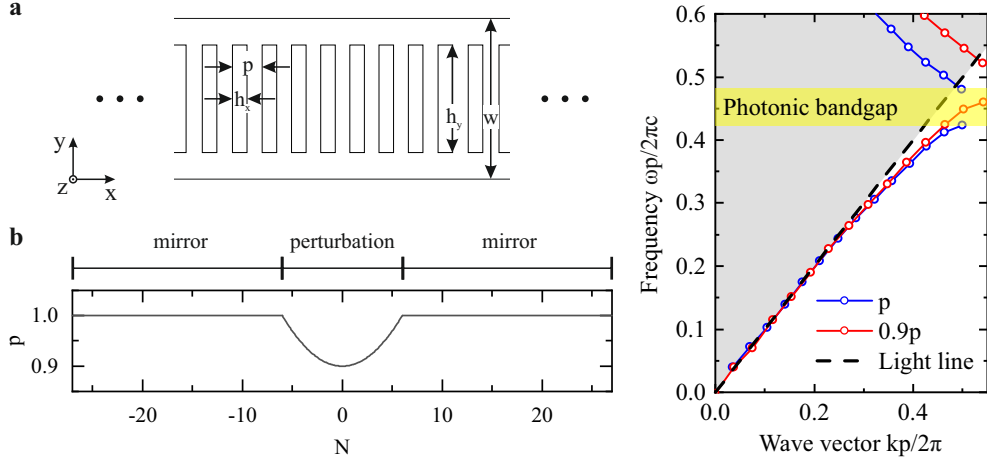


Figure 2.7: **a** | Sketch of a PCC in top view with period p , beam width $w = 4.75p$, hole width $h_x = p/2$ and hole height $h_y = 0.7w$. **b** | Period of the entire PCC as a function of the hole number. The central periods at $-6 \leq N \leq 6$ are parabolically decreased to $0.9p$. This area is called perturbation area, while the outer, unperturbed, areas are called mirrors. **c** | Band structure calculations from [116] for PCCs with periods p and $0.9p$. The latter exhibits three photonic states in the bandgap of the former. This figure is reproduced on the basis of [116].

means that the mode is completely located within the PCC, whereas a strongly enhanced width would result in decreased mode confinement. The hole height is $h_y = 0.7w$ and the thickness of the PCC is $d = 200$ nm. Although simulations show that a slightly larger thickness of 300 nm would be more favorable in terms of mode quality, fabrication constraints forced us to use a 200 nm thick membrane. The issue will be further discussed in Chapter 4.

Figure 2.7 **b** shows the period p as a function of the hole number N , which corresponds to the number of Bragg layers, counted from the center of the PCC. The entire cavity contains $2 * 27$ holes. In the outer areas, the period is kept constant in order to obtain two Bragg mirrors. These areas are labeled “mirrors” in Figure 2.7 **b**. The crystal defect is realized by a parabolic decrease of the period for $-6 \leq N \leq 6$ down to a central period of $0.9p$. This region is called “perturbation area”. The parabola depth is determined by band structure calculations [116] as depicted in Figure 2.7 **c**. It shows the dispersion relations of two crystals with periods p (blue) and $0.9p$ (red), simulated for crystals with slightly differing width ($w = 3p$) and thickness ($d = 0.9p$). It reveals that the photonic bandgap of period $0.9p$ is shifted to slightly higher energies, so that the highest states of its dielectric band move inside the photonic bandgap of the crystal with period p , highlighted by the yellow area. We observe that three modes (red circles) of the red band lie inside the photonic bandgap of the blue band. This fits nicely with our results in Section 3.1 and Chapter 4, that show three major modes observed in both simulation

and experiment.

The photonic crystal platform material is SiO_2 , for reasons that we have discussed in detail in Chapter 1. The choice of layout also results from the material choice. Since the refractive index difference of SiO_2 ($n_{\text{SiO}_2} \approx 1.46$) and air, in the visible regime, is relatively small compared to, e.g., silicon (Si) ($n_{\text{Si}} > 3.7$), the photonic bandgap is smaller, as well. This leads to higher losses in mirror directions, which makes a 1D beam design favorable. The 1D design allows us to benefit from confinement by total internal reflection in two dimensions and tailorable confinement by Bragg mirrors in only one dimension. Simulations of such PCC structures [116] show that the highest losses for $N < 10$ mirror layers arise in x direction. For $N \geq 10$, the losses in z direction dominate the total loss rate. The thickness of the PCC, however, is a parameter that is not easy to change due to fabrication constrictions and is kept constant.

2.2.3. Characterization of optical modes

Quality factor The quality factor (Q -factor) of a cavity mode is a measure of the cavity goodness as a resonator. It is defined as

$$Q = \frac{\omega}{\Delta\omega} = \frac{\lambda}{\Delta\lambda} \quad (2.7)$$

with $\Delta\omega$ ($\Delta\lambda$) being the full width at half maximum (FWHM) of the resonance frequency ω (resonance wavelength λ) [113].

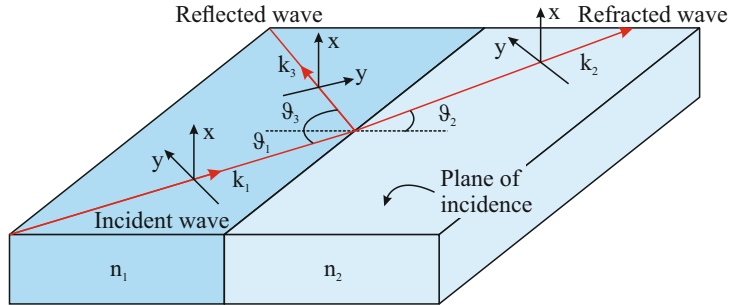


Figure 2.8.: Reflection and refraction at a dielectric interface. x -polarized waves are called transverse-electric (TE) since the electric field is orthogonal to the plane of incidence. y -polarized waves are called transverse-magnetic (TM). This figure is reproduced on the basis of [111].

Polarization of optical modes As shown in Figure 2.8, we can categorize the polarization of an electromagnetic wave incident onto an interface of two media (n_1 and n_2) into two cases [111]: The polarization (i.e. the electric field) being orthogonal (in x direction) or parallel (in y direction) to the plane of incidence. The former mode is called TE or s -polarized, the latter TM or p -polarized. For a mode traveling within a thin layer of dielectric material (be it isotropic or a photonic crystal) which is located in the xy -plane, we define the polarization in a similar manner. Modes with the electric field parallel to the xy -plane (modes of the form (E_x, E_y, H_z)) are called transverse-electric and with the magnetic field parallel to the xy -plane (modes of the form (H_x, H_y, E_z)) transverse-magnetic.

2.3. Optical coupling

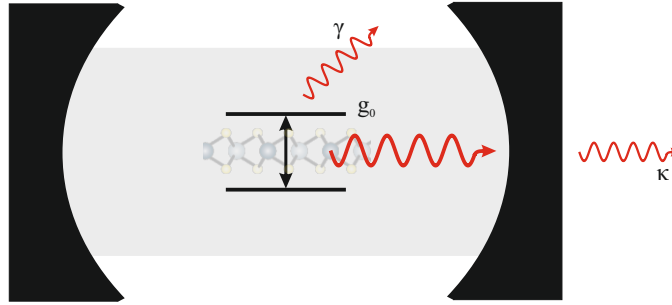


Figure 2.9.: Sketch of a TLS in a cavity coupled with a coupling constant g_0 . The TLS corresponds to the TMD monolayer in this work. The coupling regime depends on the relationship between g_0 and the cavity losses κ and non-resonant losses γ .

Resonant coupling between a cavity and an electronic two-level system (TLS) can occur in two coupling limits: the strong coupling and the weak coupling regime [113]. They can be distinguished by the coupling constant g_0 . Figure 2.9 shows a sketch of a TLS sitting in a simple two-mirror cavity. When we consider the photon decay rate of the cavity κ , the cavity decay rate can be related to the Q -factor by [113]

$$\kappa = \frac{\omega}{Q}. \quad (2.8)$$

Non-resonant losses indicated by the decay rate γ can occur by various reasons: the TLS emits the photon in an unsupported angle of the cavity (as indicated in Figure 2.9), the optically active material in the cavity decays to other levels and emits a photon of

different frequency or is scattered to other states and possibly does not emit a photon at all. Whenever other levels are involved, the TLS model gets insufficient. Strong coupling occurs when $g_0 \gg (\kappa, \gamma)$ and weak coupling when $g_0 \ll (\kappa, \gamma)$. Since, in the strong coupling limit, the interaction between TLS and cavity is faster than the loss rate of the cavity, the photon can be reabsorbed by the electronic system which represents a reversible process. Strong coupling requires very high cavity Q -factors and narrow-bandwidth light sources (ensuing low internal losses). In the weak coupling regime, the photon decay rate is much larger than the interaction rate. This leads to an irreversible process since the photon will not interact with the system a second time.

In our case, the TLS is the A-exciton of monolayer MoS₂. In Chapter 4, we will clearly observe cavity-MoS₂ coupling by cavity mode peaks emerging from the broad PL background. Due to the broad spectral emission of TMDs (indicating a non-ideal TLS) and cavity Q -factors which are measured to be (only) a few thousand, the coupling is in the weak regime. This has been similarly confirmed by Mangold [117], who used identical PCCs, but cadmium selenide (CdSe) nanoclusters as optically active material. With these clusters, even a direct measurement of the Purcell effect was possible. The Purcell effect describes the cavity related enhancement of the spontaneous emission rate. Therefore, it was necessary to measure the time dependence of the CdSe nanocrystals within and outside of a cavity. This measurement is not applicable to monolayer MoS₂ since lifetimes of 4 ps [118, 119] are too short for direct measurements with common detectors which exhibit time resolutions of about 50 ps¹.

2.4. Vanadium dioxide - a phase change material

Phase change materials are solid state materials that undergo a phase transition at a specific temperature T_c , the so-called “critical temperature”. In this thesis, we focus on vanadium dioxide (VO₂), which is one of the most promising and well studied materials.

VO₂ is a semiconducting crystal at room temperature (low-T phase) with a bandgap of approximately 0.6 eV to 0.7 eV [64, 121] and a metal when heated above its critical temperature $T_c = 68^\circ\text{C}$ (high-T phase). Despite of its clear semiconducting properties in the low-T phase, we will refer to the transition as metal-insulator transition (MIT) due to historic reasons. Although we will exclusively deal with a thermally induced MIT, it has been shown that electrical [122, 123], optical [63–65, 124] or pressure-induced [61] control is also possible. Laser pulse induced measurements show that the MIT occurs on a timescale of about 200 fs. VO₂ has been studied for about 60 years [59, 121, 125] and great efforts have been made to improve its properties for various desired applications (see Chapter 1). Especially the fabrication of nanocrystals has introduced new fascinating effects that will be considered in Section 2.4.1.

¹Single photon avalanche diode (SPAD), PDM Series, manufacturer: “Micron Photon Devices”

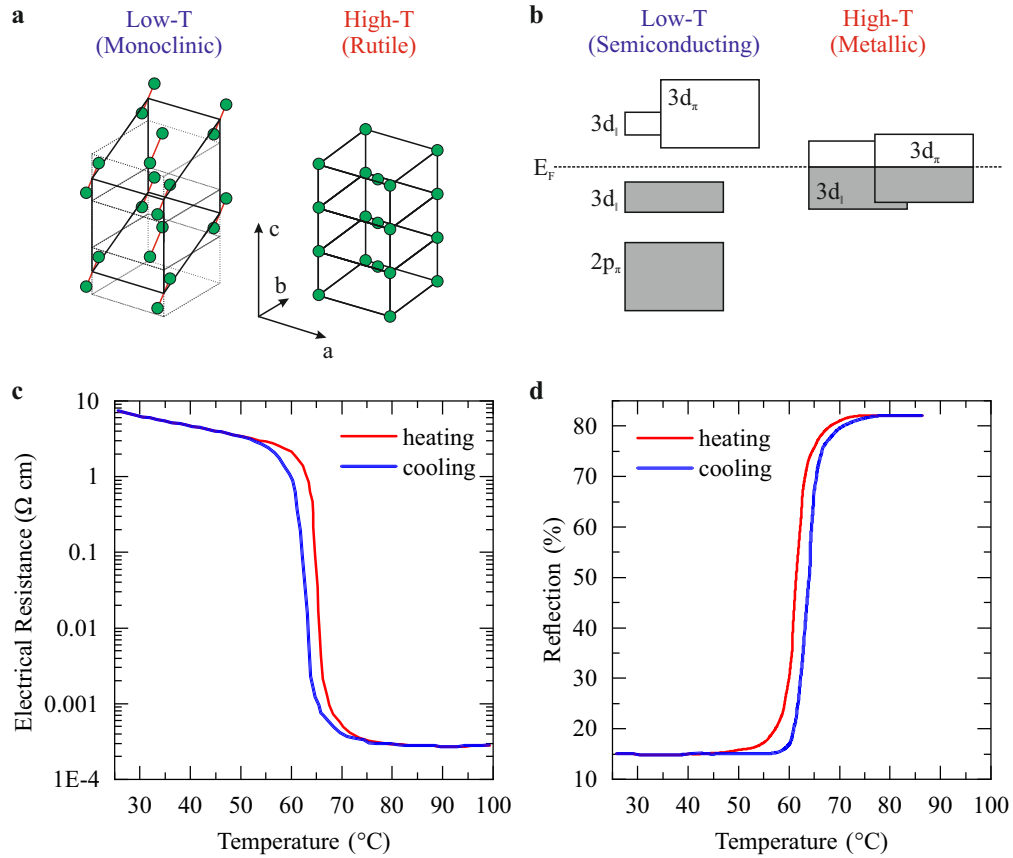


Figure 2.10.: MIT of VO₂. **a** | The VO₂ crystal structure is monoclinic in the low-T phase and rutile in the high-T phase. Only the V atoms (green) are shown, while O atoms positioned in an octahedron around each vanadium atom are omitted. In the monoclinic phase, the V atoms dimerize into pairs, illustrated by the red connectors. **b** | Bandstructure in the low-T and high-T phase. Due to the dimerization along the *c* axis in the low-T phase, the bands at the Fermi energy E_F (dashed line) split or shift to higher energies. The resulting bandgap gives rise to semiconducting behavior. The high-T phase is metallic since E_F is located inside the 3d bands. **c** | Temperature dependent electrical resistance for the heating (red) and cooling (blue) process. At the MIT, it drops by more than 4 orders of magnitude. **d** | Temperature dependent reflection with same color scheme as in **c**. At the MIT, the reflection increases from 15% to over 80%. The data in **c** and **d** is adapted from [120].

Figure 2.10 **a** shows the crystal structure of the vanadium (V^{4+}) atoms for the semiconducting (low-T) and the metallic (high-T) phase. Each vanadium atom is surrounded by an octahedron of oxygen (O^{2-}) atoms which are omitted in the sketch for clarity. The high-T phase shows a rutile crystal structure which is of higher symmetry than the monoclinic structure in the low-T phase. Here, the vanadium atoms have dimerized into pairs that are further separated from each other (3.12 \AA) than the V-V distance within a pair (2.65 \AA) [125]. Additionally, each dimer is slightly tilted against the c axis. This alteration in the crystal structure has a large effect on the bandstructure of the material as illustrated in panel **b**. The explanation of the bandstructure change is based on [64, 126, 127]. VO_2 has the electron configuration $[Ar]3d^34s^2$. In the high-T phase, the energy levels near the Fermi energy can be separated into two bands stemming from two-fold degenerate and pi-hybridized $3d_\pi$ orbitals aligned perpendicular to the c axis and a single $3d_\parallel$ orbital parallel to the c axis. These energetically overlapping bands are half-filled which causes the metallic character as depicted on the right-hand side in the sketch. In the low-T phase, the $3d_\parallel$ band splits up into bonding and antibonding orbitals due to the dimerization along the c axis. The tilting of the vanadium pairs shifts the $3d_\pi$ band to higher energies. These changes produce the energy gap and, therefore, the semiconducting behavior.

The changes in the bandstructure lead to dramatic changes in the electric, magnetic and optical properties. Figure 2.10 **c** and **d** show the temperature dependent ohmic resistance and the reflectivity of VO_2 . These measurements are adopted from J. Nag *et al.* [120]. At the critical temperature, the resistance decreases by more than four orders of magnitude and the reflectivity increases from below 20 % to above 80 %. These measurements clearly demonstrate the MIT. We also observe a small hysteresis, which will be further discussed in Section 2.4.1.

In Chapter 5, we want to specifically exploit the drastic change of the refractive index in order to build a temperature controlled switchable optical device. The complex refractive index \tilde{n} is defined by the square root of the relative permittivity or dielectric function $\epsilon(\omega)$ which has been introduced in Equation (2.3):

$$\tilde{n}(\omega) \equiv \sqrt{\epsilon(\omega)} = \sqrt{\epsilon_1(\omega) + i\epsilon_2(\omega)}. \quad (2.9)$$

The refractive index can also be separated into real and imaginary part

$$\tilde{n} = n + i\kappa \quad (2.10)$$

with the real part of the refractive index $n = \sqrt{(\epsilon_1 + |\epsilon|)/2}$ and the extinction coefficient $\kappa = \sqrt{(-\epsilon_1 + |\epsilon|)/2}$. The real part determines the propagation of light inside a medium, the imaginary part determines the attenuation.

Figure 2.11 depicts the refractive index (panel **a**) and the extinction coefficient (panel **b**) as a function of the wavelength for $T = 30^\circ\text{C}$ (blue lines) and $T = 85^\circ\text{C}$ (red lines).

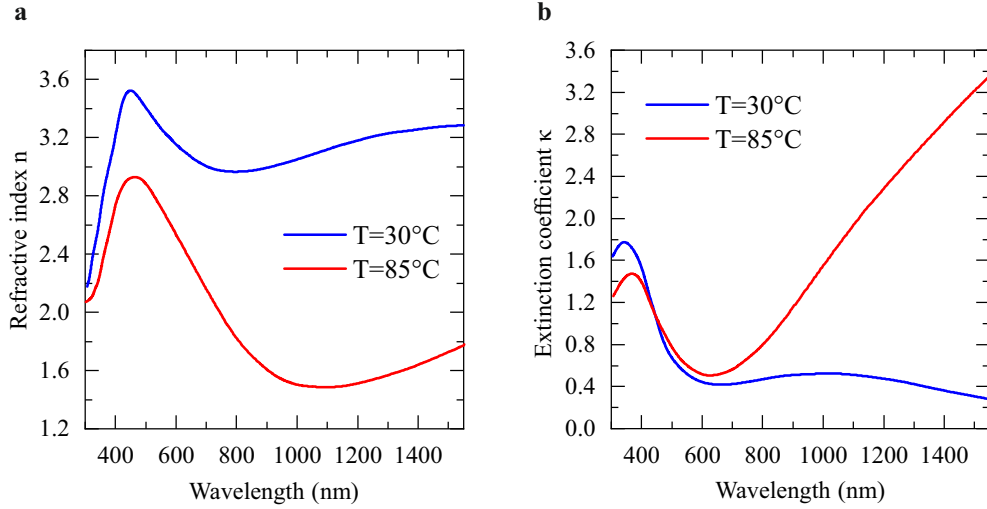


Figure 2.11.: **a** | Refractive index and **b** | extinction coefficient of VO₂ thin films in the low-T (blue lines) and high-T (red lines) phase as a function of the wavelength. The highest distinctness appears in the NIR regime. This ellipsometric data is adapted from [60].

The refractive index is lowered at high temperatures for all wavelengths. The extinction coefficient is, for $\lambda < 450$ nm, also slightly lower in the metallic phase, but increases drastically for larger wavelengths. Both n and κ are especially highly differing in the near infrared regime, for $\lambda > 800$ nm.

2.4.1. Vanadium dioxide nanoclusters

In Figure 2.10, we observe a small hysteresis at the MIT of a VO₂ film. This hysteresis gives rise to a variety of applications (see Chapter 1). It can be dramatically increased when we employ small VO₂ particles with diameters of a few 10 nm [128], so-called “nanoclusters” or “nanocrystals”. The hysteresis most likely originates from a reduced number of oxygen vacancies that occur at grain boundaries in larger crystals. Those vacancies seem to operate as nucleation points for the MIT [129]. Figure 2.13 **a** shows a transmission electron microscope (TEM) image of VO₂ nanocrystals implanted into 200 nm thick silica. It impressively shows that this technique permits rather homogeneous crystal diameters and spatial distribution as well as a uniform location in depth. Nanocluster fabrication will be discussed in detail in Section 3.2.5. The magnification of a single nanocluster in Figure 2.13 **b** clarifies that the inside of these clusters is practically defect-free. The TEM images in panels **a** and **b** are adopted from [68, 130].

Equivalently to Figure 2.11, Figure 2.12 shows the refractive indices (panel **a**) and the extinction coefficient (panel **b**) for VO₂ nanoclusters of 80 nm diameter implanted in a quartz substrate [131]. Red lines indicate the high-T (metallic) phase, while blue lines

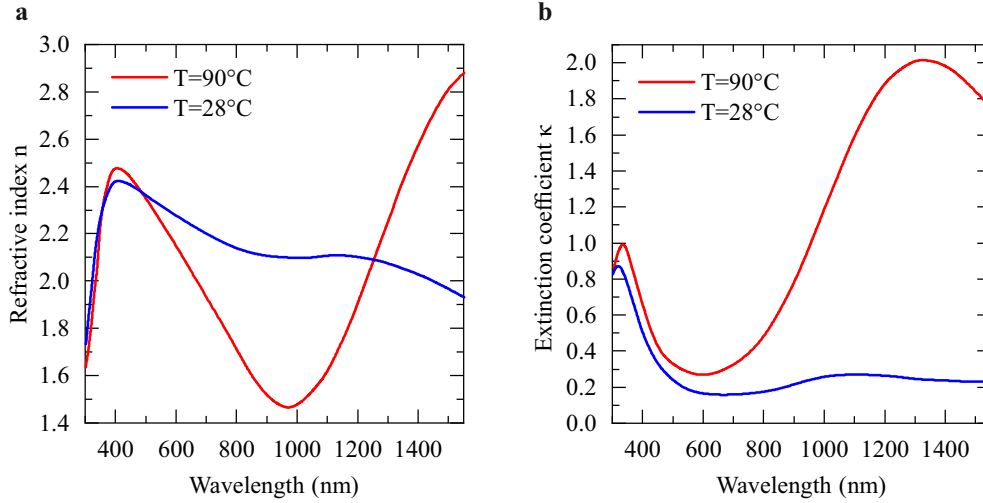


Figure 2.12.: **a** | Refractive index and **b** | extinction coefficient of VO_2 nanoclusters in the low-T (blue lines) and high-T (red lines) phase as a function of the wavelength. This ellipsometric data is adopted from [131].

indicate the low-T (semiconducting) phase. In general, the values are lower than those of the thin film due to the surrounding quartz matrix. Especially in panel **a**, we observe a qualitative difference between nanoclusters and thin film. The refractive index behaves very similarly in both phases up to a wavelength of 500 nm. At larger wavelengths, the refractive index of the low-T phase decreases almost monotonically, while the index of the high-T phase strongly increases in the NIR regime.

Besides the large refractive index change at the MIT, VO_2 also shows, like conventional metals, plasmonic effects in the metallic phase. The plasma edge, which is defined by the plasma-frequency ω_p , is near 800 nm for high-T VO_2 [65]. Light of larger frequencies (smaller wavelengths) $\omega > \omega_p$ is predominantly transmitted since the electrons cannot “follow” these frequencies - the reflectivity is low. For frequencies $\omega < \omega_p$ (larger wavelengths), electrons can follow the electric field of the incident light, hence absorption and reflectivity are drastically increased. Nanocrystals additionally show a surface plasmon resonance in the near infrared (NIR). The exact resonance wavelength depends on the particle size and shape [65]. It has been shown that this resonance is switchable as well: on the one hand, thermally induced and, on the other hand, photoinduced on a femtosecond timescale [65].

Figure 2.13 **c** shows direct transmission measurements of embedded nanocrystals in a quartz matrix. The measurement setup is described in detail in Section 3.3.3. In order to be able to observe a significant effect, a laser at $\lambda = 1550$ nm has been used since the extinction coefficient change is largest in the near infrared regime (c. f. Figure 2.12). The sample is fabricated within the same batch as those which are employed in measurements

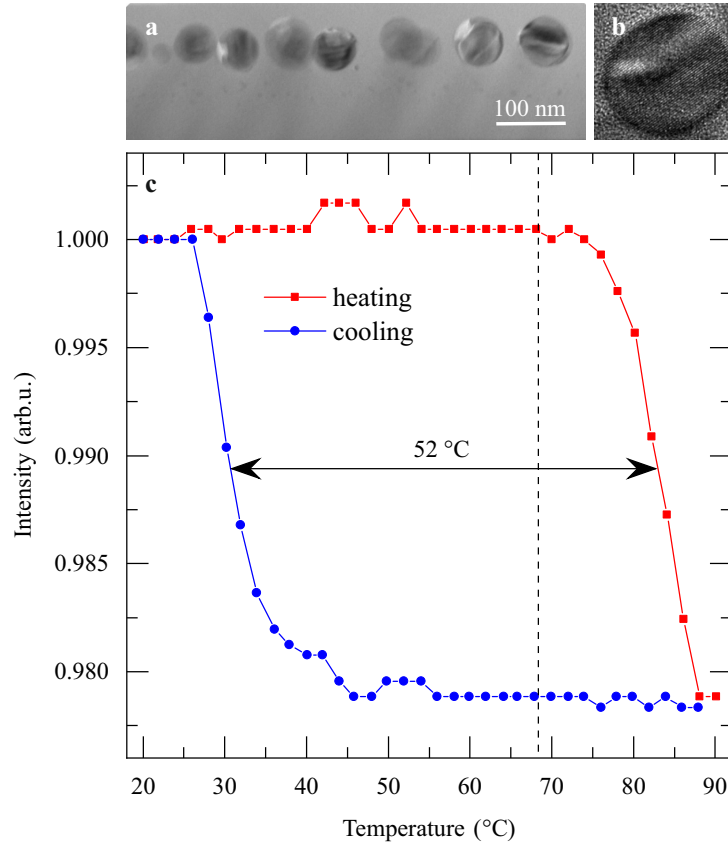


Figure 2.13.: **a** | TEM image of embedded VO₂ nanoclusters in 200 nm thick silica. They exhibit homogeneous diameters and distribution as well as a uniform implantation depth. **b** | TEM image of a single nanocluster illustrating the defect-free crystal structure inside the nanocluster. Both TEM images are adapted from [68, 130]. **c** | Temperature dependent direct transmission measurement of a quartz substrate with embedded VO₂ nanoclusters at a laser wavelength of $\lambda = 1550$ nm. It exhibits a critical temperature at about $T_c = 72$ °C in the heating branch (red symbols) and a transition temperature at about 40 °C in the cooling branch (blue symbols). The lines between the symbols are guides to the eye. The total width of the hysteresis is 52 °C.

in Chapter 5. We observe a large hysteresis of 52 °C. The MIT occurs at temperatures slightly higher than 68 °C on the heating branch (red). Besides the lack of phase change nucleation defects in nanoclusters, this can also originate to some extent from the position of the Peltier element and the temperature sensor on the sample holder. Due to an inevitable distance from the sample, the local temperature at the measurement spot will always be slightly lower than the measured temperature. The MIT in the cooling branch (blue) is between 30 °C and 40 °C. Similar measurements on VO₂ implanted diffraction gratings have been performed by J. Zimmer *et al.* [67]. The diffraction ability especially reproduces the change in the real part of the refractive index and shows much higher intensity changes as in a simple direct transmission measurement. Here, we observe a change of comparatively low 2%, but with the benefit of a rather simple setup.

2.5. Fresnel zone plates

In contrast to conventional refractive optical devices, Fresnel zone plates (FZPs) are representatives of diffractive optics that rely on the principles of diffraction and interference. FZP lenses are extensively employed in soft X-ray microscopy since refractive optical devices would simply absorb the major amount of the radiation [79]. A unique property is the two-dimensionality of the structure that enables applications on small scales (close to the sample) and easy fabrication processes, for example, by lithographic methods.

In order to understand the functioning of a FZP lens [79, 132–134], we first consider a pinhole aperture that is illuminated by a planar wavefront. Figure 2.14 illustrates the way we now divide the transmittive area of the pinhole into concentric disks n , n integer, in a way that the optical path between a given point f on the symmetry axis and disk n lies between $f + \frac{n\lambda}{2}$ and $f + \frac{(n-1)\lambda}{2}$. These disks are called Fresnel zones or half-period zones.

Using the Pythagorean theorem, we get the expression

$$r_n^2 + f^2 = \left(f + \frac{n\lambda}{2}\right)^2 \quad (2.11)$$

with r_n being the radius of the n -th ring and obtain

$$r_n^2 = n\lambda f + \frac{n^2\lambda^2}{4}. \quad (2.12)$$

For $f \gg \lambda$, we can neglect the quadratic term in n and obtain the disk radii

$$r_n \approx \sqrt{n\lambda f}. \quad (2.13)$$

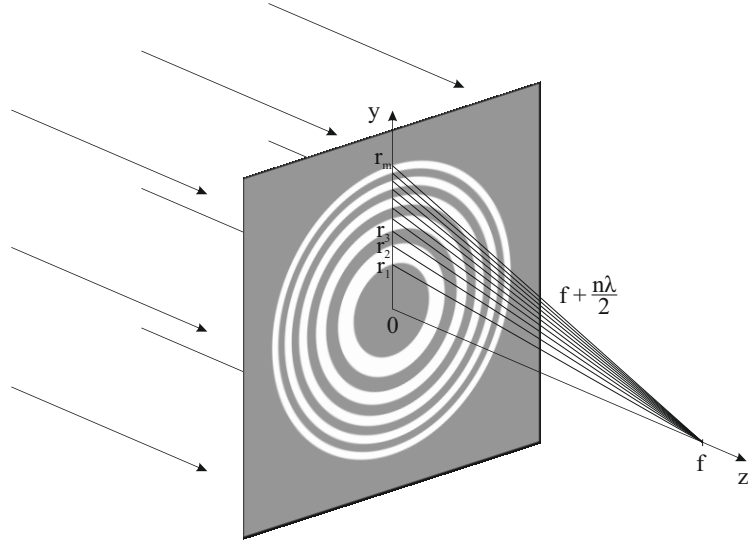


Figure 2.14.: Fresnel zone plate lens with a plane wave incident from the back. The concentric discs have radii in a way that the optical path from the disk edge to a predefined focus point f is incrementally increased by $\frac{\lambda}{2}$. Alternating opacity of the disks ensures filtering out the terms that contribute destructively to the interfering waves at point f .

The construction of the Fresnel zones is chosen in a way that adjacent zones have a phase difference of π , which means that they interfere destructively. In order to exploit this effect, we simply blank every second zone, which leads to a focusing effect with first order focus point f . Such a device is called a Fresnel zone plate lens. Concerning the alternating zone blanking, it doesn't make a difference whether to start with the central zone blanked or transparent since the focusing effect stays the same. Also, the efficiency would not change because the area of every Fresnel zone is identical (at least within the approximation made in Equation (2.13)) [79]. However, when measuring the intensity of the focus spot, a blanked central zone is preferred due to the lack of a (zero order) forward transmission background on the optical axis.

Just like a diffraction grating, and in contrast to a refractive lens, a FZP lens has multiple (including negative) order focus points when, in addition to path length differences of $\frac{\lambda}{2}$, multiples of $\frac{\lambda}{2}$ are considered. Consequently, Equation (2.11) can be extended to

$$r_n^2 + f_m^2 = \left(f_m + \frac{mn\lambda}{2} \right)^2, \quad (2.14)$$

which can be simplified to

$$r_n^2 \approx mn\lambda f_m. \quad (2.15)$$

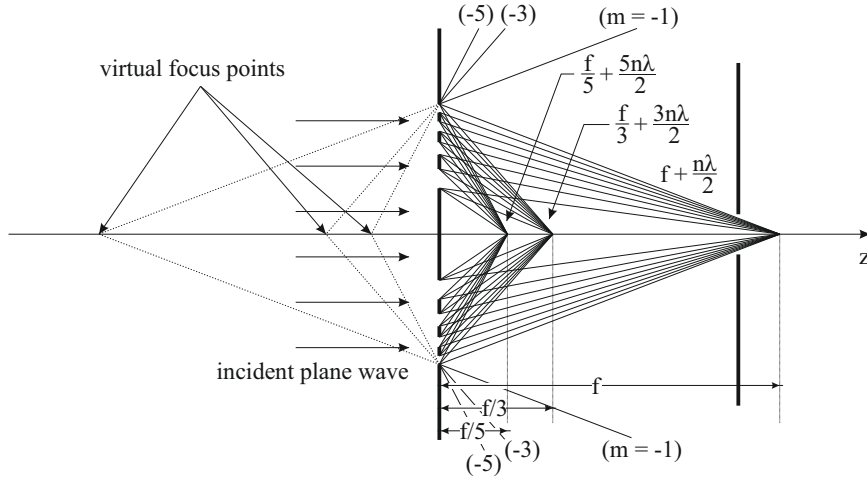


Figure 2.15.: The first three positive orders ($n = 1, 2$ and 3) of interference. At real microscopic applications, an order sorting aperture (OSA) is used to block higher orders. The corresponding negative orders ($n = -1, -2$ and -3) are diverging from the optical axis. An extension of the beam paths (dashed lines) illustrates the formation of virtual foci behind the FZP lens.

Equations (2.13) and (2.15) yield the corresponding focal lengths

$$f_m = \frac{f}{m}. \quad (2.16)$$

Figure 2.15 depicts the side view of a FZP lens with an incident plane wave. It shows the optical paths of the first three positive order focus points labeled with their respective optical path length. In a real application, negative and higher order focus points are usually blocked by an order sorting aperture (OSA) [79]. Negative orders diverge from the optical axis and create virtual foci behind the FZP lens, which are indicated by the dashed lines.

The diffraction efficiency η_m of order m is determined by the square of the respective Fourier coefficient c_m when we expand the diffraction pattern in a Fourier series [79]. The result is identical to conventional linear diffraction gratings

$$c_m = \frac{\sin(m\pi/2)}{m\pi} \quad (2.17)$$

and can be summarized as follows:

$$\eta_m = \begin{cases} \frac{1}{4} & m = 0 \\ (m^2\pi^2)^{-1} & m \text{ odd} \\ 0 & m \text{ even} \end{cases} \quad (2.18)$$

This means that about 10% of the intensity incident on the FZP lens area are collected in the positive first order which most applications make use of. An equal amount goes to the corresponding divergent negative order and approximately 1% goes to the third order. The major amount of light is either absorbed by the opaque zones (50%) or transmitted in the forward direction (25%).

3 | Methods

In this chapter, we introduce basic methods employed in the areas simulation, sample fabrication, and optical measurements. We will refer to these methods in various passages in Chapters 4 and 5.

3.1. FDTD Simulation

The basis of finite-difference time-domain (FDTD) simulations have been firstly described by Yee in 1966 [135]. With increasing computer power, the method has developed into a powerful and widespread technique for calculating electromagnetic waves in arbitrary environments. The brief introduction on FDTD principles presented in the following is based on chapters 1 to 3 of *Computational electrodynamics: The finite-difference time-domain method* by Taflove and Hagness on the reference number [136].

The fundamental approach of FDTD simulations is the (efficient) solution of Maxwell's equations in their differential form on sufficiently short length scales (about 10% of the considered wavelength) for discrete, successive time steps. Maxwell's equations in isotropic charge- and current-free media are

$$\nabla \cdot \mathbf{E} = 0 \tag{3.1}$$

$$\nabla \cdot \mathbf{B} = 0 \tag{3.2}$$

$$\nabla \times \mathbf{E} = -\mu_r \mu_0 \frac{\partial \mathbf{H}}{\partial t} \tag{3.3}$$

$$\nabla \times \mathbf{H} = \epsilon_r \epsilon_0 \frac{\partial \mathbf{E}}{\partial t} \tag{3.4}$$

with electric and magnetic field \mathbf{E} and \mathbf{H} , free-space and relative permittivity ϵ_0 and ϵ_r , free-space and relative permeability μ_0 and μ_r , and magnetic flux density $\mathbf{B} = \mu_0 \mu_r \mathbf{H}$. The use of Maxwell's differential equations and the corresponding solution in the time domain stands in contrast to former developments, specifically frequency-domain solution techniques, that employ Maxwell's equations in integral form. The progresses achieved by FDTD are a much better scalability (in frequency-domain, complex structures require

the solution of very large systems of equations) and easy incorporation of material and device non-linearities.

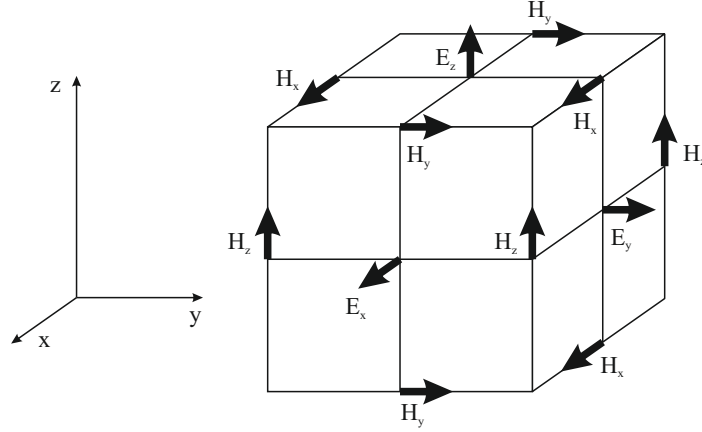


Figure 3.1.: Positions of the electric and magnetic field components in a Yee cell.

The Yee algorithm, that is still at the basis of most FDTD approaches, is designed to solve the three components of both electric field and magnetic field in discrete unit cells, so-called Yee cells, which requires the subdivision of the desired structure into a rectangular mesh. A single Yee cell is depicted in Figure 3.1. Each edge and surface of the Yee cell only occupies one of the six field components, in a way, that every \mathbf{E} field component is surrounded by four \mathbf{H} components and vice versa. This arrangement inherently enforces the so-called Gauss' law relations, represented by Equations (3.1) and (3.2). Thus, a FDTD solver only has to actively treat Maxwell's curl equations (3.3) and (3.4).

3.1.1. Photonic crystal cavities

In our photonic crystal cavity (PCC) simulations¹, we employ a simulation region with perfectly matched layer (PML) boundary conditions. This forces the region boundaries to absorb electromagnetic waves with any polarization in order to prevent reflections or artifacts from boundary constrictions. The PCC is excited by an electromagnetic Gaussian pulse in the center of the cavity of about 20 fs duration with a spectral FWHM ranging from 40 nm to 50 nm (depending on the absolute frequencies). It is detuned in wavelength by a few 10 nm from the expected main cavity resonance. This has become apparent to be more favorable for the observation of further resonance peaks in the spectral response of the cavity. In order to cover every polarization dimension, we employ three dipole sources with different orientations.

¹Employed software: FDTD simulation package by Lumerical, www.lumerical.com

For data recording, we primarily use two different types of monitors: a z -normal 2D frequency-domain field profile monitor, on the one hand, records the spatially distributed electric field components for a desired set of discrete frequencies. Time monitors, on the other hand, record the time-dependent evolution of the electric field at specific spots within the structure. Since FDTD simulations run in the time domain, the latter monitor type only needs to save all field components without much further data processing, which is rather efficient in terms of CPU and memory resources. The former monitor type transforms time-domain data into the frequency domain via fast Fourier transform (FFT) and can require much more memory, depending on the monitor size.

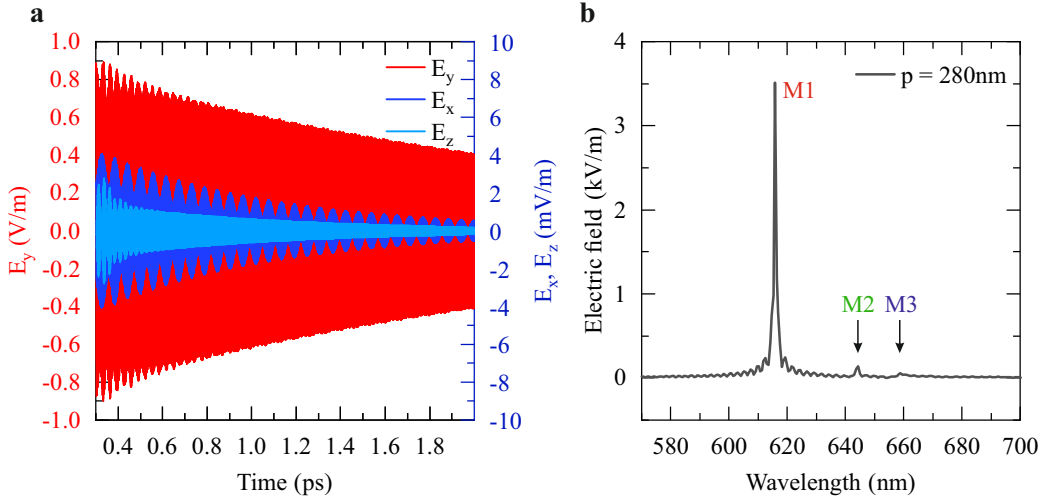


Figure 3.2.: **a** | Electric field components as a function of time near the cavity center. **b** | Calculated cavity response spectrum obtained by Fourier transform of the time dependent data shown in **a**.

Figure 3.2 **a** depicts the time evolution of the three electric field components obtained by a time monitor near the center of a PCC with period $p = 280$ nm. The scale on the left refers to the E_y component, whereas the right scale refers to E_x and E_z . In order to avoid excitation pulse recording, the detection starts with a time delay of 300 fs after excitation. Note that E_y is by a factor of $\sim 2 \times 10^2$ larger than the other two components, which indicates a strong TE mode character. The decay of the envelope function determines the cavity losses and, thus, the Q -factor. A detailed procedure to determine the Q -factor for various modes will be given at the end of this section. Figure 3.2 **b** shows the cavity response spectrum that is calculated from the time-domain data in **a** via FFT. We observe three resonant modes M1, M2, and M3. Compared to M2 and M3, M1 shows, by far, the highest intensity. From this observation, we can deduce that the dominant field contribution near the cavity center arises from mode M1. This will be verified by the dedicated mode field profiles investigated in the following paragraphs. The oscillations at the base of peak M1 are artifacts resulting from the FFT. Spectral resolution and

artifact reduction in both spectra and field profiles rely on the simulation time, which has to be chosen sufficiently long.

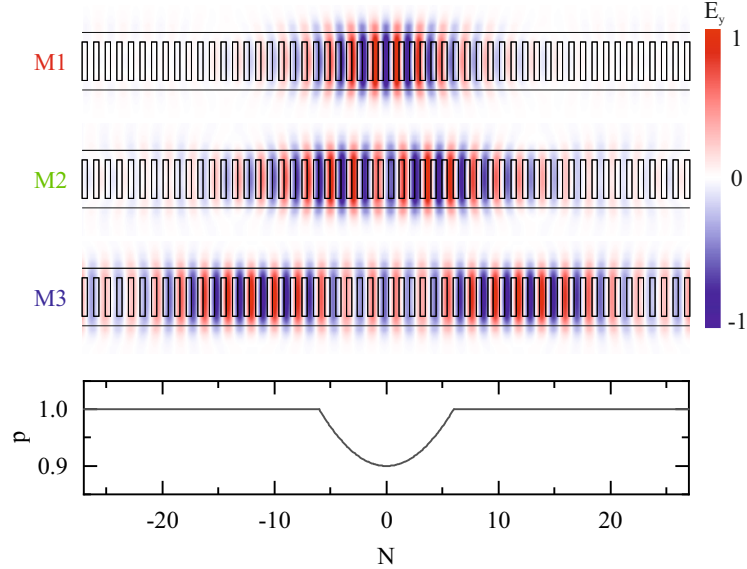


Figure 3.3.: FDTD simulated E_y field distribution in the PCC for modes M1, M2 and M3. Below: Periodicity of the PCC as a function of the hole position. In the center, it is parabolically lowered to $0.9p$. See also Figure 2.7.

We choose the mode specific field profiles (recorded by the field profile monitor) according to the mode wavelengths that we observe in the response spectrum. Therefore, we have to specify a sufficiently high wavelength resolution for the monitor. With insufficient sampling in the wavelength regime, the available field profiles might be too far detuned from the desired mode wavelength, which results in an asymmetric, “unphysical” profile. A second important parameter of field profile monitors is the so-called “time apodization”, a time delay of data recording to avoid disturbances with the excitation signal, similarly to the delay in time monitors. The apodization time is set to 500 fs.

Figure 3.3 depicts the E_y field profile of M1, M2, and M3. The periodicity of the PCC layout as a function of the hole number N is shown at the bottom of Figure 3.3 to indicate the position of the perturbation area (see also Figure 2.7). Mode M1 is a symmetric mode (i. e. $E_y(x) = E_y(-x)$) with an antinode in the cavity center. Mode M2 is antisymmetric ($E_y(x) = -E_y(-x)$) and shows two antinodes with a node in the center, while M3 is again symmetric showing three antinodes, two of which are predominantly located outside the perturbation area. The central antinode is very weak. We consider M1 the “fundamental” mode since it shows the least node number.

In general, the fundamental mode of a certain potential shows the largest wavelength (lowest energy) than higher order modes. This seems to contrast with the observed spec-

trum. The PCC, however, does not provide a uniform “confinement potential” (speaking in terms of energy) that is equal for all observable modes. M1, for example, is predominantly confined in the perturbation area, whereas M3 is mainly confined by the boundaries of the whole ladder structure. For that reason, the picture of higher order modes in a single parabolic or rectangular potential is not applicable in this type of cavity.

In order to determine the Q -factor of a specific mode, we employ the process for high- Q cavities, which is based on the time resolved field decay, as described in the Lumerical Knowledge Base [137]. High- Q cavities are present when the electric field does not decay completely in a reasonable simulation time. The Q -factor is defined by the resonance frequency divided by its peak’s FWHM as described in Equation (2.7). Spectral information can be obtained by FFT of the time resolved signal. However, the spectral resolution is insufficient for the FWHM determination in the case of high- Q cavities. For that reason, the Q -factor needs to be determined directly from the time resolved signal. At a given exponentially decaying field

$$E(t) \propto e^{-t(\alpha - i\omega_r)} \quad (3.5)$$

at a resonance frequency ω_r , the Q -factor can be expressed in terms of the decay constant α by [137]

$$Q = \frac{\omega_r}{2\alpha}. \quad (3.6)$$

In order to obtain the decay constant of specific resonances, the resonance peaks are detected in the spectrum (see Figure 3.2 **b**) obtained by FFT of the time-domain signal. In a second step, all peaks are isolated by Gaussian filters and independently back-transformed into the time domain. By logarithmic plotting of the electric field envelope for every single frequency, we can extract the slope, which corresponds to the decay constant. Finally, the Q -factors for specific modes can be calculated using Equation (3.6). The Q -factors of the modes in all simulated PCCs are depicted and discussed in Chapter 4.

3.1.2. Fresnel zone plates

Although FZP lenses can be described analytically (see Section 2.5), we require detailed simulations to determine the effect of changing refractive indices of “opaque” and “transparent” zones on the focusing properties. Assuming the lens is located in the xy plane, z is a symmetry axis, which allows us to reduce the dimension of the simulation region to 2D y -normal.

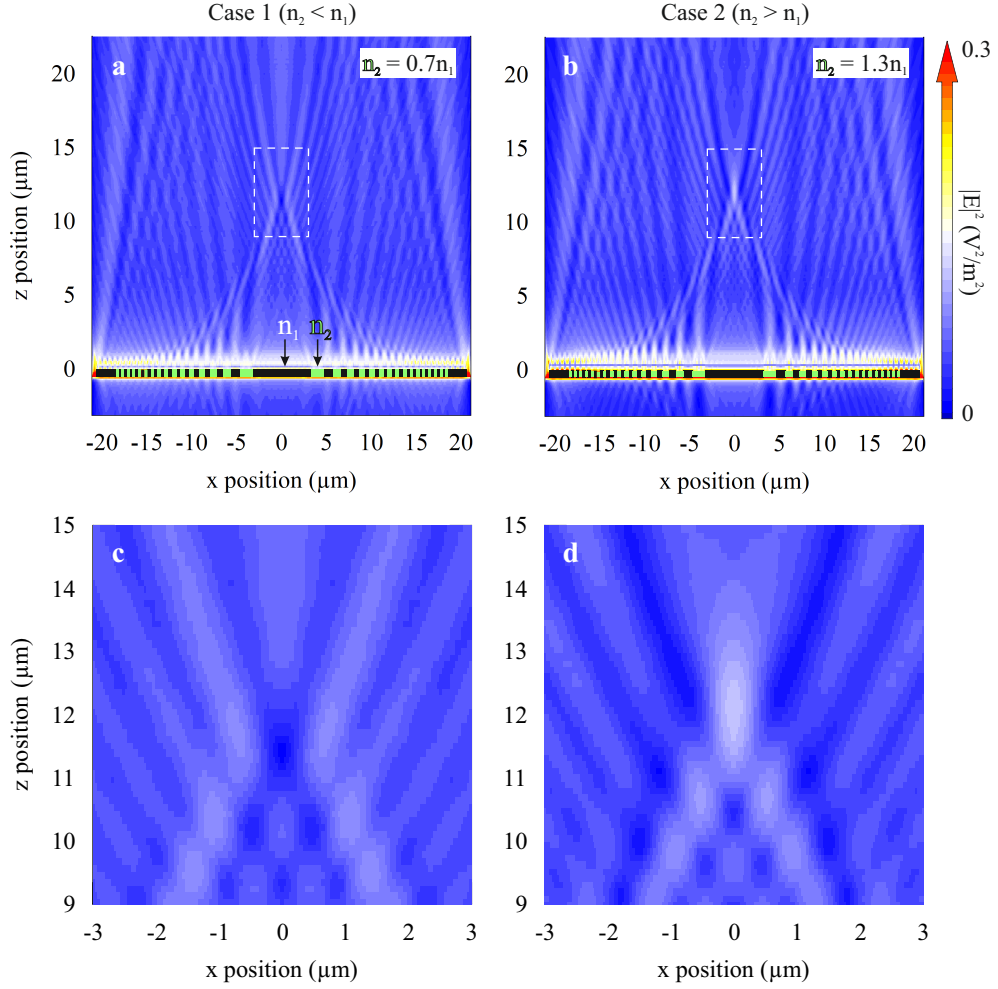


Figure 3.4.: Simulated intensity distribution $|E|^2$ of a $f = 15 \mu\text{m}$ FZP lens with incident plane wave in z direction with **a** $n_2 = 0.7n_1$ and **b** $n_2 = 1.3n_1$. The FZP thickness is exaggerated. **c** and **d** | Magnification of the respective focus area in **a** and **b** (indicated by the white dashed rectangle). The employed FZP design results in inverted interference patterns for a change of n_2 from -30% to +30% with respect to n_1 .

While the boundary conditions are PML, like in the simulations for PCCs, we now employ a plane wave as light source. Figure 3.4 shows the spatial intensity distribution $|E|^2$ in the xz plane for a $15\ \mu\text{m}$ focal distance FZP lens. The plane wave of wavelength $(670 \pm 5)\ \text{nm}$ originates below the FZP and travels in the z direction (dimensions are chosen in consistence with Chapter 5). The FZP lens is positioned at $z = 0$, has a width of $100\ \text{nm}$ (which is exaggerated in the figure), and consists of alternating zones with refractive indices n_1 (black) and n_2 (green). The FZP design is based on Equation (2.13). Refractive index and extinction coefficient of material 1 are set to $n_1 = 2.625$ and $\kappa_1 = 0.144$, respectively, which are measurement values for a $\text{VO}_2\text{-SiO}_2$ mixed layer adopted from an unpublished work by J. Zimmer.

In Figure 3.4 **a**, the refractive index of material 2 is lowered with respect to material 1 to $n_2 = 0.7n_1$ (case 1) and, in **b**, it is increased to $n_2 = 1.3n_1$ (case 2). This is basically an inversion of the FZP if we only consider the absolute difference in the refractive index: $\Delta n = \pm 0.3n_1 = \pm 0.788$. The white dashed rectangles indicate areas that are shown in magnification in **c** and **d**. The focal positions are shifted by about $3\ \mu\text{m}$ from the nominal focal distance of $15\ \mu\text{m}$ in lens direction. We, furthermore, observe destructive interference at the first order focus point in **a** or **c** and constructive interference in **b** or **d** although mathematical derivation from diffraction theory yields identical intensity distribution on the z axis for inverted FZP patterns [133]. Both effects, focus shift and intensity inversion for inverted patterns, originate from the Fraunhofer approximation that has been employed in Equation (2.13). Simulations with a FZP pattern designed after Equation (2.12) show the focus at the nominal focus position and similar interference patterns for inverted FZPs. Equation (2.13), however, has been used in the sample design in optical measurements. In Chapter 5, we will, therefore, compare the measurement results with the identically designed simulation structures in Figure 3.4. Although not intended from the beginning, we will, furthermore, make use of the distinguishability in interference patterns of inverted FZP lenses to draw conclusions about the refractive index differences between Fresnel zones.

3.2. Fabrication

In this section, we want to discuss the working principles of single fabrication steps that we used for sample preparation in this work. In Chapters 4 and 5, we will describe the complete fabrication process depending on the sample type and occasionally refer to this section. Recipes and device parameters are summarized in Appendix A.1.

3.2.1. Chemical vapor deposition

CVD is a bottom-up technique for scalable monolayer MoS_2 growth and has been developed into one of the most promising candidates for industrial fabrication [43, 45, 47, 138].

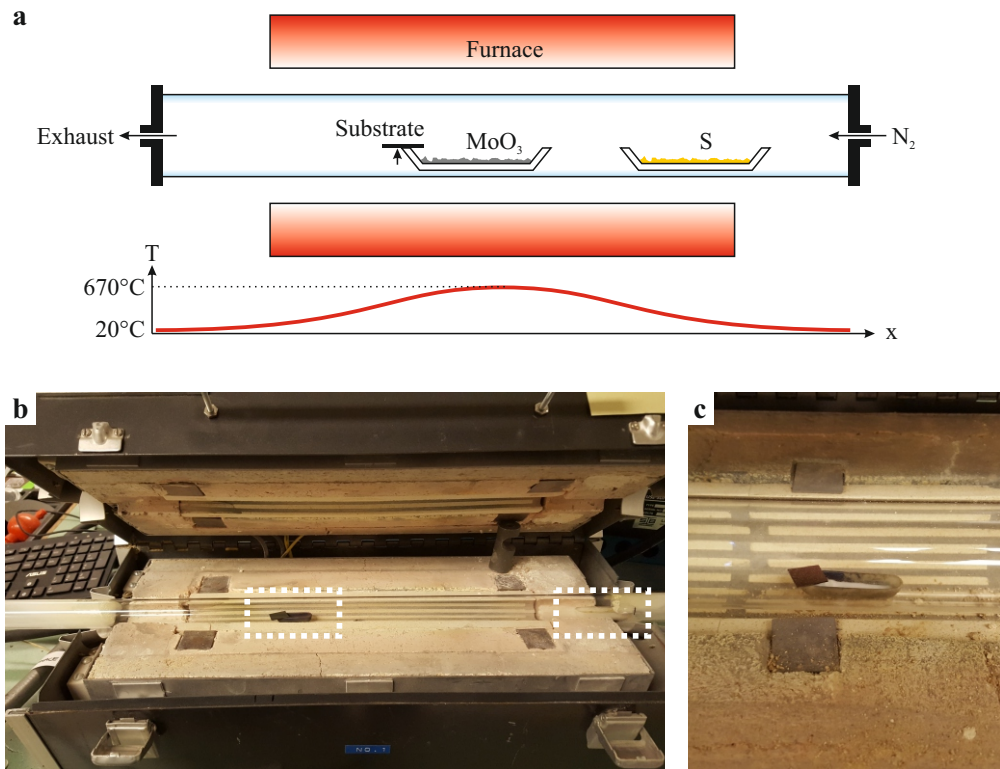


Figure 3.5.: a | Sketch of the CVD setup used for monolayer MoS_2 growth in this thesis. Two boat crucibles with precursors MoO_3 and S are located inside of a quartz glass tube that is heated by a furnace. The substrate is carried by the boat in the center. During the growth process, a constant N_2 flow is applied. The curve beneath the sketch qualitatively illustrates the temperature dependence on the position, which indicates the importance of the boat position. b | Photograph of an open furnace equipped with precursor boats (highlighted by white dashed rectangles). c | Magnified image of a boat containing MoO_3 powder with a substrate on top.

The CVD setup that has been employed in this thesis is described in [44, 107] and is depicted in Figure 3.5 **a**. Two alumina boat-shaped crucibles containing the precursors molybdenum trioxide (MoO_3) powder and sulfur (S) powder are placed into a quartz tube that is heated by a furnace. During the growth process, the tube is gradually heated to a final temperature of 670°C , kept at this temperature for about 10 min, and gradually cooled down to room temperature. Since the temperature inside the tube is position dependent, which is qualitatively illustrated by the curve beneath the sketch in **a**, the boat positions are crucial for the growth process. The MoO_3 boat is localized near the center experiencing the nominal process temperature, while the S boat is positioned near the edge of the furnace at a temperature slightly above the S melting point of 115°C . A low nitrogen (N_2) molar flow rate of 0.5 SCFH (236 sccm) applied at the S boat side of the tube establishes a N_2 atmosphere during the reaction. The sample is cleaned immediately prior to growth by piranha² etch solution and placed upside down on top of the downstream side of the MoO_3 boat. During the growth, MoO_3 and S react with each other to form MoS_2 and sulfur dioxide (SO_2), presumably under formation of the intermediate compound molybdenum dioxide (MoO_2) [139]. The small arrow indicates the site of monolayer MoS_2 deposition. Figure 3.5 **b** shows a photograph of an open furnace equipped with precursor boats that are highlighted by the white dashed rectangles. Panel **c** shows a MoO_3 boat with a substrate on top in magnification.

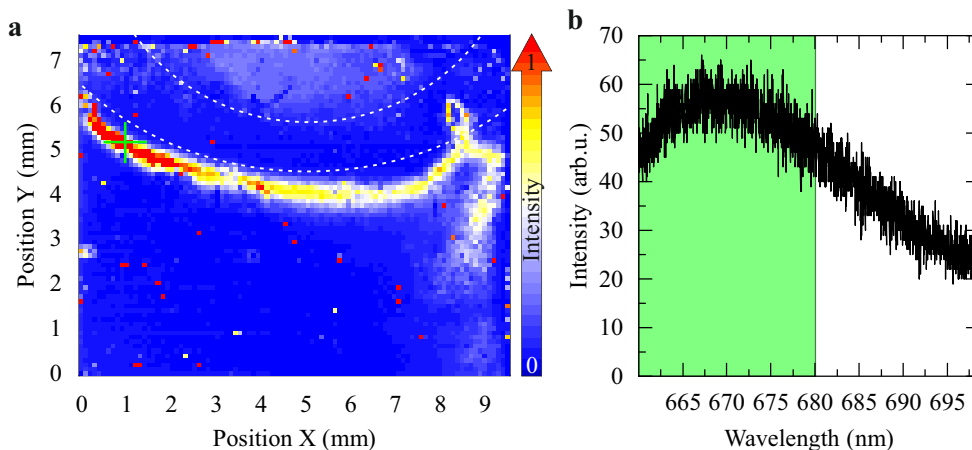


Figure 3.6: **a** | PL map of a typical sample after MoS_2 CVD growth. The white dashed lines illustrate the outline of the boat border. Areas of high PL intensity indicate monolayer MoS_2 . The green cross marks the position of the spectrum shown in **b**. **b** | Exemplary spectrum recorded at position (1 mm, 5.2 mm) in **a**. The green area indicates the area of the spectrum that has been integrated in every spectrum to obtain the intensity values in the map.

The resulting spatial monolayer MoS_2 distribution on the sample can be illustrated by a photoluminescence (PL) map. A typical PL distribution is depicted in Figure 3.6 **a**. The white dashed lines indicate the outline of the boat border. The faint blue region

²A solution of sulfuric acid and 30% concentrated hydrogen peroxide with ratio 3 : 1.

at the top of the map is bulk MoS₂, while higher PL intensities at the external side of the boat outline indicates monolayer MoS₂. The map is obtained by incrementally scanning the sample in x and y direction and recording a spectrum at every position. A exemplary spectrum at position (1 mm, 5.2 mm), indicated by the green cross, is shown in Figure 3.6 **b**. The green area illustrates the spectral area that has been integrated in every spectrum to obtain the intensity.

3.2.2. Electron beam lithography

Electron beam (e-beam) lithography is a standard method in nanotechnology to fabricate individually designed nanostructures when high throughput is not necessary [140]. A focused electron beam is scanned over an e-beam resist, e. g. polymethyl methacrylate (PMMA) or ZEP-520A (ZEP) [141]. In positive resists like these, electrons destroy the molecular chains locally and consecutive development erases the previously exposed areas. Negative resists invert the results, i. e. exposed areas remain on the substrate due to cross-linking of molecular chains, while untreated resist is dissolved during development. In this thesis, we predominantly use ZEP resist due to its strong dry etch resistance [141] accompanied by a good resolution of about 20 nm at a resist thickness of 380 nm. This is especially crucial for PCC fabrication.

For small structures, the so-called “proximity effect” needs to be considered. Due to back-scattered electrons, especially from the substrate, adjacent areas get exposed to a certain extend, which broadens the nominally defined structure. The proximity effect magnitude can be qualitatively estimated by the Rutherford differential cross section

$$\frac{d\sigma}{d\Omega} \propto \frac{Z^2}{E_0^2} \frac{1}{\sin^4(\theta)} \quad (3.7)$$

that gives us a measure for the probability of an electron of energy E_0 to be scattered at an atom with atomic number Z under an angle θ . According to Equation (3.7), scattering increases with the atomic number and decreases with the acceleration voltage, in particular.

The structure broadening can be characterized by the proximity function [142, 143], a sum of two or three Gaussian functions and, usually, one or two exponential functions, which describe the deposited energy density as a function of the distance from the incident electron beam. The free parameters of this function can be obtained, for example, by Monte Carlo simulations or by empirical methods. A Monte Carlo method is a computational algorithm based on a large number of independent random experiments (for example, the scattering events of single particles in matter) to obtain deterministic results based on the statistical outcome. The e-beam pattern construction software e_LINE [144] provides a Monte Carlo simulation module. Figures 3.7 **a** and **c** show simulated electron trajectories in a ZEP-SiO₂-Si material stack for acceleration voltages of 10 kV and

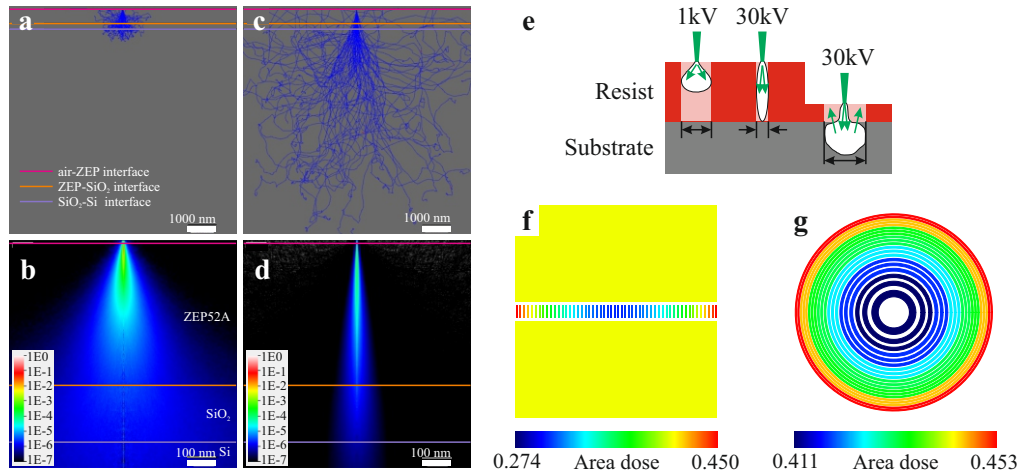


Figure 3.7.: **a** and **b** | Electron trajectories and energy density deposition in a stacked ZEP-SiO₂-Si material system for an acceleration voltage of 10 kV obtained through Monte Carlo simulations. **c** and **d** | Equivalent to **a** and **b**, but with 30 kV. **e** | Sketch of the energy density distribution in a resist-substrate system for low and high electron energies. The resolution is best for higher energies and sufficiently thick resist. **f** and **g** | Dose resolved e-beam pattern for PCC and FZP fabrication.

30 kV. Panels **b** and **d** show the respective deposited energy density (simulated for 10^5 electrons) in a magnified area. We observe that 30 keV electrons reach much further into the substrate than electrons of lower energy and experience far-reaching back-scattering in the substrate. Low-energetic electrons, however, experience large scattering already in the resist. The deposited energy density distribution for 10 keV electrons is, therefore, much broader than for 30 keV electrons. Figure 3.7 **e** summarizes these results in a sketch which shows the deposited energy (white areas) in a resist-substrate stack. Low voltages cause higher back-scattering in the resist than high voltages if the resist is of sufficient thickness. For that reason, we used the maximum possible voltage³ of 30 keV for fabrication. If the resist is too thin, however, back-scattering from the substrate is dominant for large voltages and strongly expose the resist from beneath. Therefore, a good agreement of resist thickness and acceleration voltage is necessary. In order to obtain the proximity function empirically, most methods rely on writing a matrix of certain structures [145] with varying area doses. Afterwards, the proximity parameters can be obtained from the relationship of dose to structure size.

In order to take the proximity effect into account, the area doses have to be adjusted. For larger contiguous input patterns, fragmentation into smaller polygons of different doses is often necessary. Areas with many or large adjacent exposition sites suffer from larger proximity effects than external areas of a structure and require, hence, lower nominal doses. In general, the e_LINE software is capable of both fragmentation and automa-

³Employed system: RAITH100, Raith GmbH, Konrad-Adenauer-Allee 8, 44263 Dortmund, Germany

tized dose calculation on the basis of the proximity parameters. Figure 3.7 **f** depicts the dose resolved pattern of a PCC and **g** the pattern of a FZP. However, automated fragmentation have turned out to be unfavorable for these patterns. Problems arise from occasional unexposed areas at the fragment boundaries or unintuitive fragmentation that can lead to a change of slow and fast scanning axis, e. g. within a “ladder hole”, (the software always chooses the longest side of a polygon as fast axis) causing imperfect boundaries. Additionally, the output fragments⁴ are exclusively polygons, which is particularly disadvantageous for writing circle structure like FZPs. We, therefore, have used a manual proximity correction for PCC fabrication by writing PCCs of five different periods with various doses and measuring the resulting rectangular hole sizes in the “ladder”. A 3D quadratic fit of the rectangle doses as a function of the crystal period and of the position from the center yielded the new dose distribution. We iterated this process until the result was sufficient.

3.2.3. Reactive ion etching

Inductively coupled plasma reactive ion etching (ICP-RIE) is a dry etch method and a standard process in micro- and nano-fabrication in both industry and research. The ionization of chemical reactants enables deep and highly anisotropic etching.

Figure 3.8 **a** shows a simplified setup of a typical ICP-RIE etching chamber. The reactants flow through the gas inlet into the chamber, which is evacuated to a pressure of 8.6×10^{-5} mbar. The sample is placed on an electrically isolated table that can be cooled with liquid nitrogen. The table serves as an electrode to which a RF voltage of 13.56 MHz is applied. The chamber hood is grounded. When the RF voltage is ramped up, electrons in the gas molecules start to oscillate, while the much larger ions cannot follow the oscillations. The gas is ionized and a plasma is created. Electrons that reach the hood walls are transmitted to the ground, whereas those reaching the table build up a negative charge and attract ions downwards to the sample surface. The plasma density can be strongly enhanced by a second RF voltage, the so-called ICP voltage, which is applied at a coil around the upper part of the chamber. The ICP voltage is of identical frequency as the bias voltage and generates a time-varying magnetic field, thus, inducing an electromagnetic force acting on the charge carriers. The interaction of the two RF sources enables versatile and decoupled control of ion current, i. e. the direct current (DC) bias, and ion energy [146].

⁴The fragmentation of e_LINE can be made visible as follows:

1. Go to *Exposure parameter* → *Enhanced exposure parameter* (which opens the *Exposure Details* window) → *Visualization* and check “Create ASCII debug file”
2. Start scan (or “Times” calculation)
3. Import the file `<e_LINE install folder>\User\Administrator\ExpoDebug.asc`

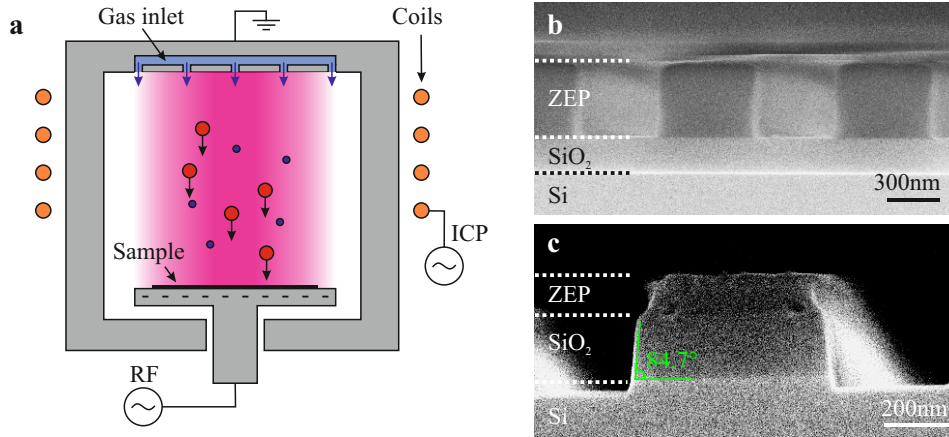


Figure 3.8: **a** | Sketch of a typical ICP-RIE setup. The gas flows into the evacuated chamber and gets ionized by applied RF voltages. The bias RF voltage applied to the sample holder predominantly causes the downward drift of the ions, while the ICP voltage applied at coils around the column induces time-varying magnetic field that constrict the plasma to reach higher densities. **b** and **c** | Etch test sample with stripe structures **b** before and **c** after the etch.

There are two etching types that can be separated [140]. The chemical etching relies on chemical reactions at the sample surface. It is mostly isotropic, very selective and does not require large ion energies. The physical etching is like sputtering the surface atoms. It is highly anisotropic, shows low selectivity and requires larger ion energies. Depending on the desired etching result, one has to find a good trade-off between both processes by adjusting the bias RF and ICP power, the gas fluence and composition, the chamber pressure, and the target temperature.

In this work⁵, we employ a $\text{CHF}_3 : \text{O}_2$ chemistry with a fluence ratio of 40 sccm : 1 sccm using 80 W bias RF power and 300 W ICP power to etch PCCs into SiO_2 (see Section 4.1). Figure 3.8 **b** shows a scanning electron microscope (SEM) image of an etch test sample in side view after e-beam. The ZEP stripes have a height of 380 nm sitting on the 200 nm SiO_2 layer and the Si substrate. Panel **c** shows a SEM image of the sample after a 100 s ICP-RIE etch. We observe that the SiO_2 has been completely erased between the stripes and even a bit of the Si substrate. A small layer of ZEP remains on top of the structures. The highlighted sidewall angle is close to ideal (84.7°). From the ratio of the removed resist and the removed SiO_2/Si substrate, we can calculate the selectivity, defined by the ratio of resist etch rate r_{resist} and substrate etch rate $r_{\text{substrate}}$. For our material system and optimized process parameters, we obtain a selectivity of

⁵Employed etching system: PlasmaPro 80 ICP by Oxford Instruments Plasma Technology, Yatton, Bristol, UK

$$\frac{r_{\text{ZEP}}}{r_{\text{SiO}_2}} = \frac{3.182 \text{ nm/s}}{2.417 \text{ nm/s}} = 1.32. \quad (3.8)$$

3.2.4. Silicon etching

Vapor phase xenon difluoride (XeF_2) is predominantly used in silicon industry to highly selectively etch a Si sacrificial layer in order to release SiO_2 or silicon nitride (SiN) nanostructures [147]. The etching is strongly isotropic. In the fabrication process of SiO_2 PCCs⁶, which is described in Section 4.1, we use XeF_2 etching to release the PCCs from the underlying Si and achieve free-standing structures.

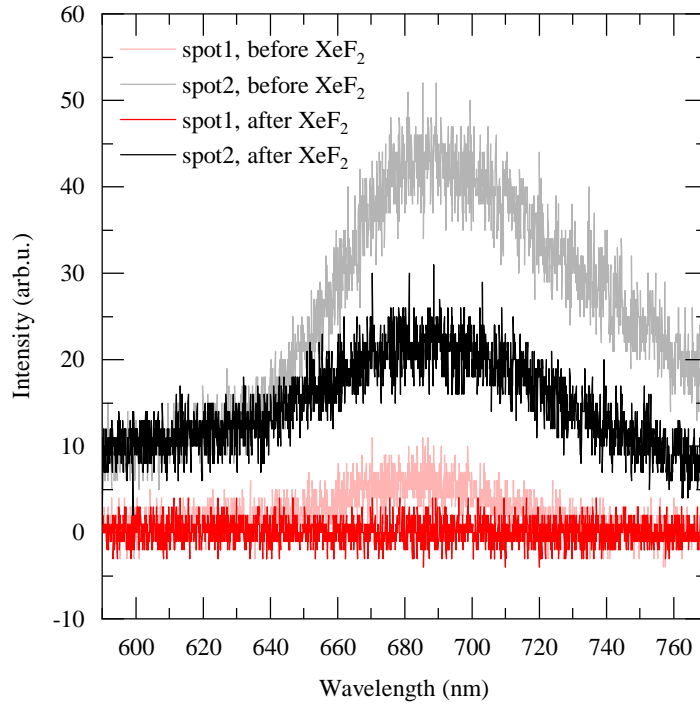
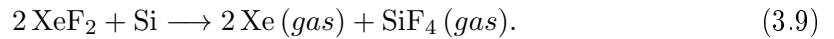


Figure 3.9.: MoS₂ PL spectra of two different sample sites (red and black curves) measured before (faint color) and after (bold color) XeF₂ gas exposure. The PL intensity is significantly decreased.

Si is one of a small number of materials that are etched by XeF₂. The chemical reaction is as follows:



⁶Xactix® e2 table-top etching system fabricated by SPTS, San José, CA 95131, USA

Other materials are germanium (Ge) or molybdenum (Mo) [148, 149]. For that reason, we investigated the impact on MoS₂. Figure 3.9 shows MoS₂ PL spectra of two different spots on the sample measured before (faint lines) and after (bold lines) XeF₂ exposure using the typical PCC etching parameters of 3 × 40 s at 2 Torr pressure. The PL intensity after the etch is significantly decreased. We relate this to a degradation of MoS₂ by XeF₂. Similar results have been also observed by other groups [150]. This MoS₂ degradation is one of the reasons for leaving the e-beam resist as passivation layer on the sample during PCC fabrication (see also Section 4.1).

3.2.5. Ion implantation

In order to fabricate VO₂ nanoclusters, V and O ions must be embedded into a substrate material which requires high kinetic energies. Here, this is achieved by ion implantation⁷. Figure 3.10 **a** depicts a sketch of the implanter, which has been adopted and slightly modified by Karl *et al.* [151]. Ions are extracted by a voltage of 10 keV from the source. The vanadium source consists of a vanadium powder that is attacked by hydrochloric acid (HCl) gas to form a vanadium chloride plasma. The oxygen source is carbon dioxide (CO₂) gas. In both cases, the mass spectrometer and a consecutive beam aperture separate the desired elements from foreign atoms and, also, unwanted isotopes or multiple charged ions. In the main chamber, the ions are accelerated by voltages up to 180 keV and are focused, thereafter, by a quadrupole lens. The beam is then scanned in *x* and *y* direction over the target wafer which is kept at room temperature for standard V and O implantation. During an implant process, movable shields can be used for site-selective implantation. The beam current is measured by four Faraday cups in the corners of an aperture in front of the target. In order to avoid channeling, i. e. an undesirable deep ion penetration into the target through atomic interstices that might appear, for example, in (100) Si, the target is tilted by 7°. Figures 3.10 **b** and **c** show photographs of the target holder carrying several 1 cm × 1 cm samples. The samples are separated by a mask (**b**) with contains holes slightly larger than the samples. Subsequently, the mask is covered by a plate (**c**) whose holes are slightly smaller than the samples to keep them in place when tilted into a vertical position.

Two of the most important parameters for implantation are the fluence, i. e. the number of ions per area, and the ion energy, which defines the implantation depth. We used fluences of $n_V = 9 \times 10^{16} \text{ cm}^{-2}$ and $n_O = 1.8 \times 10^{17} \text{ cm}^{-2}$, which require implantation times of several hours. While the fluence ratio of 1 : 2 is oriented towards the stoichiometry of VO₂ (although smaller changes can be favorable [128]), the fluence magnitudes are predominantly based on empirical values. The required ion energies can be obtained by simulation of the expected ion concentration in the target for a specified energy. Simulations are performed by the open-source software TRIM (“The Transport of Ions in Matter”) in the SRIM (“The Stopping and Range of Ions in Matter”) package [152],

⁷Group of Helmut Karl and Manfred Albrecht, Lehrstuhl für Experimentalphysik IV, Universität Augsburg, Germany

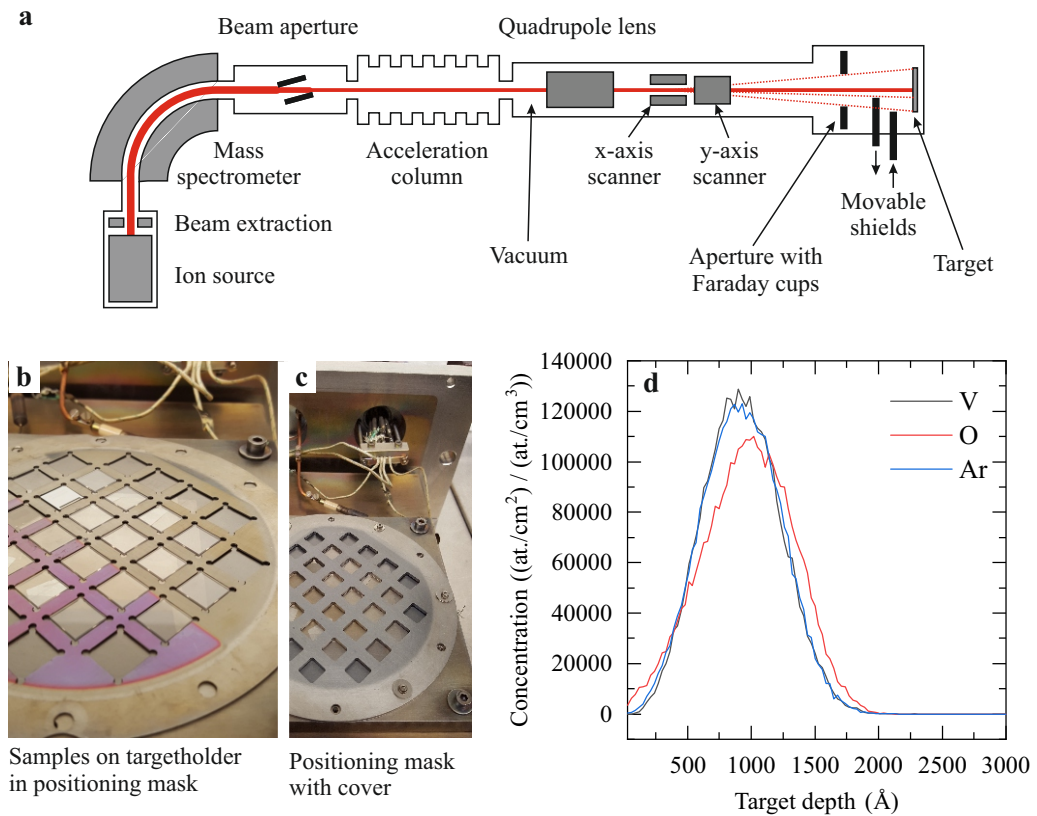


Figure 3.10.: **a** | Sketch of the ion implanter. The ion beam (red) is extracted from the source and filtered by the ion charge/mass ratio in a magnetic field. After passing an aperture, ions can be accelerated up to 180 keV, are focused, and scanned over the target. **b** | Photograph of the samples in a positioning mask on the targetholder. **c** | Samples secured by the mask cover. **d** | Simulated ion concentration of V and O for implantation energies $E_V = 100$ keV and $E_O = 36$ keV as a function of the target depth. The energies are chosen in such a way as to achieve a large overlap of both distributions and a projected range of 100 nm.

which calculates the interactions of energetic ions with amorphous targets on the basis of Monte Carlo methods. Figure 3.10 **d** shows the ion concentration for both V and O (the argon (Ar) distribution will be treated in the following paragraph) using the energies $E_V = 100$ keV and $E_O = 36$ keV that have been also employed in several other works [67, 128, 130]. These energies have been chosen to obtain a large overlap of both distributions, which is crucial for compound crystal formation, and a projected range, i. e. the depth of maximum concentration, of 100 nm. For nanocluster formation and defect healing, the sample has to be rapidly annealed to a temperature of 950 °C in a successive step. The ramping time of this rapid thermal annealing (RTA) process is 17 s, while the cooling time is 1 min.

Site-selective nanocluster formation can be achieved by either using a shadow mask during the V and O implant process or site-selective deactivation of a homogeneously implanted layer [67, 130]. According to [67], we call structures fabricated in the former process “directly synthesized (DS)” and in the latter one “selectively deactivated (SD)”. The deactivation process is realized by Ar ion implantation and is also employed for sample fabrication in this work. The whole fabrication process is depicted in Chapter 5. For that reason, we additionally show an Ar concentration profile in Figure 3.10 **d** which results from an ion energy of $E_{Ar} = 80$ keV. This energy is chosen for optimal projected range matching with V and O in order to achieve the most efficient deactivation effect.

3.3. Optical measurements

This section describes optical methods that are employed to characterize and investigate both solid semiconductors and photonic nanostructures. Of particular importance among these methods is μ -PL. It provides a rather simple, but powerful way to observe cavity mode coupling with monolayer MoS₂ emission (see Chapter 4). Raman spectroscopy is mainly used to investigate crystal structures. In this thesis, we employ Raman spectroscopy on both MoS₂ to determine film thickness and quality and on embedded VO₂ nanocrystals in SiO₂ to verify crystal stoichiometry and phase transition of the material. In Section 3.3.3, we introduce several setups for transmission measurements on both large-area and locally implanted VO₂/SiO₂ samples.

3.3.1. Photoluminescence spectroscopy

Photoluminescence (PL) is the emission of a photon by a system that has been previously excited by a photon of higher energy. Spectrally resolved PL intensity measurements are the principle investigation method in this thesis.

Figure 3.11 **a** shows the optical excitation (blue arrow) of an electron (blue circles) within a typical direct-bandgap semiconductor in momentum space (k -space). Whenever the excitation energy $\hbar\omega_{exc}$ is larger than the bandgap E_g , it is lifted from the valence

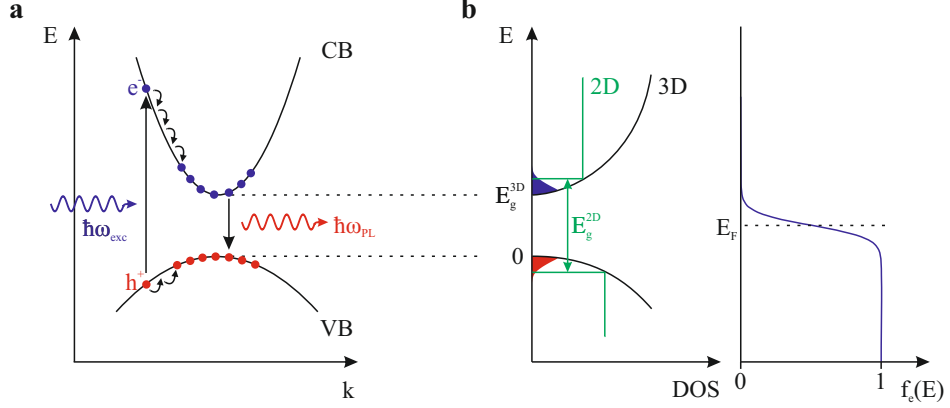


Figure 3.11: **a** | Photoluminescence in a typical direct semiconductor. An incident photon (blue arrow) with an energy larger than the band gap creates an electron-hole pair (blue and red circles) by lifting an electron from the VB to the CB. After relaxation of the charge carriers to the band extrema, they recombine under emission of a photon with about the band gap energy (red arrow). **b** | Density of states (DOS) of a 3D (black lines) and 2D (green lines) semiconductor around the band gap. Due to confinement in lower dimensional systems, the band gap is slightly increased. The blue (red) area shows the occupancy of electrons (holes) which is the product of density of states (DOS) and Fermi-Dirac statistics $f(E)$, which is sketched on the right for electrons. E_F is the Fermi energy of electrons in the conduction band.

band (VB), the highest band in the band structure with completely occupied states, to the conduction band (CB), the lowest band which is not completely occupied. The positively charged defect in the VB that the electron leaves behind is called “hole” (red circles). After separation of the charge carriers, they rapidly relax to their respective band extremum or the energetically lowest (for holes: highest) unoccupied state and recombine under emission of a photon with the energy $\hbar\omega_{\text{PL}} \approx \hbar\omega_g$. Typical phononic relaxation times are 100 fs and, hence, much faster than radiative lifetimes, which are typically in the range of pico- or nanoseconds [153]. We will neglect the formation of excitons in this section and will treat PL principles only in the single particle picture.

Figure 3.11 **b** depicts the density of states (DOS) $g(E)$ of a 3D system (black lines) and the occupancy of electrons in the CB (blue area) and, respectively, of holes in the VB (red area). The 3D DOS (in this case shown for electrons) is given by

$$g_{3\text{D}}(E) = \frac{1}{2\pi^2} \left(\frac{2m_e^*}{\hbar^2} \right)^{\frac{3}{2}} \sqrt{E - E_g} \quad (3.10)$$

with the effective electron mass m_e^* [153]. Then, the number of charge carriers is the product of $g(E)$ and Fermi-Dirac statistics $f(E)$. The right panel of Figure 3.11 **b** schematically depicts $f(E)$ for electrons. Since this work especially deals with 2D mate-

rials, the 2D DOS is depicted in green in Figure 3.11 **b** as a reference. Due to quantization in one dimension, $g_{2D}(E)$ is not a square root function any more, but a step function. The increase of E_g can be explained by considering the energy levels of a particle with mass m^* in an infinite quantum well of width d

$$E_n = \frac{\hbar^2 \pi^2 n^2}{2m^* d^2}. \quad (3.11)$$

The lowest energy level $n = 1$ has a finite ground state energy. Hence, the 2D DOS does not start exactly at the bandgap edge of a volume crystal, but consequently leads to a slightly larger bandgap E_g^{2D} [91].

In order to obtain a theoretical expression for the PL spectrum, we start with the transition probability between a state 1 and a state 2 of energy difference $\hbar\omega$, which is given by ‘‘Fermi’s Golden Rule’’ [113, 153]

$$W_{1 \rightarrow 2} = \frac{2\pi}{\hbar^2} |M_{12}|^2 g(\hbar\omega) \quad (3.12)$$

with the transition matrix element $M_{12} = \langle 2 | H' | 1 \rangle$ and the final DOS $g(\hbar\omega)$. For the perturbation operator H' caused by the incident light wave, we can employ the electric dipole interaction as an approximation

$$H' = -\mathbf{p}_e \cdot \mathbf{E}_0 \quad (3.13)$$

with the electric dipole moment of an electron $\mathbf{p}_e = -e\mathbf{r}$ and the electric field amplitude \mathbf{E}_0 . Under knowledge of the initial and final eigenstates, $W_{1 \rightarrow 2}$ can be directly calculated. The matrix element will vanish, in particular, if the optical selection rules of the transition are not fulfilled. The selection rules result from the states’ change in both parity and the quantum numbers of the orbital angular momentum l , its projection m_l , and spin m_s [154]. For the electric dipole approximation, they can be summarized by

1. The parity of initial and final state must change.
2. $\Delta l = \pm 1$.
3. $\Delta m = 0, \pm 1$.
4. $\Delta m_s = 0$.

In summary, the PL intensity I at a specific energy $\hbar\omega$ is the transition probability times the probability that state 1 (in the conduction band) is occupied and state 2 (in the valence band) is empty [153]. In a semiconductor and without exciton formation, the occupancy in the conduction band is given by the Fermi-Dirac statistics of electrons $f_e(E)$ and the number of unoccupied states is given by the Fermi-Dirac statistics of holes $f_h(E)$, yielding

$$I(\hbar\omega) = W_{1\rightarrow 2} f_e(\hbar\omega) f_h(\hbar\omega). \quad (3.14)$$

Micro-Photoluminescence

For measurements on nanostructures, it is important to spatially precisely excite and detect the light on the sample. This method is called micro-photoluminescence (μ -PL). In Chapter 4, μ -PL spectroscopy is used for characterizing hybrid PCCs. In those measurements, it is crucial to selectively excite a single cavity and spatially limit the detection area to reduce background emission originating from stray light that hasn't coupled to the cavity.

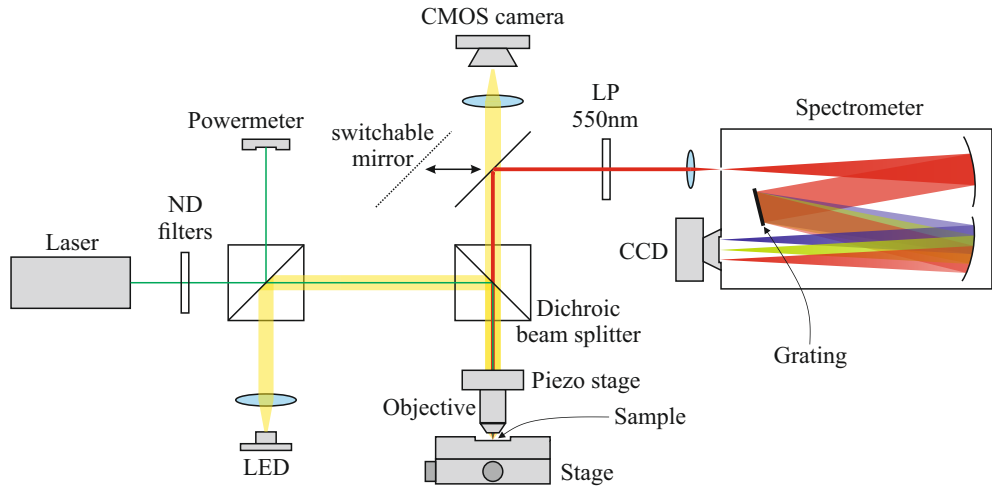


Figure 3.12.: Setup for μ -PL spectroscopy. The 514 nm diode laser for excitation is attenuated to a power of $50 \mu\text{W}$, guided through a dichroic beam splitter with a cut-on wavelength of 550 nm and focused by a microscope objective onto the sample. PL emission is collected by the same objective and filtered first by the dichroic beam splitter and second by an additional 550 nm longpass filter to extinct the reflected laser light. Finally, it is spectrally analyzed in a 0.5 m grating monochromator equipped with a liquid nitrogen cooled CCD camera. Imaging is enabled by a LED which is coupled into the beam path by an additional 50 : 50 beam splitter. The LED light can be guided to a CMOS camera by opening a switchable mirror in the detection path.

Figure 3.12 illustrates the employed optical setup. The excitation laser is a green diode laser with a wavelength of $\lambda = 514 \text{ nm}$, which is attenuated by neutral density (ND) filters to a maximum power of $50 \mu\text{W}$. After passing a beam splitter used for power detection and the incoupling of an additional light source, the beam is reflected by a dichroic beam splitter with a cut-on wavelength $\lambda_{\text{cut-on}}$ of 550 nm, which means that wavelengths $< \lambda_{\text{cut-on}}$ get reflected and wavelengths $> \lambda_{\text{cut-on}}$ get transmitted. It is subsequently focused onto the sample by an infinity corrected microscope objective with

a $40\times$ magnification and a numerical aperture $NA = 0.6$. The diffraction limited laser spot has a diameter of about $1\ \mu\text{m}$. In order to precisely position the beam spot on the sample, the objective is carried by a three-axis piezoelectric stage⁸. The piezoelectric stage allows movements in the range of $100 \times 100 \times 100\ \mu\text{m}^3$ with a resolution in the sub-nm regime. Coarse positioning and large area scans are performed by an electrified two-axis stage that carries the sample holder.

PL emission is collected by the same objective, then filtered by the dichroic beam splitter and an additional longpass filter with $\lambda_{\text{cut-on}} = 550\ \text{nm}$ and focused on the entrance slit of the spectrometer, which is set to a width of $100\ \mu\text{m}$. The monochromator unit of the spectrometer consists of two parabolic mirrors with focal lengths of $0.5\ \text{m}$. The first mirror collimates the light and reflects it onto a 1200 lines grating. The grating angle is adjusted in a way that the first order of the diffracted light beam is collected by the second mirror and focused onto a liquid nitrogen cooled CCD detector chip.

For imaging, we use a red or white LED lamp. The imaging light (yellow beam in Figure 3.12) is slightly collimated by a lens and coupled into the beam path by a $50 : 50$ beam splitter. The imaging signal is detected by a typical CMOS camera when the switchable mirror is moved out of the PL detection beam path.

3.3.2. Raman spectroscopy

Raman spectroscopy provides access to a “phonon fingerprint” of solid state materials. It is a very sensitive, fast, and non-destructive method to examine a variety of properties. For material syntheses with numerous compound products, it is, hence, a powerful tool to verify the correct material composition (cf. subsection “Vanadium dioxide Raman measurements”). In the same subsection, we will also describe how to verify the temperature dependent phase change of VO_2 . In the field of 2D materials, Raman spectroscopy is especially useful to determine the number of layers, which has been demonstrated, in the case of MoS_2 , for up to 6 layers [98]. Raman spectroscopy has been furthermore employed to gain information about, for instance, temperature [155], charge carrier density [156], or defect density [157] of the material.

Raman scattering is the inelastic scattering of photons with phonons. Figure 3.13 a shows a typical phonon dispersion relation containing the acoustic phonon band (at lower energies) and the optical phonon band (at higher energies). For light frequencies, Raman scattering can only occur near the Brillouin zone center in an area of $10^{-4}\ \pi/a$ to $10^{-3}\ \pi/a$, which is indicated in yellow (the width of this area is highly exaggerated). The photon scattering process with acoustic phonons is called “Brillouin scattering” and with optical phonons “Raman scattering”. Since the frequency shifts at Raman scattering are larger than at Brillouin scattering, it is much easier to observe. Near the crossing point of phonon band and light line, direct absorption (infrared (IR) absorption) or resonant Raman scattering can occur. IR-active modes require a polar crystal, i.e. ionic binding

⁸TRITOR101, piezosystem jena GmbH

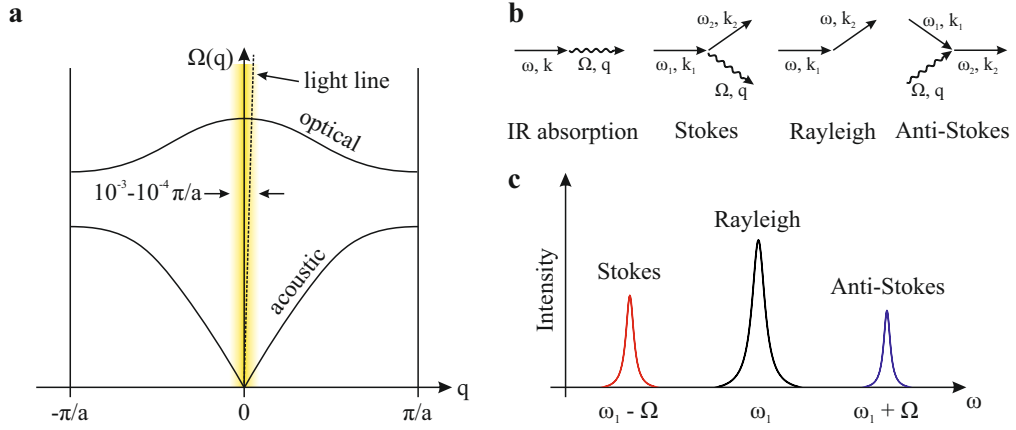


Figure 3.13: **a** | Phonon band structure containing acoustic and optical branches and the light line (dashed). Inelastic light scattering can only occur near the yellow shaded area. **b** | Various processes that can occur for an incident photon: IR absorption, Raman scattering by phonon emission (Stokes process), elastic light scattering (Rayleigh process), Raman scattering by phonon absorption (Anti-Stokes process). **c** | Sketch of a typical Raman spectrum containing the Rayleigh peak, the Stokes peak at lower energy and the Anti-Stokes peak at higher energy.

character of the atoms [153]. Raman scattering, on the other hand, is only observable for Raman-active modes. To figure out, whether a phonon mode is Raman active or not, group theory considerations are necessary [158] which are beyond the scope of this work. However, for materials with a centrosymmetric unit cell, symmetry considerations can be employed to show that IR-active and Raman-active modes are complementary [153]. In unit cells without inversion symmetry, phonon modes can be both IR and Raman active.

Figure 3.13 **b** depicts sketches of possible processes that might occur when a photon of energy $\omega_{(1)}$ and wave vector $\mathbf{k}_{(1)}$ impinges onto a crystal. In the case of IR absorption, the photon vanishes completely and a phonon with energy Ω and wave vector \mathbf{q} is emitted. Rayleigh scattering is the elastic scattering at the crystal without energy change of the photon. In the case of inelastic photon scattering, the outgoing photon (ω_2, \mathbf{k}_2) has changed its energy due to phonon emission (Stokes process) or absorption (Anti-Stokes process). Hereby, we simplify the interaction sketch and neglect exciton generation and annihilation during the scattering process. Since conservation of energy and momentum are required, we can write

$$\omega_1 = \omega_2 \pm \Omega \quad (3.15)$$

$$\mathbf{k}_1 = \mathbf{k}_2 \pm \mathbf{q}. \quad (3.16)$$

A typical Raman spectrum of a single atom base material, as depicted in Figure 3.13 c, shows three signal peaks. The center peak stems from (elastic) Rayleigh scattering, the peak at lower energies contributes to the Stokes process and the higher energy peak to the Anti-Stokes process. Both Raman peak intensities are highly exaggerated with respect to the Rayleigh peak.

In order to measure Raman scattering, high spectral resolution and high laser suppression is necessary. An effective laser line filter can be realized either by double or triple grating spectrometers or, in more recent times, by so-called “edgepass” filters that provide extremely sharp transmission changes at the cut-on or cut-off wavelengths. Although the actual Raman scattering process does not immediately depend on the laser wavelength for visible light, it is favorable to use smaller wavelengths for high signal intensity since the scattering efficiency scales with ω^4 for $\omega \gg \Omega$ (we don’t consider resonant Raman spectroscopy) [115]. Additionally, narrow bandwidths and rather high output powers of typically a few 10 meV are necessary. For that reason, many Raman lasers are in the green spectral range.

In this thesis, we solely measured Stokes processes and used both a Ar^+ laser at a wavelength of 514.5 nm and a diode pumped solid state laser at 532 nm for Raman measurements. A Raman setup can be basically structured like the μ -PL setup shown in Figure 3.12. The most important difference is the obligatory need of an edgepass filter in detection and a narrow band laser source.

MoS₂ Raman measurements

Monolayer MoS₂ shows three Raman-active phonon modes, but only two of them, the so-called E_{2g}^1 and A_{1g} mode, are experimentally easily accessible due to a very high phonon DOS close to their energies [159]. Figure 3.14 shows a typical Raman spectrum⁹ of CVD-grown monolayer MoS₂ on a 300 nm SiO₂/Si substrate. The peaks at wave numbers 385.95 cm⁻¹ and 404.49 cm⁻¹ clearly coincide with the two mode frequencies of monolayer MoS₂ [98, 159]. The large peak at 521.47 cm⁻¹ stems from the Si substrate [160]. The upper inset shows a microscope image of the investigated area with the laser spot position marked by the green cross. The dark purple areas are monolayer MoS₂, while the light pink area is pure substrate. The MoS₂ distribution shows a thickness gradient as typical for CVD growth: from multilayer MoS₂ (on the left) over monolayer film to

⁹This measurement was performed in the laboratories of Ludwig Bartels’ group, UCR.

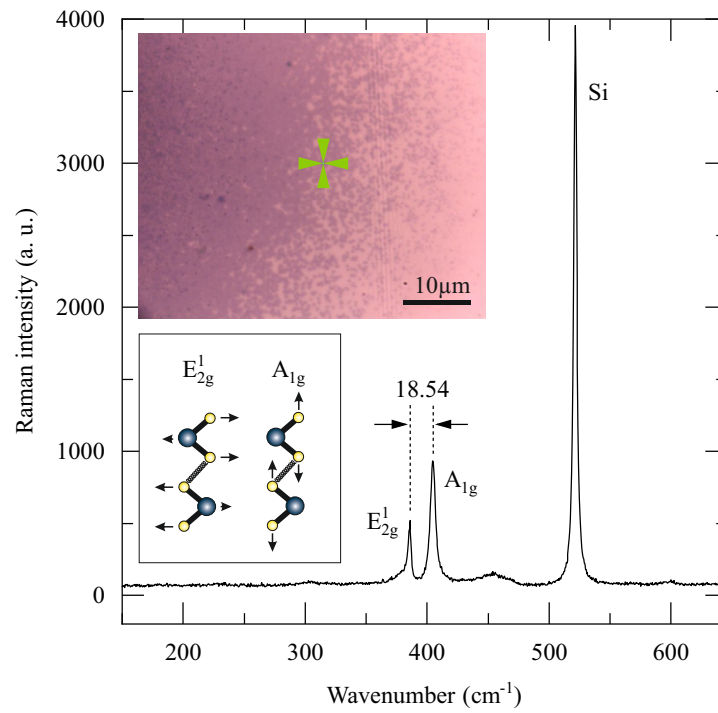


Figure 3.14. A typical Raman spectrum of monolayer MoS₂ showing the characteristic E_{2g}^1 and A_{1g} peaks. The large peak at 520 cm^{-1} stems from the Si substrate. The upper inset shows the position on the sample (green cross) at which the Raman spectrum is recorded. Dark purple areas are monolayer MoS₂, light pink areas are pure substrate. The lower panel illustrates the atomic oscillations in the case of the two prominent Raman-active modes.

flake formation (in the right half of the image). The lower inset in Figure 3.14 sketches the oscillation directions of the two Raman-active modes in a bilayer. E_{2g}^1 corresponds to an in-plane oscillation and A_{1g} to an out-of-plane oscillation. Unlike further modes that exist in bulk MoS₂, the sulfur atoms move against the molybdenum atom while the coupling between the layers (indicated by the spring) is rather low. For that reason, these modes can also propagate in a monolayer.

Interlayer coupling changes the mode energies in multilayer systems. For that reason, the spectral distance of the Raman peaks is of special interest since they can imply the number of layers. With increasing number of layers, the E_{2g}^1 mode energy decreases (the Stokes-peak shifts to the right), while the A_{1g} mode energy increases (the Stokes-peak shifts to the left). As a rule of thumb, a peak distance of $< 20 \text{ cm}^{-1}$ is a strong indication of monolayer MoS₂. This condition is clearly fulfilled in Figure 3.14. An investigation of the peak distances for monolayer, few-layer, and bulk MoS₂ reveals a monotonic increase from about 19 cm^{-1} for monolayers to about 25.5 cm^{-1} for bulk [98]. In this study, it has been possible to distinguish between up to 6 layers, while the differences between layers 1, 2 and 3 are the most prominent.

VO₂ Raman measurements

Raman spectroscopy on VO₂-SiO₂ samples can give indication of the vanadium and oxide compounds within the nanocrystals that have been formed during the annealing process (see Section 3.2.5).

Figure 3.15 **a** shows Raman spectra¹⁰ of VO₂ nanocrystals embedded in a fused silica substrate at various temperatures. The temperature cycle consists of a heating process from room temperature to about 100 °C and a cooling process back to room temperature. The analysis of the peak positions is based on measurements from Rafe [128] and other works [161, 162]. Besides the VO₂ signature peaks at 200 cm^{-1} , 224 cm^{-1} and 637 cm^{-1} (bold bordered labels), the sample also shows strong peaks originating from V₂O₅, c.f. also [128], which doesn't cause negative effects on the existing VO₂ compounds. However, a low amount of V₂O₅ is favorable in order to increase the amount of VO₂.

Figure 3.15 **b** shows the peak area of the three VO₂ signature peaks (after background correction) as a function of temperature. They clearly show a hysteresis with a critical temperature $T_C \approx 70 \text{ °C}$ in the heating branch and the reverse phase transition at 50 °C in the cooling branch. The disappearing of the room temperature VO₂ peaks at elevated temperatures demonstrates the crystal structure change in the material, which is discussed in detail in Section 2.4. The distinct peak intensity changes prove that there is a sufficient amount of VO₂ in our sample to observe a phase transition and the large hysteresis indicates that nanocluster formation has been successful.

¹⁰These measurements were performed in the laboratories of Helmut Karl's group, Experimentalphysik IV, Augsburg University

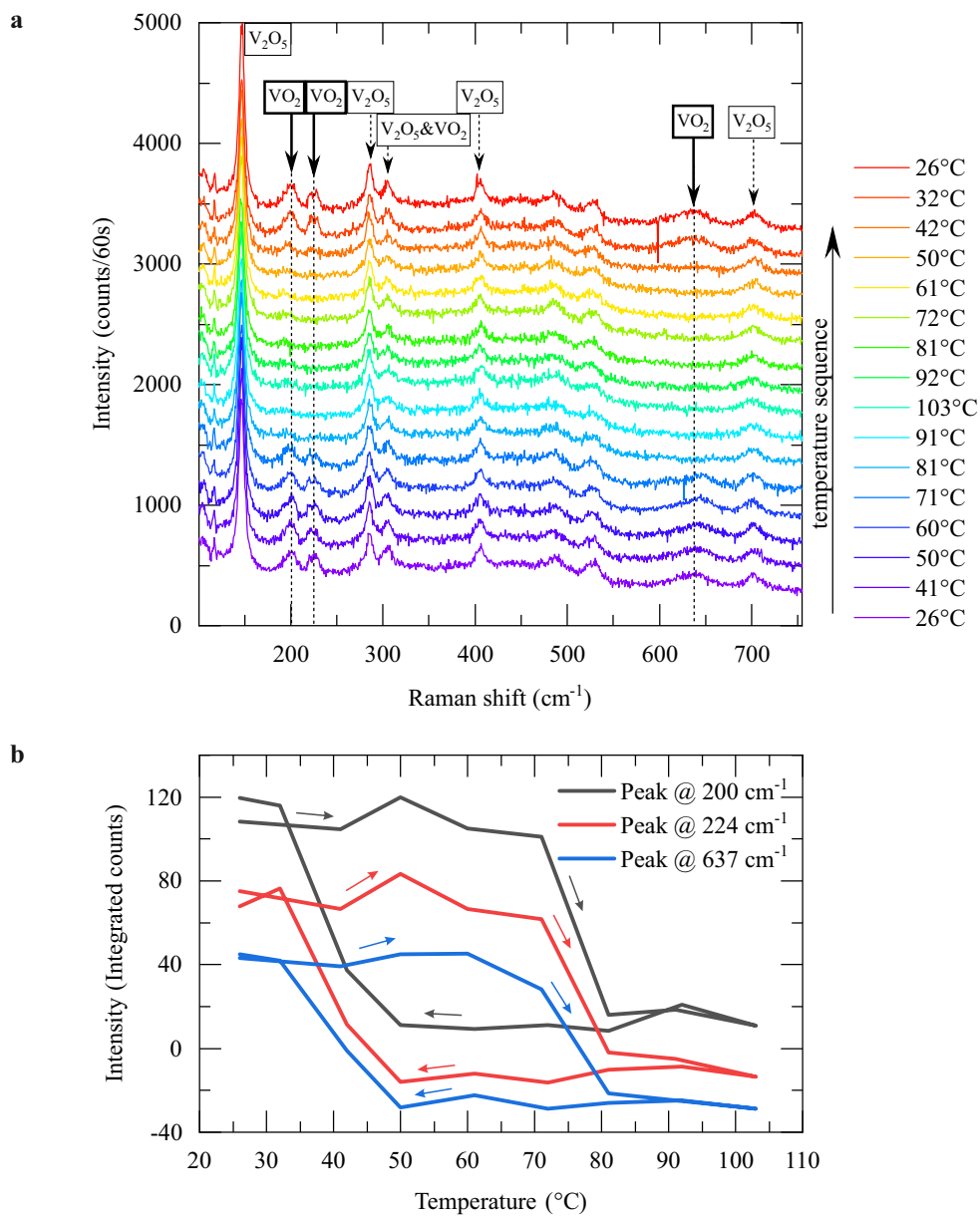


Figure 3.15.: **a** | Raman spectra of VO_2 nanoclusters for a temperature sequence $26^{\circ}\text{C} \rightarrow 103^{\circ}\text{C} \rightarrow 26^{\circ}\text{C}$. The dashed lines indicate the relevant VO_2 peaks. **b** | The peak areas of the three VO_2 lines as a function of the temperature show a large hysteresis with MITs at about 70°C and 50°C .

3.3.3. Direct transmission measurements

In the following section, we want to consider transmission measurements of VO₂ implanted fused silica samples. In order to verify a notable transmission change due to the VO₂ phase transition, which is required for later measurements (see Chapter 5), we perform direct transmission measurements. Such a configuration requires the ability to precisely measure small intensity changes. For this purpose, a lock-in amplifier together with a gated laser are typically employed.

Figure 3.16 **a** illustrates the direct transmission setup. We use a gated diode laser of wavelength $\lambda = 1550$ nm as light source, whose beam diameter is slightly narrowed by a pinhole, and an InGaAs photodetector to measure the intensity after the sample. The detector outputs a voltage which is proportional to the incident light power at a given wavelength. The output is connected to the signal input of a lock-in amplifier. The sample is carried by a copper sample holder which is placed on a Peltier element for temperature control. A signal generator triggers the laser with a square-wave signal, which also serves as a reference for the lock-in amplifier. The processing of measurement signal and reference finally yields a DC voltage that is proportional to the signal amplitude. The voltage is indicated by a gauge and additionally read out by a computer. Figure 3.16 **b** displays the functionality of a lock-in amplifier in more detail. At first, the user needs to lock the reference (for simplicity, we assume a sine wave of angular frequency ω) to the measurement signal (of the same frequency, but with a lot of noise) by applying a phase shift to the reference. This is done by maximizing the time integrated output signal. In a next step, both signals get multiplied, which yields a purely positive signal of double the frequency of each signal. In the frequency domain, this corresponds to a peak at $\omega - \omega = 0$ and at $\omega + \omega = 2\omega$. Time integration, which is realized by a low-pass filter, erases the frequencies $\omega > 0$ and outputs a DC signal that is proportional to the amplitude of the input signals. A temperature dependent direct transmission measurement on VO₂ nanoclusters is shown in Figure 2.13.

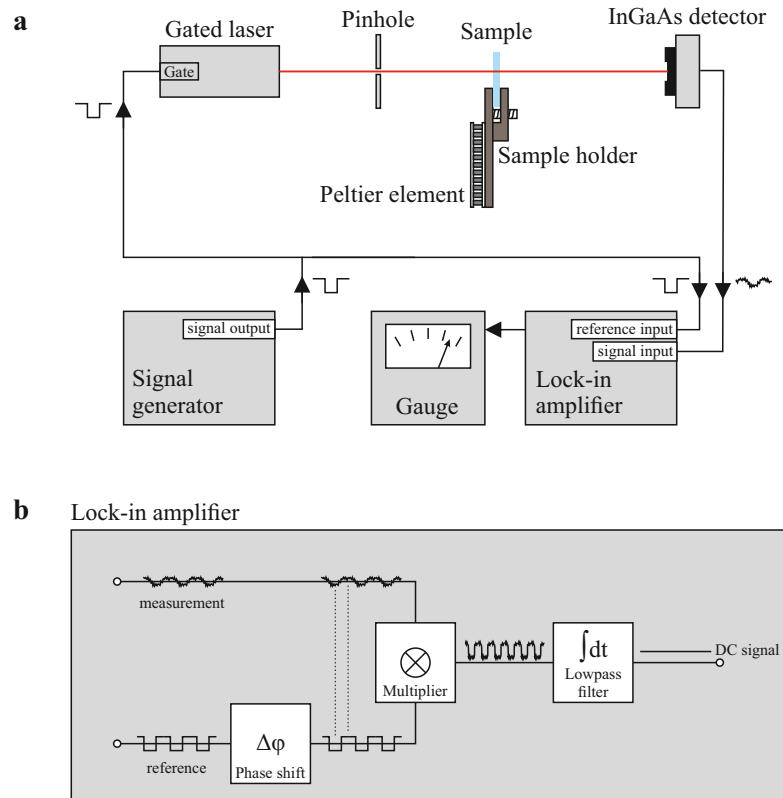


Figure 3.16.: **a** | Setup for temperature-dependent direct transmission measurements. The transparent sample is carried by a copper holder that is connected to a Peltier element for temperature control and positioned in a NIR laser beam, which is subsequently detected by an InGaAs photodiode. The gated laser is triggered by a square-wave signal. Both reference signal from the laser trigger and measurement signal from the photodetector are merged in a lock-in amplifier and converted into a DC voltage that is proportional to the input signal amplitude. **b** | Principle setup of a lock-in amplifier in time domain. The reference signal (bottom path) has to be phase matched to the measurement signal by applying a phase shift. Both signals get multiplied which yields a purely positive signal of twice the frequency. A low-pass filter then filters the DC component out of the signal, which corresponds to an integration in time. The output voltage is linear to both of the input amplitudes.

4 | Photonic crystal cavities

The concept of photonic crystals has been introduced in Section 2.2. There, we also motivate the “ladder”-type SiO_2 photonic crystal cavity (PCC) design employed in this work, that was initially created by Gong *et al.* [116]. The 1D beam layout primarily supports light confinement in 2 dimensions due to total internal reflection which enhances the Q -factor for our choice of material. Given fabrication constrictions of the design, regarding the membrane thickness of 200 nm, are discussed later in Section 4.1.

This chapter¹ deals, firstly, with the fabrication of free-standing hybrid devices, i. e. PCCs that are coupled to monolayer MoS_2 , secondly, with the detailed analysis of a single PCC emission spectrum and, thirdly, with geometric tuning of the cavity mode. Finally, we also compare our measurements with FDTD simulation results. The basic concepts and software parameters of these simulations are described in detail in Section 3.1.

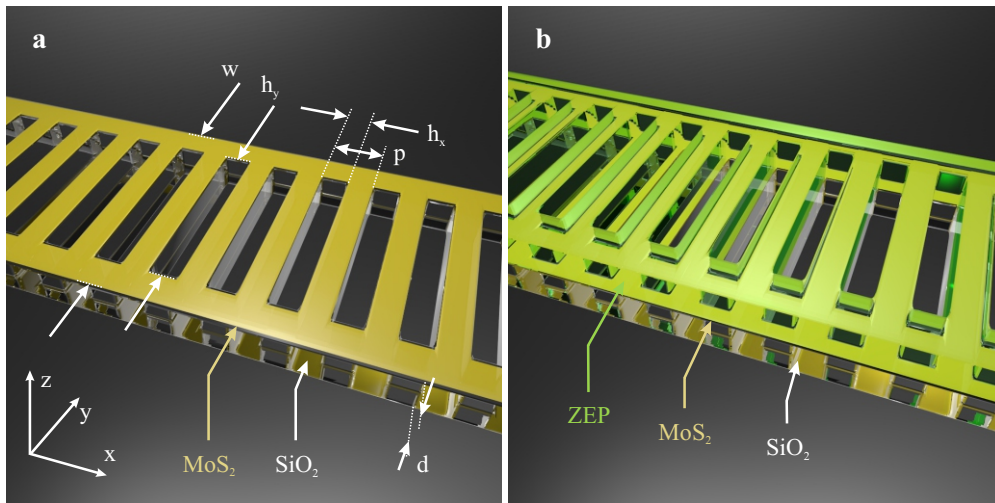


Figure 4.1.: Layout of a PCC. **a** | Monolayer MoS_2 (yellow) is located on top of the SiO_2 structure. The labels are consistent to Figure 2.7. **b** | Monolayer MoS_2 is encapsulated between SiO_2 and a layer of ZEP e-beam resist (greenish).

Figure 4.1 **a** illustrates the basic layout of a free-standing PCC with monolayer MoS_2 (yellow) on top. All parameter names are adopted from Figure 2.7 **a**. In this approach, optical pumping of the cavity does not arise from the light source inside the structure,

¹This chapter is based on results that have been published in [18].

which stands in contrast with our (idealized) simulation approach (see Section 3.1). However, an embedded monolayer is clearly preferable in terms of coupling efficiency. Figure 4.1 b shows a triple layer approach with a supplementary layer of electron beam (e-beam) resist on top of the monolayer. This image illustrates the actual fabricated device with monolayer MoS₂ encapsulated between SiO₂ membrane and resist layer. The benefits of this approach, concerning the fabrication process, are discussed in detail in Section 4.1. The positive effect of an increased membrane thickness on the Q -factor will be further examined in Section 4.3.

4.1. Fabrication of hybrid devices

Figure 4.2 a describes the five basic fabrication steps in a sketch. Step 1 (material growth) is conducted by our collaboration partners at the University of California Riverside² [18]. It starts with a commercially available Si substrate that is thermally oxidized to a depth of 200 nm from the surface. The substrate is carefully cleaned with piranha solution³ to avoid contamination by organic material. The chemical vapor deposition (CVD) growth process takes place inside a glass tube that is gradually heated and cooled over time. On the substrate surface, the precursors molybdenum trioxide (MoO₃) and sulfur (S) react to MoS₂ and, ideally, form a monolayer. A detailed discussion of CVD growth is given in Section 3.2.1.

Step 2 (spin coating of e-beam resist) determines the begin of the PCC fabrication. In this section, we will only focus on the principles of the subsequent fabrication steps. The exact parameters of the entire fabrication process are listed in Appendix A.1. First, we produce an etch mask by e-beam lithography. After careful cleaning of the sample with nitrogen gas, the e-beam resist ZEP-520A (ZEP)⁴ is spin-coated onto the sample (step 2). We have measured a resist thickness of 380 nm. ZEP is a positive resist and is preferred to PMMA due to its much higher dry etch resistance while their spatial resolution is comparable [141].

In step 3, the desired pattern is written into the resist by focussed electron beam exposure which is described in detail in Section 3.2.2. The sample is developed in a 50:50 mixture of pentyl acetate and methyl isobutyl ketone (MIBK), followed by two dipping steps in pure MIBK and isopropyl alcohol (IPA) for development stopping and cleaning. In order to improve the etch resistivity of the ZEP resist, we perform a hardbake after development [141, 163, 164].

In step 4 (dry etching), we transfer the pattern into the underlying MoS₂ and SiO₂ layers by inductively coupled plasma reactive ion etching (ICP-RIE) using a CHF₃ : O₂

²Group of Ludwig Bartels, Department of Chemistry and Materials Science & Engineering Program, University of California, Riverside, California, 92521, USA

³A solution of sulfuric acid and 30% concentrated hydrogen peroxide with ratio 3 : 1.

⁴Manufacturer: Zeon Chemicals L. P. (www.zeon.co.jp)

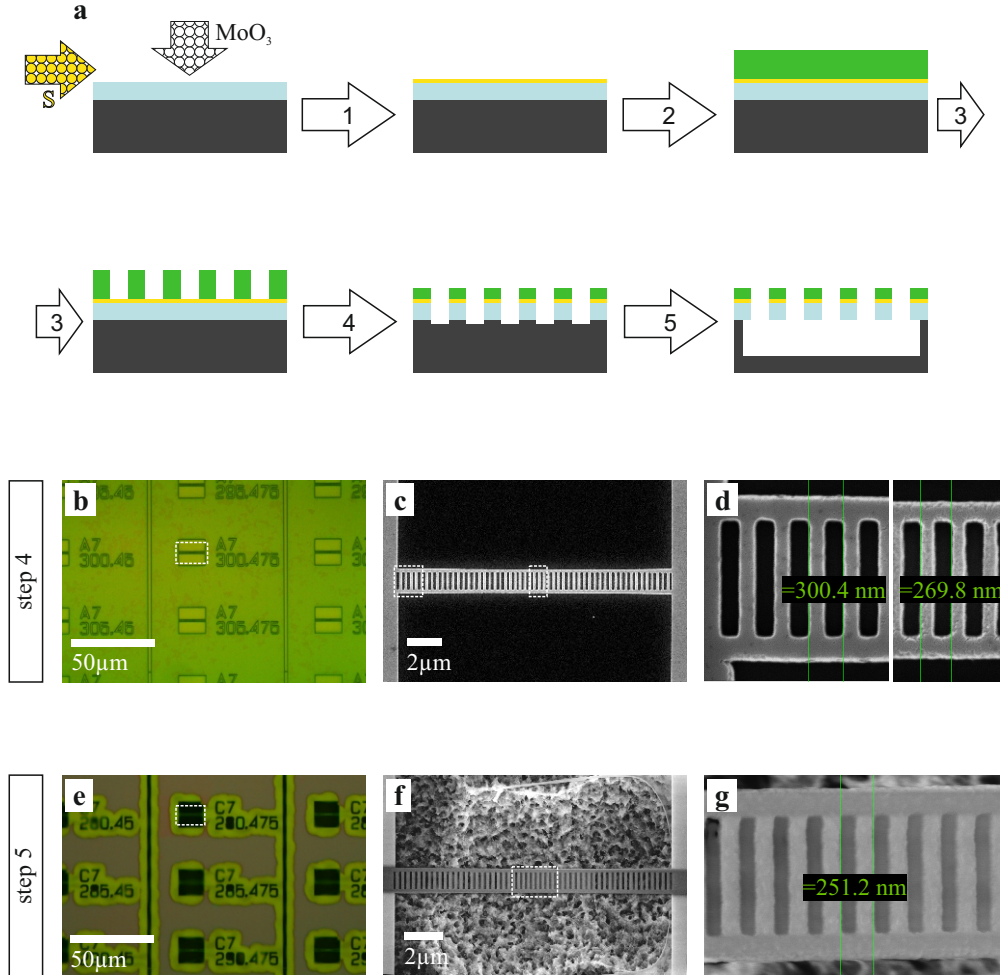


Figure 4.2.: **a** | The fabrication process consists of five major steps: (1) CVD growth of monolayer MoS_2 (yellow) with precursors MoO_3 and sulfur onto the 200 nm thick SiO_2 surface layer (blue) of a Si substrate (dark gray), (2) spin-coating of 380 nm thick ZEP e-beam resist, (3) e-beam exposure, development and hardbake of the resist to produce an etch mask of the desired PCC structure, (4) ICP-RIE dry etching to transfer the resist pattern into the MoS_2 and SiO_2 layers, (5) removal of the underlying Si with vapor phase XeF_2 to obtain a free-standing PCC. **b** | Optical microscope image of a typical sample after the ICP-RIE etch (step 4). **c** | SEM image of a PCC with a period of 300 nm. **d** | Magnification of the outer left end and the center of the PCC. **e-g** | Equivalent image sequence to **b-d** showing a sample after the XeF_2 etch. **f** and **g** show a free-standing PCC with a period of 280 nm. The white dashed rectangles in **b-c** and **e-f** indicate the magnified areas shown in the subsequent image.

chemistry with a ratio of 40 sccm : 1 sccm. The complete list of parameters is specified in Appendix A.1. For a closer explanation of the working principle of ICP-RIE, we refer to Section 3.2.3. In order to reach the desired etch depth, the selectivity, i. e. the ratio of resist etch rate r_{ZEP} to substrate etch rate r_{SiO_2} , is crucial to avoid destroying the MoS₂ monolayer. In etching tests, we have measured a maximum selectivity of about $r_{\text{ZEP}} : r_{\text{SiO}_2} = 1.32$. A 200 nm thick SiO₂ membrane, therefore, requires an ZEP resist thickness of at least 264 nm to be completely etched, a 300 nm membrane requires 396 nm thick resist. For that reason, we chose a SiO₂ membrane thickness of 200 nm.

In step 5, we remove the underlying silicon by an isotropic XeF₂ vapor phase etch. The XeF₂ etch chemistry is explained in more detail in Section 3.2.4. This last step is performed without removing the ebeam resist in advance. There are three major reasons that suggest leaving the resist on the PCC structure:

1. Protection and passivation: As indicated in Figure 3.9, XeF₂ attacks MoS₂ to a certain extent which leads to lower PL emission. The resist helps to protect the MoS₂ from XeF₂ and, furthermore, from general environmental influences during measurements.
2. Possible Q -factor improvement: Simulations of PCCs with thicknesses of 200 nm and 300 nm indicate higher Q -factors of the latter (see Figure 4.7 and also [116]). Since ZEP features a refractive index of $n_{\text{ZEP}} = 1.541$ [141] and is, therefore, comparable to SiO₂ ($n_{\text{SiO}_2} = 1.46$), the residual resist helps to effectively increase the thickness of the 200 nm SiO₂ membrane.
3. Improved photonic coupling: With the resist layer on top, the MoS₂ becomes embedded inside the photonic structure. It is, therefore, able to provide better optical coupling since the electric field maxima of the photonic modes are located in the center of the membrane.

Figure 4.2 **b** shows an optical microscope image of a typical sample (in this case, without MoS₂) after step 4. The PCCs are visible as horizontal beams within the quadratic structures, which are arranged in a matrix with a pitch of 100 μm in x direction and of 50 μm in y direction. Columns are separated by vertical lines and each PCC is labelled on its right side. The white dashed rectangle indicates the position of a SEM close-up shown in Figure 4.2 **c**. The displayed PCC has a period of $p = 300$ nm. The SiO₂ layer appears grey, while black areas are ICP-RIE etched. Panel **d** shows a further magnification of the outer mirror section on the left and the perturbation section in the center of the PCC both of which are marked by a white dashed rectangle in panel **c**. For the mirror part, we measure a period of 300.4 nm and, at the center, a period of 269.8 nm. These values match nicely with the nominal mirror period of 300 nm and the expected period in the perturbation center of 0.9×300 nm = 270 nm. We also note that the center part of the PCC is slightly thinner because of proximity effects that emerge much stronger in the middle of a structure than at the edges (c.f. Section 3.2.2).

Figure 4.2 **e-g** show the equivalent sequence of images as **b-d** after fabrication step 5. The sample in **e-g** is the identical one that we use for optical characterization measurements presented in the following section. In Figure 4.2 **e**, the undercut areas around ICP-RIE etched structures are clearly distinguishable from pristine areas due to their brighter greenish color. The SEM image of a PCC with period 280 nm in panel **f** illustrates the rough structured surface of the underlying silicon. Again, we measure the periodicity in the center of the PCC using the close-up image shown in panel **g** and obtain a value of 251.2 nm. The good agreement with the nominal value of $0.9 \times 280 \text{ nm} = 252 \text{ nm}$ confirms the successful fabrication process.

4.2. Optical mode characterization

For the optical characterization of the hybrid PCC devices, we employ a typical micro-photoluminescence (μ -PL) setup, which is sketched and described in detail in Section 3.3.1.

Figure 4.3 **a** shows the emitted spectrum of a PCC with a period of 275 nm recorded at room temperature. The broad MoS₂ PL emission is decorated with four clearly distinguishable modes, M^(*) (purple), M1 (red), M2 (green), and M3 (blue). The solid lines of respective mode color are Lorentzian fits. From the fits' FWHM, we determine Q -factors of 922, 1018, 1706 and 1575. Figure 4.3 **b** to **d** show the modes in magnification with the same color code. Modes M1, M2, and M3 can be identified with the simulation results in Figure 3.3. In addition to the three major modes, we also observe the very weak mode M^(*) in some PCCs spectra, here emerging at 610 nm, which could not be reconstructed by simulation. This mode could possibly originate from the de facto-multilayer structure (SiO₂-MoS₂-ZEP) that was considered as single membrane in simulations.

Furthermore, we want to study the polarization of a PCC mode. The polarization dependence is measured by putting a half wave plate and a polarization filter in the detection path. Since the reflectivity of the spectrometer grating is polarization dependent, the input polarization needs to be kept in a fixed direction in order to avoid errors introduced by the spectrometer. Hence, we leave the polarization filter fixed while only rotating the preceding half wave plate. An rotation angle α of the half wave plate rotates the polarization by 2α .

Figure 4.4 **a** depicts the detected emission spectra in the wavelength area of mode M2 for polarization angles perpendicular ($\alpha = 90^\circ$) and parallel ($\alpha = 0^\circ$) to the PCC axis. The polarization direction is furthermore sketched as green arrows in the SEM images presented next to each of the spectra. While the M2 peak is most prominent at $\alpha = 90^\circ$, it disappears completely at $\alpha = 0^\circ$ demonstrating a strong mode polarization. In order to better quantify the strength of the polarization, we record a spectrum every ten degrees. Figure 4.4 **b** depicts the background-corrected peak intensity of mode M2 (symbols) as a function of the linear polarization angle in units of the summarized maximum (I_{\max}) and minimum (I_{\min}) measured intensity. It reveals a strong linear polarization perpendicular

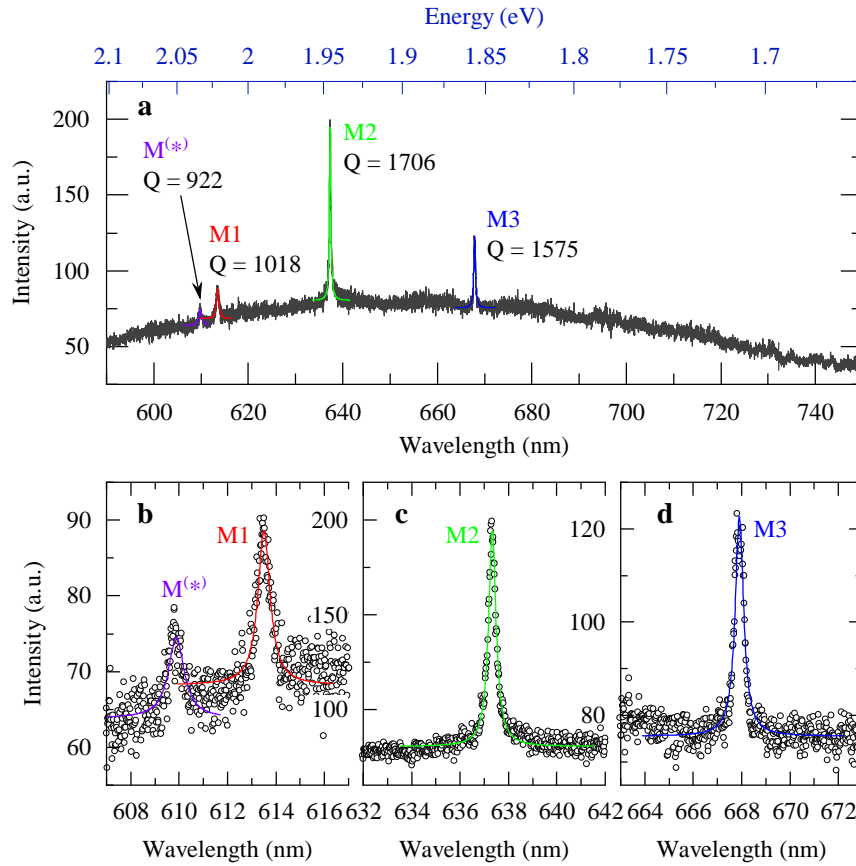


Figure 4.3: **a** | The emission spectrum of a typical hybrid PCC, here shown with a period of 275 nm, depicts the broad PL spectrum decorated with three major modes and a fourth mode $M^{(*)}$ that are fitted with Lorentzians (colored solid lines). Modes M1, M2, and M3 can be identified with the modes that result from simulations in Figure 3.3. The Q -factor of the measured modes are in the range between 900 and over 1700. **b-d** | Magnifications of the single modes using the same color code as in **a**.

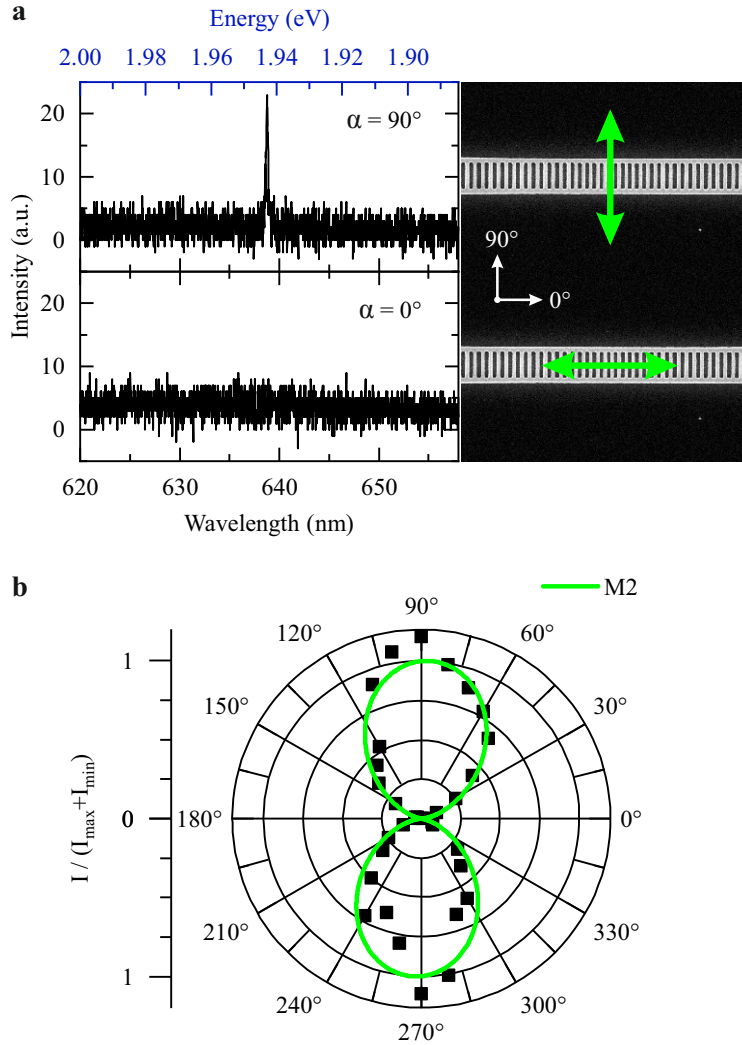


Figure 4.4.: **a** | Emission spectra at polarization angles perpendicular ($\alpha = 90^\circ$) and parallel ($\alpha = 0^\circ$) to the PCC axis. The polarization direction is additionally illustrated as green arrow in the sketches next to each spectrum. **b** | Normalized and background corrected M2 mode peak intensity (symbols) plotted as a function of the linear polarization angle fitted with a \sin^2 function (solid line). The mode appears to be strongly polarized perpendicular to the PCC slab axis with a DoP close to unity. This proves the strong TE-polarization.

to the PCC slab axis expressing a strong transverse-electric (TE) polarization. This agrees with simulations (see Figure 3.3) showing that E_y is the predominant electric field component. The data is fitted with a \sin^2 function (green solid line) with its period parameter kept fixed at 360° . To motivate the fit function, we consider E being the detected electric field amplitude as well as E_0 and I_0 the incident electric field amplitude and intensity, respectively. The detected intensity under the polarization angle α is then

$$I = |E|^2 = |E_0 \sin \alpha|^2 = |E_0|^2 \sin^2 \alpha = I_0 \sin^2 \alpha. \quad (4.1)$$

In order to quantify the polarization quality, we define the degree of polarization

$$\text{DoP} = \frac{I_{\max} - I_{\min}}{I_{\max} + I_{\min}}. \quad (4.2)$$

From evaluation of the fit data, we obtain a value of $\text{DoP} = 1.000 \pm 0.013$ which is close to ideal.

In a further step, we want to confirm the spatial localization and confinement of a PCC mode intensity distribution. Figure 4.5 depicts an optical microscope image of a 310 nm period PCC. The free-standing SiO_2 membrane areas appear greenish, while the non-undercut areas at the borders of the image are brownish. Dark areas completely lack of the SiO_2 membrane. We spatially scanned the laser over this area with a size of $35 \times 35 \mu\text{m}$ using a step size of $1 \mu\text{m}$. At each step, a spectrum was recorded. The accumulated PL intensity at the spectral mode position is plotted for each spatial position in a false-color map in Figure 4.5 **b**. In comparison with **a**, free-standing membrane areas are clearly resolved by their stronger PL emission than pristine areas located at the top, bottom, and left border of the map. This results from the refractive index ratio at the SiO_2/air interface $\frac{n_{\text{SiO}_2}}{n_{\text{air}}} > 1$ which is more reflective than the SiO_2/Si interface $\frac{n_{\text{SiO}_2}}{n_{\text{Si}}} < 1$. Therefore, a larger amount of PL emitted into the substrate gets reflected. The highest PL can be observed at the PCC center, as expected. In order to obtain a map of pure PL enhancement, we need to subtract any intensity variations emerging from the MoS_2 quality. Figure 4.5 **c** exemplarily shows the spectrum recorded at position $(x/y) = (19 \mu\text{m}/19 \mu\text{m})$. For every spectrum, we subtract the blue area (background) from the red area (mode) and plotted the result in a new map in Figure 4.5 **d**. The bright solid lines indicate the outline of the PCC and the ICP-RIE etched areas. This background-corrected map precisely depicts the strong localization of the M1 mode at the center of the PCC.

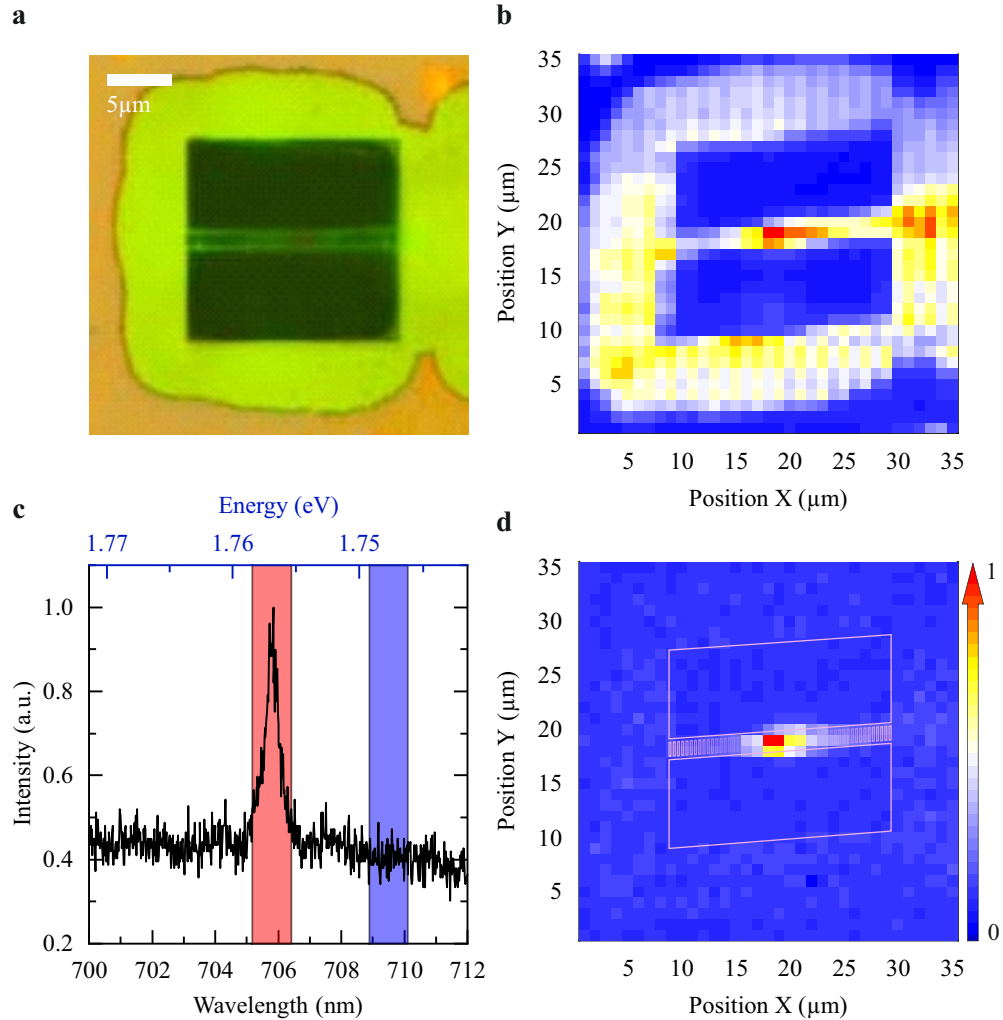


Figure 4.5.: **a** | Microscope image of a PCC with period 310 nm. The greenish area is the free-standing membrane, brownish is pristine SiO₂/Si and the black area ICP-RIE etched. **b** | PL map of the same area shown in **a** with spectral restriction to the M1 mode wavelength (red area in **c**). **c** | Spectrum at the spatial position $(x/y) = (19 \mu\text{m}/19 \mu\text{m})$. The mode area is highlighted in red, the background area used for background correction in blue. **d** | Background corrected PL map. The bright solid lines indicate the outline of the PCC. As expected, the mode is strongly confined in the center of the PCC.

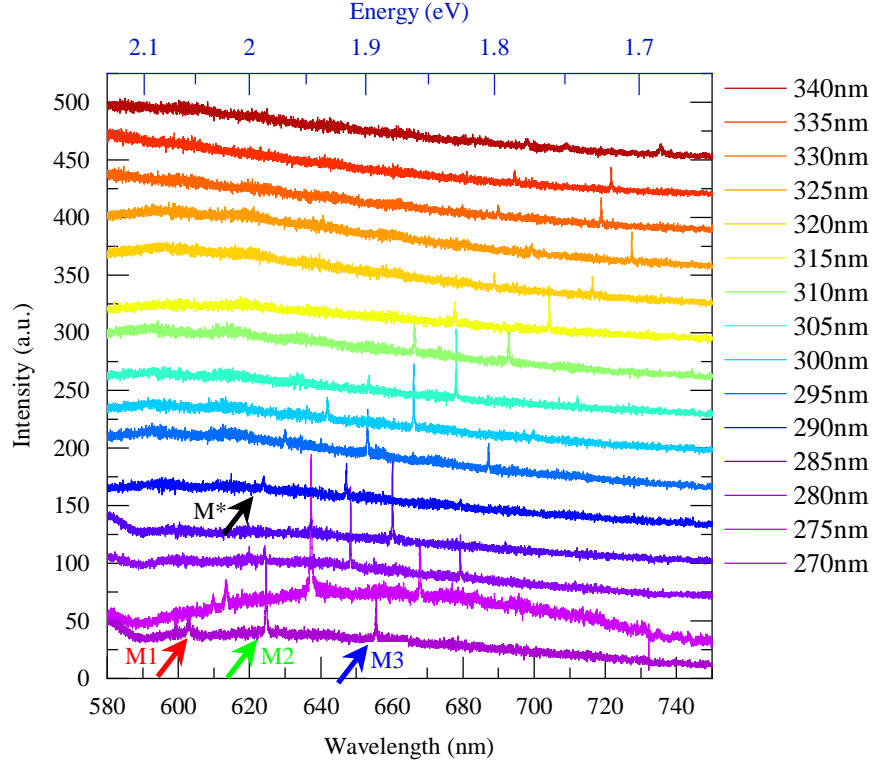


Figure 4.6.: Emission spectra of PCCs with various periodicity ranging from $p = 270$ nm at the bottom to $p = 325$ nm at the top in 5 nm steps. The red (green, blue) arrow marks the M1 (M2, M3) mode. PCCs with $p \geq 290$ nm show an additional mode M^* which is highlighted by the black arrow. All resonance wavelengths increase linearly as a function of the period.

4.3. Geometric mode tuning

Since the PCC resonance wavelengths strongly depend on the period, we can easily tune them by variation of the crystal period. We call this process “geometric tuning”. Figure 4.7 shows the stacked emission spectra of PCCs with periods ranging between 270 nm at the bottom of the graph and 340 nm at the top in 5 nm steps. The resonance wavelengths of mode M1, M2, and M3 (marked by the red, green, and blue arrow) increase linearly as a function of the period. For periods $p \leq 285$ nm, they completely overlap with the MoS_2 PL spectrum while the modes successively disappear for larger periods. For periods $p \geq 290$ nm, we observe an additional mode M^* , which is marked by the black arrow, emerging at shorter wavelengths. The M^* mode also exhibits TE-like character in polarization-dependent measurements. However, its origin is not obvious as we couldn’t reproduce it in simulations. We suppose that it might originate also from the multilayer membrane structure that could cause additional reflections at interior interfaces. In summary, we are able to shift the mode peaks over the entire MoS_2 PL

spectrum simply by increasing the crystal period.

For further analysis of the data in Figure 4.6, we extract the mode positions and Q -factors from Figure 4.6 and plot them as symbols in Figure 4.7 **b** and **c**, respectively. The mode color-code is identical to the one used in Figure 4.6. Cavity modes that are measured on multiple PCCs are represented by the error bars. For reference, we also show a typical PL spectrum of pristine monolayer MoS₂ in panel **a**. All mode positions shift linearly, as also observed by Gong *et al.* [116], within the entire measurement range. The solid lines (using again the symbols' mode color-code) represent simulation results for a SiO₂ membrane thickness of $d = 200$ nm and match well with the measurement data. In order to regard the residual e-beam resist left on top of the PCCs, we additionally show simulation results of mode M1 for membrane thicknesses of $d = 300$ nm. The area of $200 \text{ nm} \leq d \leq 300 \text{ nm}$ is highlighted in faint red. As expected, the M1 measurement results are located within this area.

The Q -factor analysis in panel **c** remarkably reveals values of $Q > 1000$ for almost all PCCs. Our measured Q -factors are systematically lower than the values observed in the work of Gong *et al.* [116] (ranging between 4000 and 5500) which presumably originates from the thinner membrane and also scattering losses that may be caused by the additional interfaces at the MoS₂ and ZEP resist layer. Our data is in very good agreement to the simulation results, especially for modes M1 (again shown for $d = 200$ nm and $200 \text{ nm} < d < 300 \text{ nm}$) and M2, which are located in the same order of magnitude as the measurements.

4.4. Conclusion

In this chapter, we describe the nanofabrication of arrays of optically active SiO₂-MoS₂ PCC resonators onto a SiO₂/Si substrate and discuss the advantages of leaving the e-beam resist on top of the devices. Large scalability of our approach is provided by the CVD growth of monolayer MoS₂, which cannot be achieved by top-down methods like exfoliation. All devices investigated in this chapter stem from a single sample, indicating the high quality of the fabrication process. We observe three major modes in both μ -PL measurements and FDTD simulations. We verify the strong TE nature of the modes, which is predicted by simulation as well, and observe high spatial confinement in the middle of the PCC. Changing the crystal periodicity results in linear spectral mode tuning (so-called geometric tuning) that ranges over the whole MoS₂ PL spectrum, as demonstrated. For periods $p > 285$ nm, we observe an additional mode that shifts linearly with the period as well, but is not reproduced by simulation. Hence, we assume its origin to be in the multilayer membrane structure. The vast majority of all measured modes show Q -factors ranging between $Q = 1000$ and 4000. Both geometric tuning and Q -factor order of magnitude are in very good agreement to our simulations.

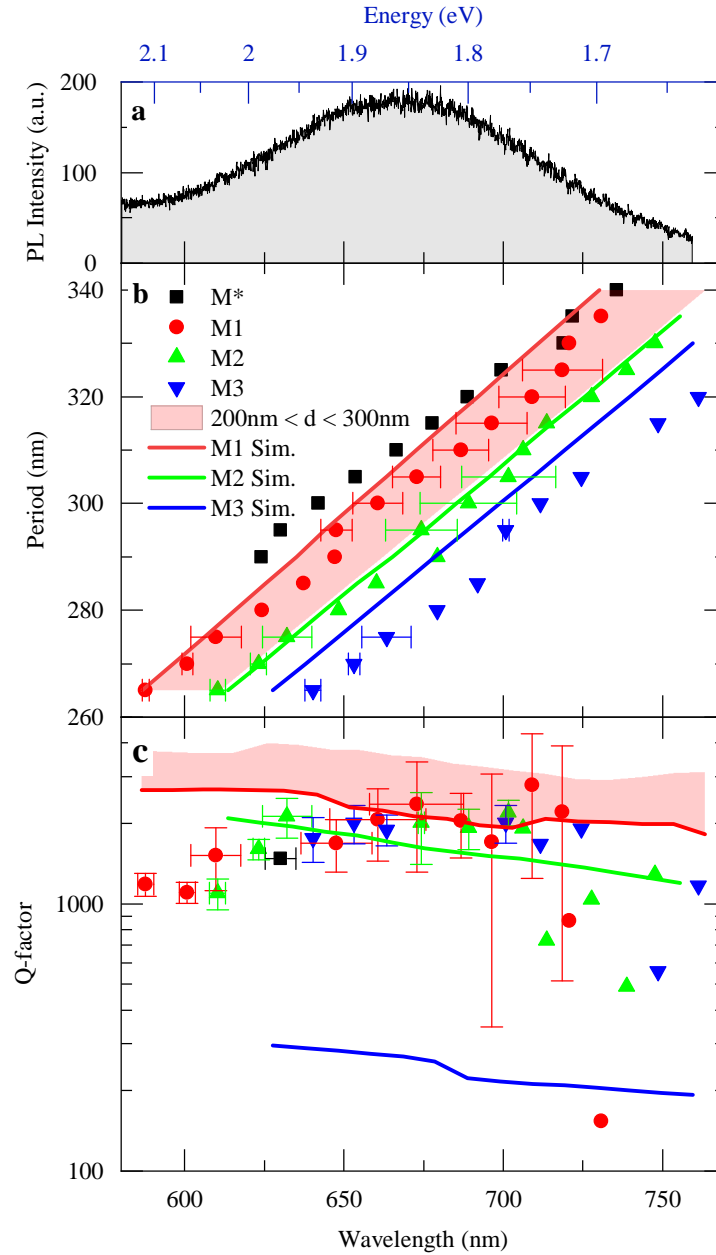


Figure 4.7.: **a** | A typical MoS₂ PL spectrum for reference. **b** | Analysis of the geometric tuning of every mode labeled in Figure 4.6 using the same color-code. The measured mode positions (symbols) increase linearly with the PCC period and match well with the simulation results (solid lines). For consideration of a slightly thicker membrane due to residual e-beam resist, the red shaded area shows the results for membrane thicknesses ranging between $d = 200\text{ nm}$ and 300 nm . **c** | Q -factors observed in experiment and simulation as a function of the respective mode wavelength. The majority of the Q -factors are located in the range of 1000 and 4000 which fits well to the M1 and M2 modes in simulations. The measured data of M3 are significantly higher than observed in simulation.

4.5. Outlook

The PCC design described in this chapter can be natively transferred to other TMDs or TMD based van-der-Waals heterostructures like MoSe₂-WSe₂ heterostructures where highly electrically tunable interlayer excitons with rather long lifetimes of 1.8 ns have been observed [165]. Also, signal enhancement of quantum dot-like single photon sources that have recently been observed in monolayer WSe₂ by multiple groups [5–9] is conceivable.

Since TMDs are, among their other interesting properties, non-linear crystals, the second harmonics emission signal can be effectively enhanced by a PCC supporting half the wavelength of the excitation laser. This effect has been shown by Fryett *et al.* for silicon cavities and exfoliated WSe₂ [31]. In contrast to silicon, though, SiO₂ would drastically reduce absorption losses of the visible and infrared PL shown by most TMDs due to its large bandgap of 9.3 eV.

In terms of integration into photonic circuits, our resonator design is especially useful to work as both PCC and waveguide. Hence, this design could simplify and improve optical coupling between PCCs to form photonic molecules, similar to photonic molecules of so-called *L3* cavities that have been shown by Kapfinger *et al.* [166]. Even photonic networks of a larger amount of PCCs coupled to each other are thinkable.

Alternative cavity design In order to further improve the cavity design, we want to discuss a “proof of principle” simulation study of a circular hole layout that has been inspired by Li *et al.* [23]. In [23], Q -factors of 5.2×10^6 has been shown in simulations and even room-temperature lasing have been experimentally achieved for monolayer MoTe₂ on a Si PCC.

Figure 4.8 **a** shows the PCC layout that we studied in FDTD simulations. Similarly to Figure 2.7, the perturbation area in the center (for hole numbers $-7 < N < 7$) consists of a parabolic reduction of period $p = 300$ nm to $0.9p$ and is surrounded by mirrors. The period as a function of the hole number is illustrated in **d**. We set the beam width to $w = 1.6p$ and the hole radius to $r = 0.35p_N$ (p_N is the period at a specific position and indicates that the radius changes in the perturbation area). Panels **b** and **c** show both the electric field magnitude $|E|$ and, in particular, its E_y component for fundamental mode M1. The calculated Q -factor is $Q = 543$ at a wavelength $\lambda = 630$ nm. This is significantly lower as of the previously shown PCCs, but could possibly be improved in further studies by a systematic variation and optimization of the hole radii and, especially, of the perturbation function. From high Q -factor sensitivity on width variations, that we observe from further simulations, we assume that field leaking in y direction is a major constriction of this extremely small design. However, a small width could be possibly advantageous for cavities with crossed beams. This kind of cavities will be described in paragraph “polarization independent cavity”. Figure 4.8 **e** shows a SEM image of a fabricated free-standing PCC with circular holes and period $p = 265$ nm. We,

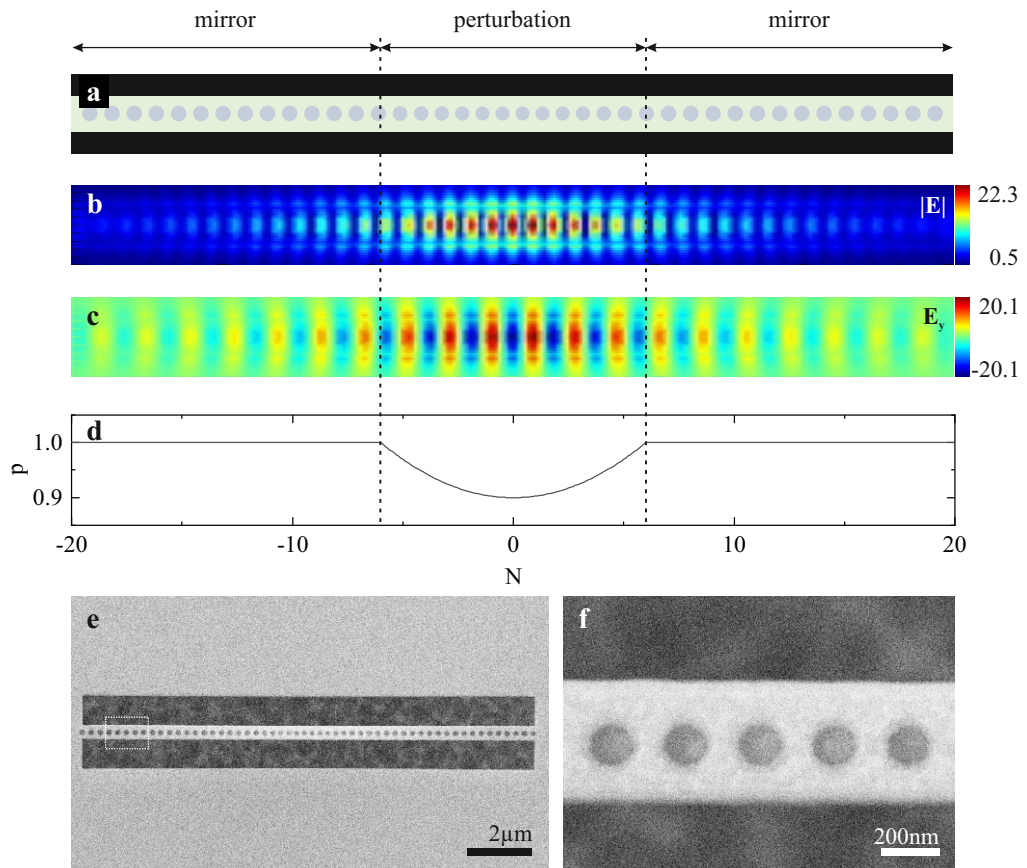


Figure 4.8: **a** | Simulation layout of a circular hole PCC. The perturbation area and mirrors are similar to Figure 2.7, the hole radii are proportionally reduced in the perturbation area. **b** and **c** | Electric field magnitude and E_y component of the fundamental mode (M1). **d** | Period p as a function of hole number N . **e** and **f** | SEM images of a free-standing PCC with circular holes and period $p = 265$ nm. The white dashed rectangle indicates the magnified area shown in **f**.

thereby, demonstrate that fabrication is possible and that the structure is stable. The area indicated by the white dashed rectangle is shown in magnification in panel **f**.

In order to make our simulations' setting comparable with [23], we also considered a Si PCC with the same parameters as [23]. While, in [23], the first mode shows a Q -factor of 5.2×10^6 , we obtain a value of $Q = 1.1 \times 10^5$. The deviation of about 20% is attributed to the different simulation method (transmission simulation) that has been applied in [23].

Polarization independent cavity The choice of SiO_2 as platform material does not only originate from its high establishment in TMD CVD growth and its undeniably easy integration into modern silicon industry fabrication processes, but its optical isotropy and lack of birefringence also makes it a promising candidate for both crystal axis independent and non-polarizing devices. A non-polarizing resonator would be especially favorable for valley-dependent PL enhancement in TMDs. $K+$ and $K-$ valleys are optically addressable by the circular polarization direction which has to be preserved by the cavity. Therefore, a possible cavity design is the superposition of two perpendicularly arranged linearly polarizing resonators as shown in Figure 4.9 **a**. A similar structure consisting of GaAs has been studied by Rivoire [167] using two different wavelengths in the horizontal and vertical arm for non-linear frequency conversion. Based on this concept, non-polarizing SiO_2 cavities as further developments of the “ladder”-type design presented in this work has been investigated in FDTD simulations by Tobias Petzak [168] in the framework of this project.

Figure 4.9 shows simulation results from [168] for three selected extended designs. Panel **a** exhibits a resonator which, in principle, consists of two overlapping 1D PCCs perpendicular to each other that we name “cross-PCC”. The electric field E in x and y direction was found to be of almost equal amplitude and time dependency. The profile of the fundamental mode $|E|$ is depicted in panel **b**. Depending of the hole distance in the center of the structure, Q -factors of up to $Q = 1300$ are obtained. In order to test the stability of such a structure and the parameters of e-beam exposure, we have fabricated the device on pristine SiO_2 without TMD. An SEM image of the free-standing device is depicted in panel **c**.

A possible improvement of the structure in terms of the Q -factor is investigated by adding two more 1D photonic crystal beams forming a star-like structure. Panels **d** to **f** show layout, simulated electric field magnitude and fabricated device of such a “star”-cavity correspondingly to panels **a** to **c**. The Q -factor was found to be 1200 which is insignificantly lower than that of “cross”-PCCs.

A further device simulated in [168] is presented in panel **g**. It consists of concentric rings and can be considered as extension of **d**. The radially arranged slabs are added to carry the rings in a free-standing device. Panel **h** shows the simulated fundamental mode of the device which exhibits a Q -factor of 5000. This value is in the same order of magnitude as the Q -factor of 1D PCCs which is remarkable since the mode needs to be

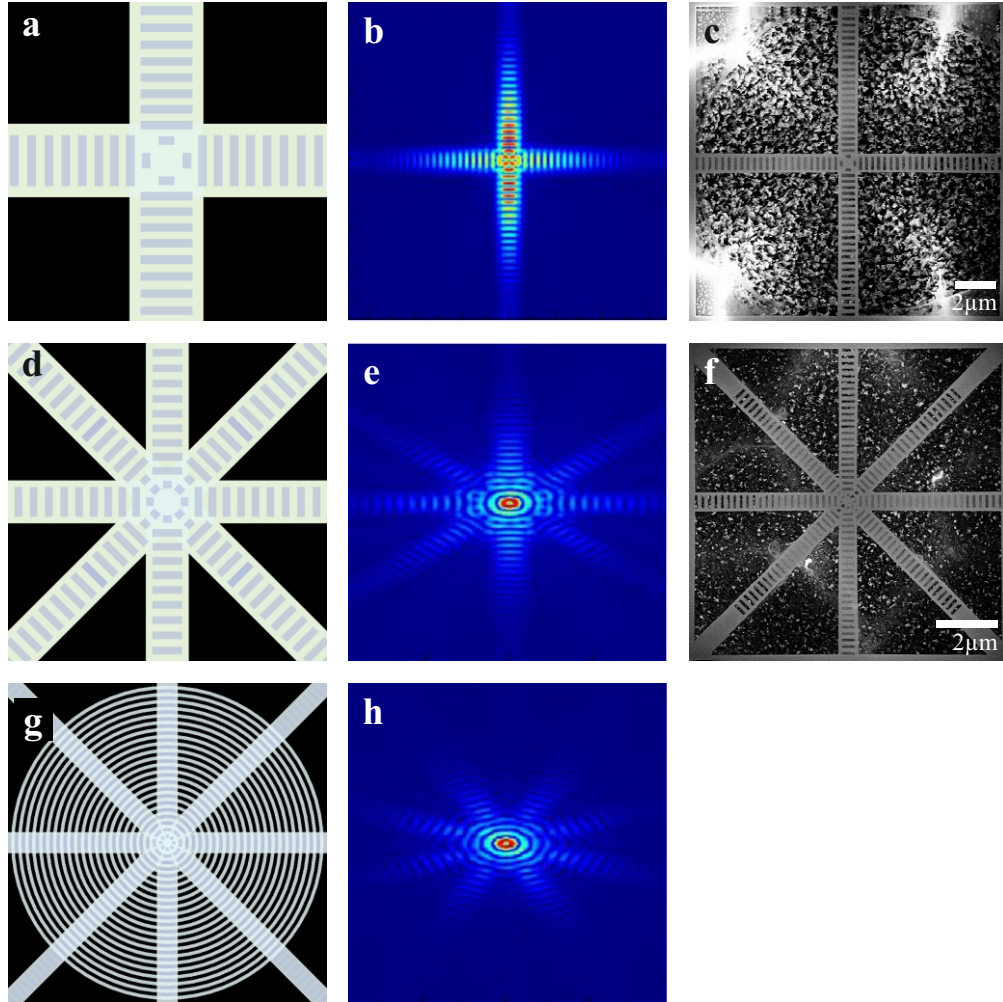


Figure 4.9.: **a** | Cross-PCC layout consisting of two superimposed 1D PCCs perpendicular to each other. **b** | Spatial $|E|^2$ distribution (E being the electric field) of the fundamental mode of **a** which exhibits a Q -factor of $Q = 1300$. **c** | SEM image of a free-standing cross-PCC fabricated on pristine SiO_2 without TMD. **d-f** | Corresponding images to **a-c** for a star-like PCC with two more PCC beams. Simulations exhibit a Q -factor of $Q = 1200$ for the fundamental mode. **g-h** | Layout and simulated electric field distribution for a ring cavity consisting of concentric rings carried by radially arranged beams. For this design, Q -factors of $Q = 5000$ were determined.

confined by photonic crystal mirrors in two dimensions without using the rather efficient total internal reflection.

5 | Tunable Metasurfaces

In Chapter 4, we have considered near-field interaction of 2D materials and photonic crystals. The parameters that have been varied in these systems are purely geometric, which means, we had to define them prior to fabrication. In order to enhance the flexibility of such or similar systems in real-world integrated devices, an additional physical parameter may become desirable that can be varied reproducibly and in real-time. Here, thermochromic materials come into play. These materials have been already studied for decades in their electric and optical behavior (see Section 2.4) and allow us to abruptly change the complex refractive index with temperature by undergoing a metal-insulator transition (MIT) at a specific critical temperature. This can happen on even sub-picosecond time scales [63, 64]. One of the most common representatives of these phase-change materials is vanadium dioxide (VO_2). Current promising developments head for its commercial employment in so-called “smart” coatings, for example, for energy efficient windows [69, 73]. VO_2 nanoclusters (see Section 2.4.1) promise a special benefit since they allow us to shift the critical temperature from 68°C to slightly above room temperature due to their large temperature hysteresis.

In this chapter, we will investigate the impact of refractive index changes on nanophotonic devices that are fabricated from VO_2 nanoclusters and illuminated by both LED light and MoS_2 PL. In contrast to Chapter 4, which focuses on direct light-matter coupling, we will study light diffraction in the near-field diffraction regime. The light field is modulated by Fresnel zone plate (FZP) lenses. FZP lenses are 2D structured patterns and represent the large class of so-called metasurfaces. Their fabrication requires less demanding lithography efforts than that of photonic crystals, which simplifies the rather complex fabrication of monolayer MoS_2 and VO_2 nanoclusters on the same sample. This process will be described in Section 5.1. In Section 5.2, we will illustrate the transmission setup and the measurement procedure. Subsequently, the results are discussed in Section 5.3.

5.1. Fabrication of hybrid devices

The fabrication process of hybrid monolayer MoS_2 - VO_2 nanocluster samples is depicted step by step in Figure 5.1 a. In step 1, we consecutively implant vanadium (V) and oxygen (O) ions in a $500\ \mu\text{m}$ thick fused silica substrate. The ion fluence ratio V : O is 1 : 2 ($9 \times 10^{16}\ \text{cm}^{-2}$: $1.8 \times 10^{17}\ \text{cm}^{-2}$) according to the VO_2 stoichiometry. The fluence magnitude results in average crystal diameters of about $90\ \text{nm}$ [67, 130]. The ion

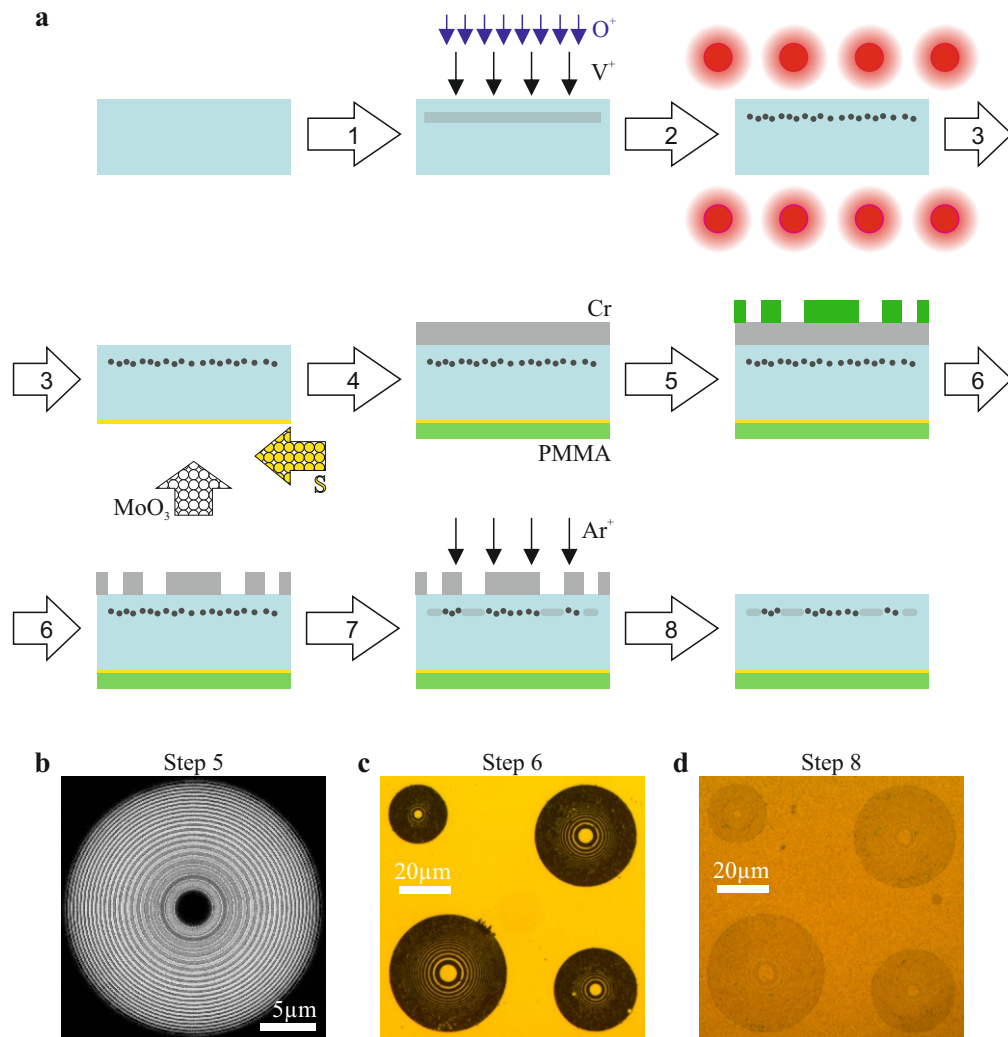


Figure 5.1.: **a** | Sample fabrication process for selectively deactivated FZP lenses. V and O ions are successively implanted into a $500 \mu m$ thick fused silica substrate (step 1) and annealed for 10 min by RTA (step 2). Afterwards, monolayer MoS_2 is grown onto the opposite side via CVD (step 3). While the MoS_2 is passivated by a PMMA coating, a 120 nm thick Cr layer is evaporated on the implanted side of the sample (step 4). In the next step, ZEP resist is spun onto the Cr layer and structured by conventional e-beam lithography (step 5). The FZP structure is transferred into the Cr layer by wet etching and the resist is removed (step 6). The structured Cr layer serves as hardmask for Ar deactivation (step 7). The Cr mask is removed in a last step. **b** | SEM image of a FZP lens with $f = 5 \mu m$ after development. **c** | Optical microscope image showing the Cr mask of FZP lenses with $f = 5 \mu m, 10 \mu m, 15 \mu m$ and $20 \mu m$. **d** | Microscope image after the final fabrication step.

energies of $V_V = 100$ keV and $V_O = 36$ keV correspond to their masses and provide equal implantation depths of about 85 nm. All implant parameters are adopted from [67]. A detailed description of the ion implantation process is provided in Section 3.2.5.

In order to enforce the formation of monocrystalline nanoclusters out of the homogeneous ion distribution in the substrate and to heal crystal defects caused by the implant process, the sample is annealed in an Ar atmosphere for 10 min at a temperature of 950 °C in step 2. This rapid thermal annealing (RTA) process is performed by high power 60 kW halogen lamps that provide a temperature ramping time of 17 s. The cooling time is set to 1 min.

In step 3, monolayer MoS₂ is deposited onto the opposite side of the substrate. We describe the CVD growth process in detail in Section 3.2.1. The order of the process steps during the whole fabrication is crucial due to the impact of temperature on the sample: MoS₂ CVD growth takes place at 670 °C. Hence, the RTA temperature of 950 °C would destroy the monolayer MoS₂. However, the growth has to be performed before Ar deactivation (see step 7) since high temperatures heal the intentionally introduced Ar defects up and would revert the deactivation process.

In order to preserve the MoS₂ from damage during the following fabrication steps, we passivate the bottom side with a PMMA coating. The FZP lens fabrication starts by deposition of a 120 nm Cr layer onto the top side (step 4) that is used as hard mask for site-selective Ar deactivation.

In step 5, a ZEP resist layer is spin-coated onto the Cr layer and structured by e-beam lithography. The e-beam pattern comprises FZP lenses of nominal focal lengths $f = 5$ μm, 10 μm, 15 μm and 20 μm for both possible (inverse) layouts, which are designed after Equation (2.13). We, furthermore, employ manual proximity correction, as described in Section 3.2.2.

A SEM image of a FZP lens with $f = 5$ μm after development is depicted in Figure 5.1 **b**. In the following step, we employ a wet etching solution¹ to transfer the pattern into the Cr layer and remove the resist with acetone. Panel **c** shows a microscope image of the hardmask for FZP lenses with f ranging from 5 μm to 20 μm. The e-beam layout has been designed with 40 zones for every lens. The outer ring of the lens with $f = 5$ μm, hereby, shows a width of only 146 nm. However, the fabrication process, especially the Cr wet etching step, limits the spatial resolution. We, therefore, inevitably forfeit some of the outer Fresnel zones, which is observable in microscope images.

The hard mask allows selective deactivation of the VO₂ nanoclusters (step 7) by Ar ions using a fluence of 7×10^{15} cm⁻² and an energy of 80 keV. These parameters are adopted from [67]. The Ar ions basically revert the annealing process by introducing defects into the clusters.

¹Chrome Etch 18, micro resist technology GmbH, Köpenicker Str. 325, 12555 Berlin

In the last step, we remove the hardmask by the same Cr etching solution that has been applied in step 6. Panel **d** shows a microscope image of the resulting sample surface at the same position as in **c**. Due to rather similar refractive indices of active and deactivated areas, the contrast between single Fresnel zones is very low. All fabrication parameters are summarized in Appendix A.2.

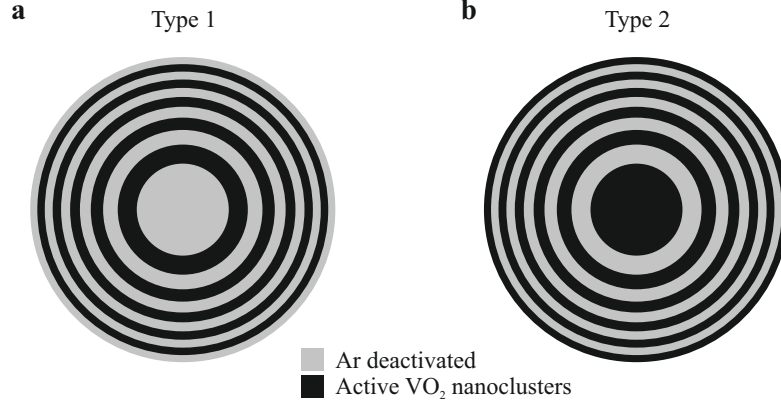


Figure 5.2.: **a** | Selectively deactivated FZP lenses of type 1 have deactivated central disks.
b | Type 2 FZP lenses show the inverse layout of **a**.

Figure 5.2 shows the two possible layouts of a selectively deactivated (SD) FZP lens. We will call the layout in **a** “type 1” in the following. A type 1 FZP lens consists of a deactivated central disk, while the outer Fresnel zones successively alternate between active nanocluster (black) and deactivated (gray) areas. A type 2 lens is depicted in panel **b** and shows the inverse layout of type 1. We have fabricated both types of lenses, but we will predominantly consider and compare type 1 FZP lenses in the main part of this thesis. Type 2 lens measurements are depicted in Appendix A.3 and will be referred to, when necessary.

A different way to site-selectively arrange VO_2 nanocrystals is the so-called “direct synthesis” (see also Section 3.2.5). Directly synthesized (DS) samples are covered by a Cr hardmask before V and O implantation. A third implantation step is omitted. Both methods have been employed by J. Zimmer [67] to fabricate diffraction gratings. A comparison between them show much stronger switching contrasts for the selective deactivation method. This effect predominantly results from the small refractive index contrast in the low-T phase. Due to precedent homogeneous implantation of VO_2 in the selective deactivation method, the low-T phase index contrast is only based on the additionally introduced Ar ions, which is rather low. Therefore, the refractive index change due to the MIT has much more impact on the resulting index contrast. Although DS FZP lenses have been fabricated in the scope of this project, they will not be treated in this thesis. Preliminary and unsystematic measurements (not depicted) have shown that a MIT is not visible in the focusing ability of DS FZP lenses.

5.2. Optical measurements

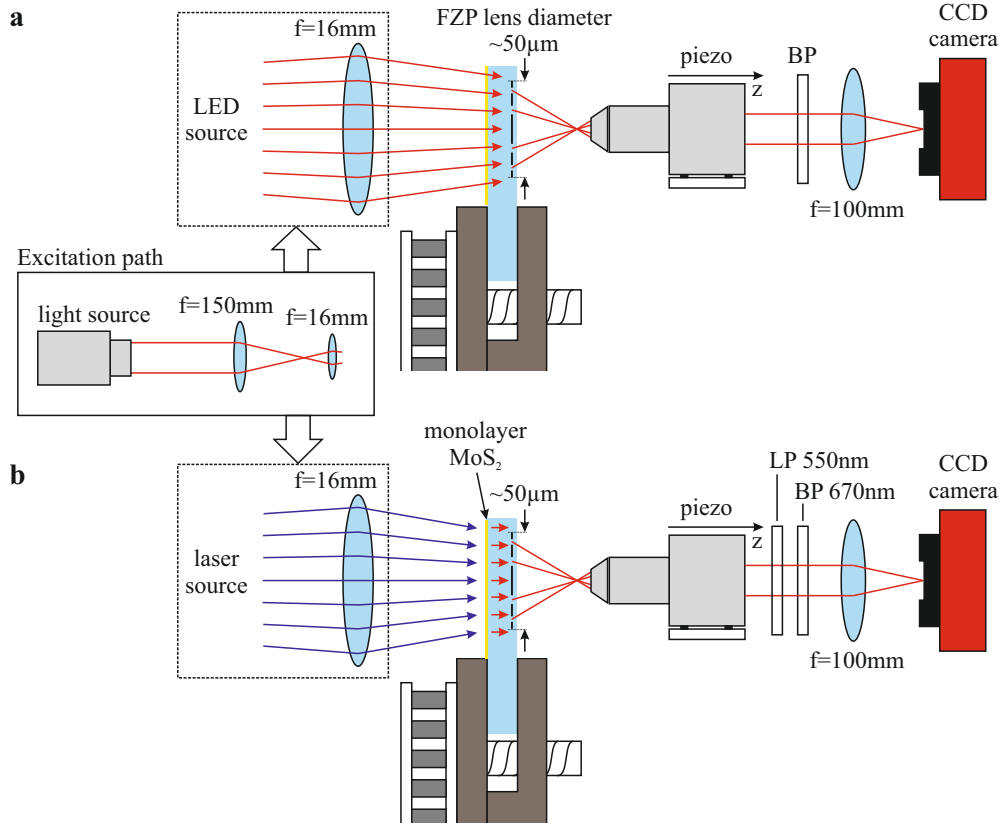


Figure 5.3.: Transmission setup for temperature dependent measurements of the focusing ability of VO_2 implanted FZP lenses. **a** | A LED light source in the red or infrared regime is focused on the sample, in a way that the selected FZP lens is illuminated as homogeneously as possible. The beam path before the sample is illustrated for **a** and **b** in the shared inset. Afterwards, the light is collected by an objective, which is mounted on a piezo actuated stage. The collimated light is filtered by a bandpass filter and focused on a Peltier cooled CCD camera. **b** | The setup for MoS_2 PL illumination only differs from **a** in the excitation path. A $\lambda = 405 \text{ nm}$ laser source is focused on the MoS_2 covered side of the sample, in a way, that the emitted PL illuminates the selected FZP lens. The sketches are not to scale.

Figure 5.3 shows the setup that we use to investigate the temperature dependent focusing properties of a VO_2 implanted FZP lens. The copper sample holder is temperature controlled by a water-cooled Peltier element. As a first step, we use LED light sources of wavelengths $\lambda = 670 \text{ nm}$ and 940 nm to directly illuminate the FZP lens, which is depicted in panel **a**. The sample layout allows to illuminate and observe four lenses with different focal lengths simultaneously. The FZP lens focuses the light at the designated focal distance of a few μm . The focused light is collected by an infinity corrected objective

with $40\times$ magnification and $\text{NA}=0.6$, which is mounted on a piezoelectric stage. The collimated light is subsequently filtered by a bandpass filter (the transmission wavelength depending on the light source) to spectrally narrow the light source. Since FZP lenses are achromatic, the filtering yields a better distinctness of the FZP focus points. Finally, the light is focused onto the CCD chip of a Peltier cooled camera².

In a second step, we change the setup to an “on-chip” light source. Panel **b** shows the focusing of PL which is emitted from monolayer MoS_2 that covers the opposite side of the (transparent) substrate. For excitation, we employ a slightly defocused 405 nm diode laser at a power of $400\ \mu\text{W}$. The excitation is identical in **a** and **b**, except of the light source itself. It consists of a $f = 150\ \text{mm}$ collecting lens followed by a $f = 16\ \text{mm}$ collecting lens to narrow the beam diameter. Due to diffraction limits, laser collimation with a beam diameter in the order of the FZP size ($\approx 50\ \mu\text{m}$) is not possible. Instead, the second lens is positioned in a way that the light spot appears slightly larger than the desired FZP lens in the camera. This helps us to achieve the best trade-off between homogeneous illumination and maximum excitation power density. In order to prohibit excitation laser light detection in the camera, we employ an additional longpass filter at $\lambda = 550\ \text{nm}$.

A measurement sequence consists of the scanning of the objective in steps of $\Delta V_{\text{piezo}} = 0.5\ \text{V}$ or $\Delta z = 0.38\ \mu\text{m}$ along the z axis. The maximal range of the piezoelectric stage is $100\ \mu\text{m}$. At every position, we record an image with the CCD camera using exposure times in the range from 0.5 s to 60 s. The whole procedure is conducted for various temperatures.

Figure 5.4 **a** shows a sketch of a FZP lens in side view with a light beam (red shaded area) incident from the left. The first order focus point is formed by the partial rays depicted in red in a distance f on the right side of the FZPs. Equally, the cone of third order interference (dark blue shaded area) and of the corresponding negative orders (green and orange shaded) are sketched. Panels **b** to **d** show the CCD images of a red LED illuminated $f = 10\ \mu\text{m}$ FZP lens recorded at the z position of focus points $m = -1$ (the objective’s focal plane is inside the substrate), $m = 0$ (objective’s focus on the FZP lens) and $m = 1$ (objective’s focus outside the substrate). In both **b** and **d**, the bright FZP focus spot in the middle of the lens area is clearly visible. The green, white and red lines mark the cross sections that are displayed in **e**. Panel **e** shows the cross sections of a complete measurement sequence as a function of the z position. This yields an image that is comparable to the sketch in panel **a**. Both positive and negative order focus points are clearly visible as well as the (dark) spots of destructive interference that precede and follow those spots in z direction. Also, the positive third order focus point is rather distinct. Especially, the left (negative order) part of the image suffers from some artifacts stemming from small spontaneous xy drifts of the sample. A long term linear xy sample drift over the whole measurement could be corrected by a linear backshift

²Atik cameras ATK-314L

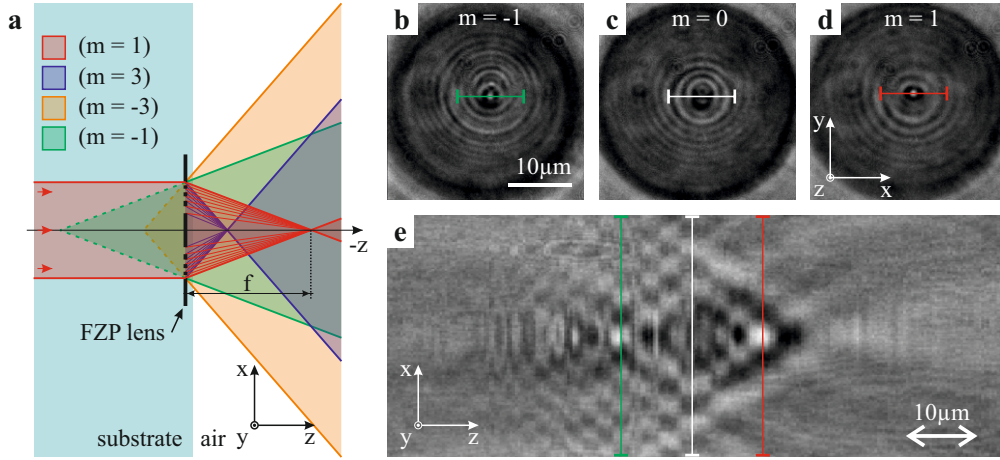


Figure 5.4: **a** | Sketch of the light cones of the four interference orders $m = 1$ (red shaded), $m = 3$ (blue shaded), $m = -3$ (orange shaded), $m = -1$ (green shaded) in side view. **b-d** | CCD images of a FZP lens with $f = 10$ at focus point (z) position of order $m = -1, 0$ and 1 . The colored bar mark the cross sections that are also marked in **e**. **e** | Cross sections of the illuminated FZP lens as a function of the z position. The point of view is identical to the sketch in **a**.

applied to each individual image. Image analysis and corrections are conducted by a custom-built python script.

In the following, we investigate the focus point intensity change as a function of the temperature in a range of 20°C to 95°C . In order to measure the focus point intensity, we define a rectangular area of $7\text{ px} \times 7\text{ px}$ in the center of the FZP lens area and calculate the intensity average for every single image in that area. The pixel resolution is 70 nm px^{-1} . Linear xy shifts of the FZP lens due to a small misalignment of the laser beam or the objective are corrected by linear interpolation of the evaluation area position. Position $z = 0$ is always defined as the position of the FZP lens.

The FZP lens which is exemplarily shown in Figure 5.4 **b-e** is fabricated by the direct-synthesis method. Due to their higher refractive index contrast, DS lenses show more pronounced focus spots. However, a temperature dependent switching has not been measurable. Hence, we only analyze temperature dependent measurements at SD lenses in this work.

5.3. Measurement results

We subdivide our results into three subsections, discriminated by the employed light source. In Section 5.3.1, we will investigate MIT induced effects at a wavelength of

$\lambda = 940$ nm as a first step. Since the VO_2 refractive index change is much more prominent in the infrared regime than in the visible (see Figure 2.12) and since nanoclusters, in particular, show a surface plasmon resonance in the NIR which further enhances the absorption contrast at the MIT, measurements in the NIR regime promise best-observable effects. In Section 5.3.2, we change the LED wavelength to $\lambda = 670$ nm to be in agreement with MoS_2 PL emission, however, without suffering any intensity constrictions. In Section 5.3.3, we will demonstrate measurements on the basis of on-chip monolayer MoS_2 PL.

5.3.1. Infrared LED illumination

Figure 5.5 **a**, **c**, and **e** show the FZP lens focus spot intensity as a function of the z position (the coordinate system is the same as in Figures 5.3 and 5.4) for three different FZP lenses with nominal focal lengths $f_{\lambda=670\text{ nm}} = 10$ μm , 15 μm and 20 μm under the illumination of light with $\lambda = 940$ nm. We record intensity profiles for a set of temperatures following the temperature cycle 20 $^\circ\text{C}$ (bottom profile) \rightarrow 95 $^\circ\text{C}$ \rightarrow 20 $^\circ\text{C}$ (top profile) using incremental steps of 10 $^\circ\text{C}$ at maximum. In each measurement, the objective is moved piezo-electrically controlled along the z axis in a range of about 100 μm with a resolution of 0.38 μm . In these intensity profile plots, the substrate area is highlighted in blue for clarity. For each focal length, we can immediately observe the emergence of distinct maxima and adjacent minima (marked by gray shaded bars) at a temperature of 90 $^\circ\text{C}$ in the heating process (brown line), which disappear again in the cooling process at 30 $^\circ\text{C}$ (green line). Extrema that appear in the “air” half space (positive z values) are real focuses, whereas extrema in the “substrate” half space (negative z values) are virtual. With increasing nominal focal length, these features shift further away from the FZP lens, as expected. The simulations in Figure 3.4 show that the observation of maxima or minima depend on the FZP pattern type. Type 1 and type 2 patterns are defined in Figure 5.2. This can be verified when we compare Figure 5.5 (type 1) with similar measurements on type 2 FZPs in Figure A.2 (Appendix A.3). We find, indeed, that maxima and minima switch positions.

Since the lens design is calculated assuming $\lambda = 670$ nm, the focus intensity maximum does not match the respective nominal values. However, we can recalculate the expected focal lengths for the given design at $\lambda = 940$ nm. From Equation (2.13) for $n = 1$, we obtain the relationship

$$f_\lambda = \frac{r_1^2}{\lambda}. \quad (5.1)$$

The nominal focal distance $f_{670\text{ nm}} = 15$ μm , for example, yields a infrared focal distance of $f_{940\text{ nm}} = 10.7$ μm .

Table 5.1 summarizes $f_{940\text{ nm}}$ of the three investigated FZP lenses. The third column lists the measured z positions of the features with the largest distance from the FZP lens in

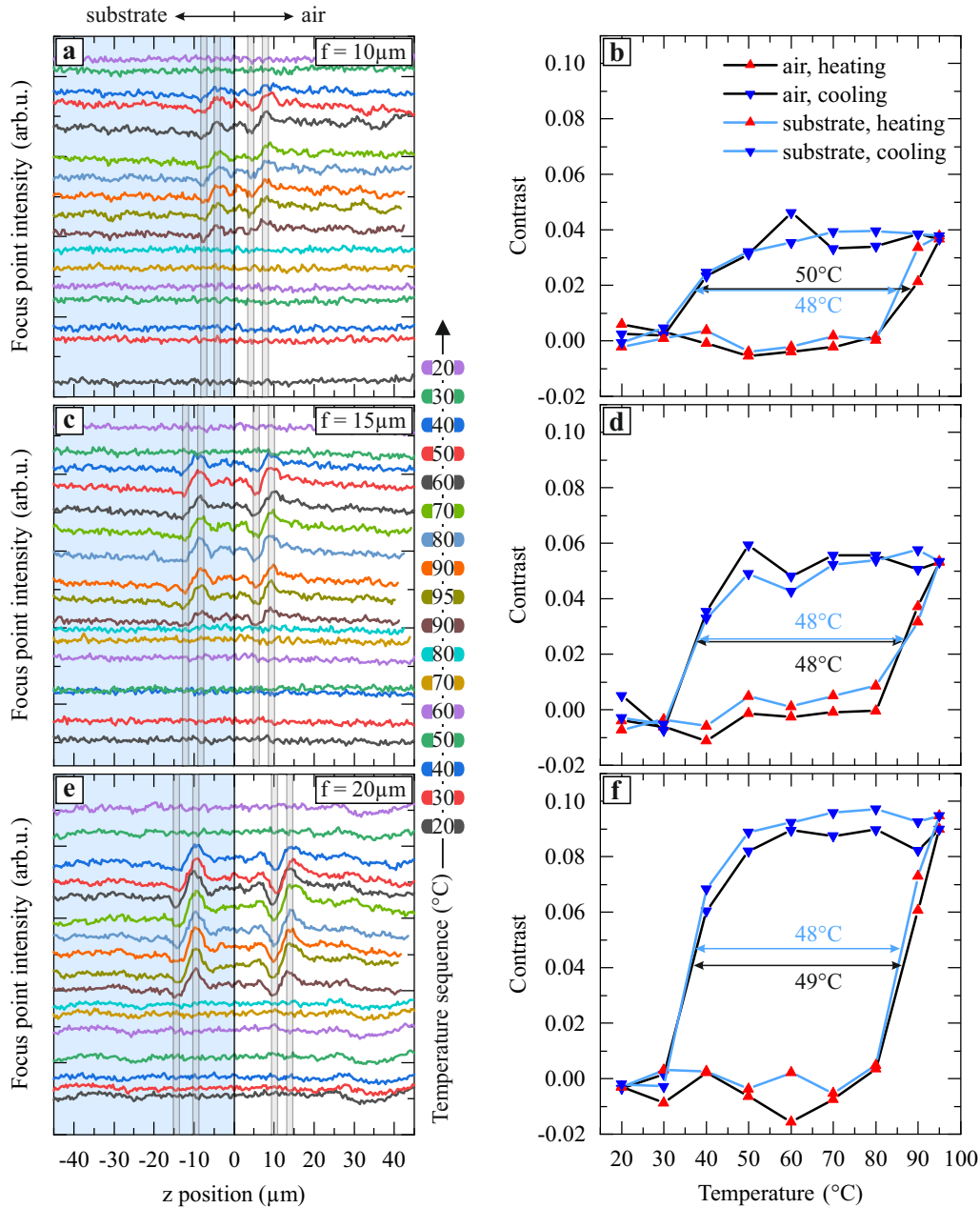


Figure 5.5: **a** | Intensity distribution on the optical axis (z axis) of a FZP lens with focal length $10\ \mu\text{m}$ for infrared illumination ($\lambda = 940\ \text{nm}$). Negative positions (blue background) represent the inside of the sample (substrate) and positive positions the outside (air). The color code represents various sample temperatures applied in the sequence that is depicted in the middle of the figure. Clear intensity maxima I_{max} and minima I_{min} (gray bars) are only visible in the metallic phase of VO_2 . **b** | Intensity contrast as a function of temperature for the “air” side (black line) and the “substrate” side (blue line). The two branches consisting of the heating sequence (red symbols) and the cooling sequence (blue symbols) clearly depict a hysteresis in temperature. **c** and **d** | Intensity profiles and temperature dependent intensity contrasts for a FZP lens with focal length $f = 15\ \mu\text{m}$. **e** and **f** | Equivalent to **c** and **d**, but with $f = 20\ \mu\text{m}$.

Design $f_{\lambda=670\text{ nm}}$ (μm)	Calculation $f_{\lambda=940\text{ nm}}$ (μm)	Measurement $f_{\lambda=940\text{ nm}}$ (μm)
10	7.1	7.9
15	10.7	9.3
20	14.3	13.9

Table 5.1.: Columns 1 and 2 depict corresponding FZP lens focal lengths for wavelengths $\lambda = 670\text{ nm}$ and $\lambda = 940\text{ nm}$. Measurement values are shown in column 3.

the air regime (i. e. maxima, in this case). This corresponds to the $m = 1$ extremum. The measured values match the calculations quite well. The additional mismatch at $15\ \mu\text{m}$ and $20\ \mu\text{m}$ lenses, which show slightly reduced actual focal distances, can be explained by the design of the FZPs, based on the Fraunhofer approximation, that we discuss in Section 3.1.

In order to quantify the temperature dependent focusing behavior, we evaluate the intensity contrast of constructive (I_{max}) and destructive (I_{min}) interference for each temperature. The intensity values are obtained by integrating the intensity within the gray highlighted bars in panels **a**, **c**, and **e**. We define the contrast as

$$\text{Contrast} = \frac{I_{\text{max}} - I_{\text{min}}}{I_{\text{max}} + I_{\text{min}}}. \quad (5.2)$$

Figures 5.5 **b**, **d**, and **f** show the intensity contrast for both air half space (black line) and substrate half space (blue line) of the corresponding FZP lens as a function of temperature. For all FZP lenses, we observe a clear hysteresis. The MIT in the heating branch (red symbols) is at $\sim 80^\circ\text{C}$, in the cooling branch (blue symbols), it is between 30°C and 40°C . Both transition temperatures are in good agreement with direct transmission measurements in Figure 5.3. Real and virtual focus points show nearly identical behavior. The switching contrast increases with the focal length. We assume that this originates from the very high proximity of minima and maxima, which is, especially, valid for larger wavelengths. A reduction of the focal distance, consequently, leads to partial overlapping of minima and maxima resulting in a decrease in their contrast.

5.3.2. Red LED illumination

In Section 5.3.1, we prove that the fabricated FZP lenses are able to both focus NIR light and switch the focusing ability on and off with temperature. In this section, we change the LED wavelength to the area in which monolayer MoS_2 is emitting.

Figure 5.6 shows the identical set of graphs as Figure 5.5, but recorded at wavelength $\lambda = 670\text{ nm}$. Again, we observe features in panels **a**, **c**, and **e**, that emerge in both negative and positive direction in nearly the same distance from the lens. The gray bars mark the

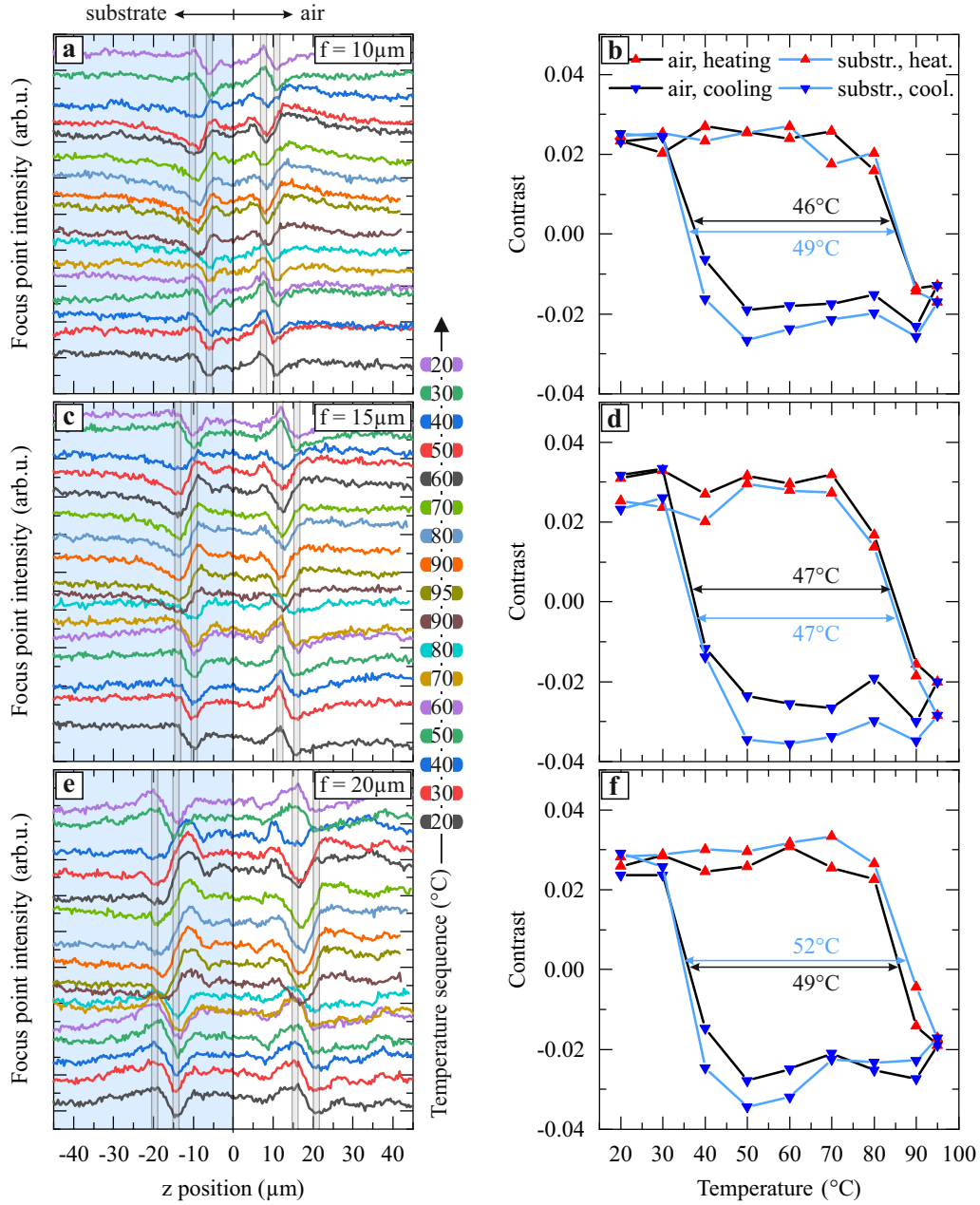


Figure 5.6.: **a** | Intensity distribution on the optical axis (z axis) of a FZP lens with focal length $10\ \mu\text{m}$ for red illumination ($\lambda = 670\ \text{nm}$) at various temperatures. Coordinate system and color codes are identical with Figure 5.5. The clear maxima I_{max} and minima I_{min} (indicated by the gray bars) change significantly in the metallic phase of VO_2 . **b** | Intensity contrast as a function of temperature for the “air” half space (black line) and the “substrate” half space (blue line). The two branches consisting of the heating sequence (red symbols) and the cooling sequence (blue symbols) clearly depict a hysteresis in temperature. **c** and **d** | Intensity profiles and temperature dependent intensity contrasts for a FZP lens with focal length $f = 15\ \mu\text{m}$. **e** and **f** | Equivalent to **c** and **d**, but with $f = 20\ \mu\text{m}$.

positions of minima and maxima that we determined in the bottom profile ($T = 20^\circ\text{C}$) in each panel. As discussed earlier, they represent real and virtual focus points. The feature distance from the lens increases with increasing nominal focal length, as expected and observed in Figure 5.5, as well. In contrast to the former NIR measurements, however, we observe features even at room temperature. This arises from the refractive index difference between active and deactivated zones in the VO_2 low-T phase. This difference has been shown to be significantly smaller at wavelength $\lambda = 940\text{ nm}$, since neither a focusing effect has been measurable at low temperatures nor the FZPs have been even visible in the camera at $z = 0$. The refractive index difference for wavelength $\lambda = 670\text{ nm}$, however, appears to be significant. This leads to the observed focusing even at room temperature. We will further analyze individual profiles at the end of this subsection by comparing them to simulations.

Figures 5.6 **b**, **d**, and **f** show the temperature dependent contrast for each lens, which is defined by Equation (5.2). The positions of I_{\max} and I_{\min} are always determined at room temperature. In a following step, we spatially integrate the intensity at these positions for all profiles and plot the contrast as a function of temperature for both the air and the substrate half space. In all cases, the contrast shows a clear hysteresis which is of similar height for all lenses and ranging between approximately 0.03 and -0.03 . A negative contrast means that $I_{\max} < I_{\min}$, which occurs in the high-T phase due to the refractive index change at the MIT.

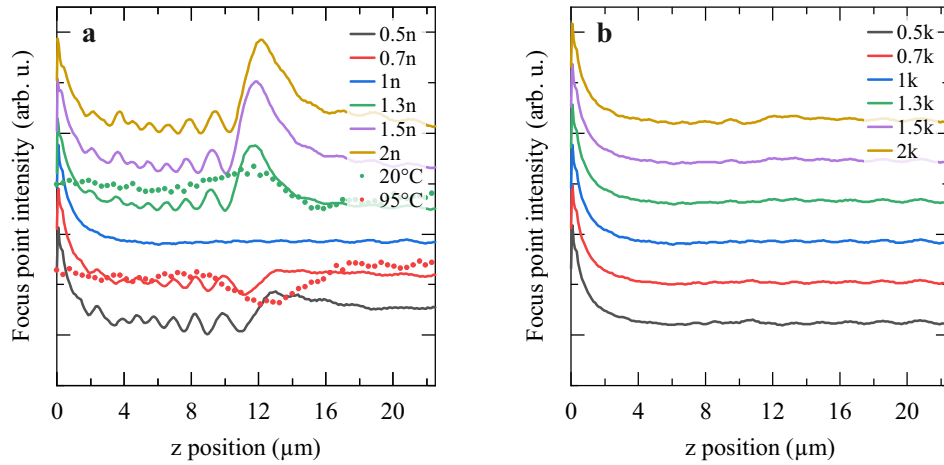


Figure 5.7.: **a** | Simulated intensity on the optical axis of a type 1 FZP lens with $f = 15\ \mu\text{m}$ (solid lines). The complex refractive index $n + ik$ of deactivated zone plates is kept constant. We approximate n and k by measurement values of VO_2 nanoclusters in fused silica (see Figure 3.4). The refractive index of active zone plates n_{active} is varied by different factors of n . Factors $n_{\text{active}}/n < 1$ are analogous to type 1 FZPs in Figure 5.2, whereas factors $n_{\text{active}}/n > 1$ are analogous to type 2. The dots show re-plotted measurement data from Figure 5.6 for temperature $T_{\text{low}} = 20^\circ\text{C}$ and $T_{\text{high}} = 95^\circ\text{C}$. **b** | Simulated intensity on the optical axis for different extinction coefficients k .

Figure 5.7 **a** shows the intensity distribution on the optical axis of a type 1 FZP lens with $f = 15 \mu\text{m}$ obtained by simulation (see also Section 3.1). The profiles have been extracted from a set of 2D simulations, two of which are shown in Figure 3.4. The complex refractive index $n + ik$ of the deactivated Fresnel zones is kept constant since they do not undergo a MIT. We approximate n and k by measurement values of VO_2 nanoclusters in fused silica ($n = 2.625$, $k = 0.144$) as described in Section 3.1. The line colors represent different refractive indices of the active Fresnel zones, which are varied from $n_{\text{active}} = 0.5n$ to $2n$. The falling edge at small z values of every profile arises from evanescent modes of the incident plane wave (incident from the negative half space in positive direction). At a refractive index ratio of 1 (blue line), we do not observe any interference since the FZP lens becomes a homogeneous plane. The profiles with refractive index ratios $\neq 1$ show diffraction patterns of partial waves interfering constructively and destructively. The most prominent features arise at z positions in the area of the nominal FZP focal length. For active Fresnel zones of refractive index $n_{\text{active}} < n$ (black and red line), we primarily observe a distinct intensity minimum at about $z = 11 \mu\text{m}$ followed by a rather weak maximum with a slowly falling edge in positive direction. For active Fresnel zones with refractive index $n_{\text{active}} > n$, we observe prominent maxima between $z = 11 \mu\text{m}$ and $12 \mu\text{m}$ with much steeper falling edges. While all profiles within the former or the latter group are comparable among each other and all features solely become more distinct with higher refractive index differences, the profile shape between those groups is significantly different.

In order to compare simulation and experiment, we re-plot measurement values (dots) at temperature 20°C (green dots) and 95°C (red dots) from Figure 5.6. The scale is adjusted to the simulated profiles $0.7n$ and $1.3n$ which best reproduce the data. We conclude from this comparison of simulation and measurement that the refractive index ratio between active and deactivated zones n_{active}/n switches from > 1 to < 1 at the MIT. Although experimental data shows reasonable good coincidence with the profiles $0.7n$ and $1.3n$ (i. e. deviations from n of $\pm 30\%$), the magnitude of the index change cannot be quantified from this data.

Figure 5.7 **b** shows simulated profiles for a variation of the extinction coefficient k_{active} (the imaginary part of the refractive index of active FZPs), while the real part of the refractive index n is kept constant. We observe no significant change in all six profiles. Hence we conclude that the changes in lens focusing predominantly arise from the changes in the real part of the refractive index. This means that the interference patterns rather arise from phase shifts due to changes in n than from opacity switches due to changes in k .

5.3.3. Molybdenum disulfide photoluminescence illumination

In the following section, we change the light source from off-chip to on-chip by using MoS_2 PL emission. For excitation, we employ a blue diode laser at $\lambda = 405 \text{ nm}$. The setup is sketched and described in detail in Section 5.2.

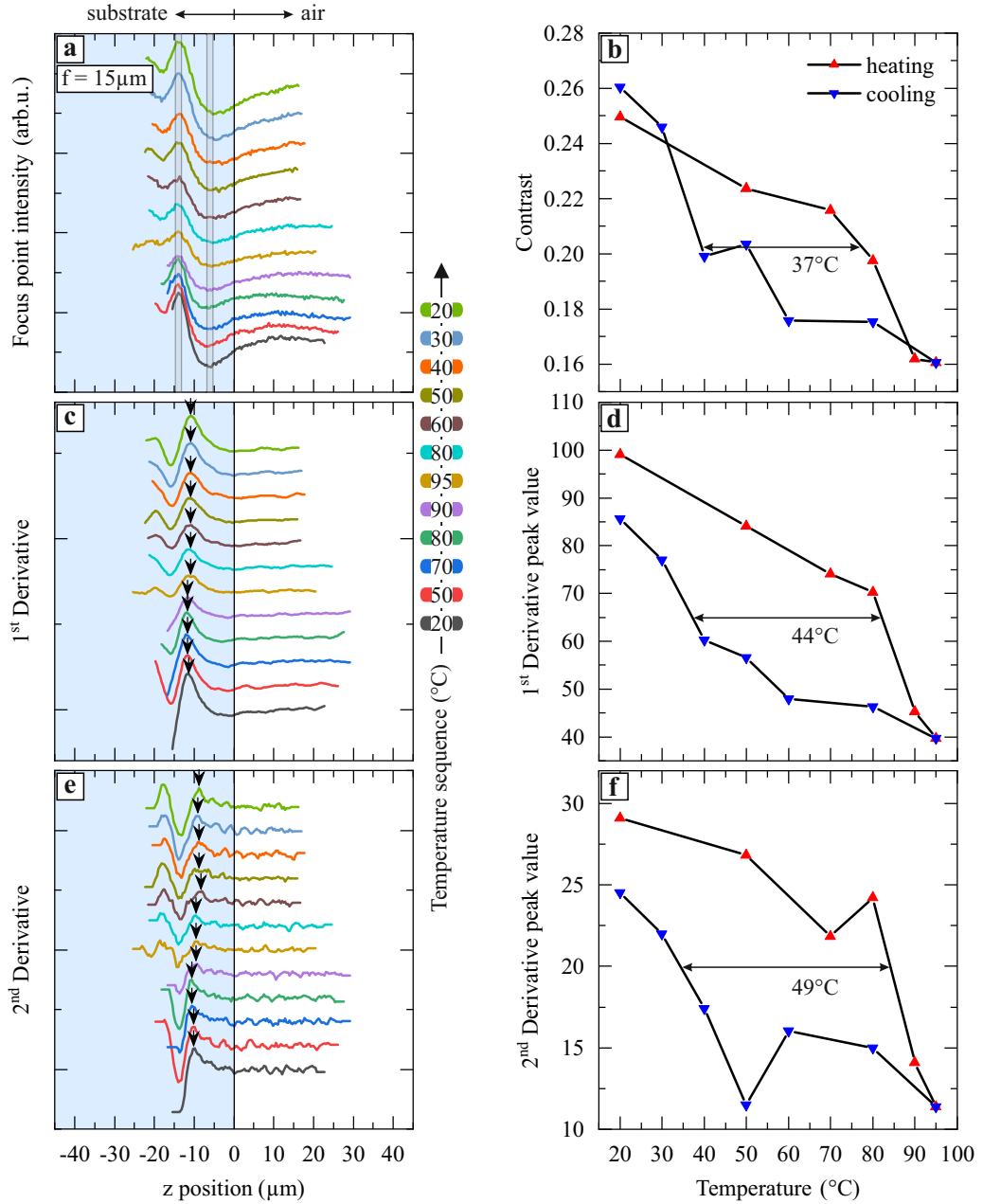


Figure 5.8: **a** | Intensity distribution on the optical axis (z axis) of a FZP lens with focal length $15 \mu\text{m}$ for MoS_2 PL illumination at various temperatures. Coordinate system and color codes are identical with Figure 5.6. The clear maxima I_{max} and minima I_{min} are indicated by the gray bars. **b** | Intensity contrast calculated from I_{max} and I_{min} as a function of temperature. The two branches consisting of the heating sequence (red symbols) and the cooling sequence (blue symbols) depict a hysteresis in temperature which seems to be superimposed by a linear trend with negative slope. **c** | First derivative (i.e. the slope) of the profiles in **a**. The black arrows indicate the maximum in each profile. **d** | Maximum values of the profiles in **c** as a function of temperature. **e** and **f** | Corresponding to **c** and **d** for the second derivative (i.e. the curvature) of the profiles in **a**.

Figure 5.8 **a** shows measured intensity profiles on the optical axis of a $f = 15 \mu\text{m}$ FZP lens under MoS₂ PL illumination. Due to the low intensity of monolayer MoS₂, compared to a LED, we need to use rather long exposure times of 1 min per image. For that reason, we have investigated only one FZP lens. Again, we observe a focusing effect that results in maxima at $z \approx -14 \mu\text{m}$ and broad minima at $z \approx -6 \mu\text{m}$. Both positions are marked by gray bars. In contrast to LED illumination, however, the profiles are asymmetric and features, surprisingly, only occur in one (the substrate) half space. Furthermore, the distance between minima and maxima of $8 \mu\text{m}$ is higher than in Figure 5.6 **c** ($\approx 4 \mu\text{m}$) and we don't observe an exchange of minima and maxima in the high-T phase. These effects have to arise from the change in the experimental conditions, which is, in essence, the on-chip light source. We will later discuss possible reasons for the differences of the intensity profiles measured off-chip and on-chip concerning the mid- to far-field emission characteristics of monolayer MoS₂. For now, we will proceed with the investigation of the temperature dependent behavior, which we analyze similarly to the previous measurements under LED illumination.

The contrast of I_{\min} and I_{\max} , indicated by the gray bars, is plotted as a function of temperature in panel **b**. The contrast changes as a function of temperature of 0.1 (from 0.16 to 0.26) are surprisingly high. However, we only observe a weak hysteresis. The contrast rather seems to imply a strong superimposed linear component decreasing with temperature. For further analysis of the intensity profiles, we additionally show the first and second derivatives in panels **c** and **e** yielding the profile slopes and curvatures. In order to eliminate noise, both first and second derivatives are smoothed by a Savitzky-Golay filter, a method that uses a second order polynomial in a 10 data point window (corresponding to about $3.5 \mu\text{m}$) as regression function. We plot the maxima, marked by the black arrows, as a function of temperature in panels **d** and **f**, respectively. Both slopes and curvatures show a hysteresis in temperature, although it stays less pronounced as in Figures 5.5 and 5.6. In both cases, we still observe the negative linear trend.

This trend could arise by any kind of temperature dependent light attenuation within the beam path if we assume that the incident light intensity has a larger effect on the profile maxima (constructive interference) than on the minima (destructive interference). For that reason, we investigate the temperature dependence of the MoS₂ PL intensity. Figure 5.9 **a** shows the PL intensity as a function of temperature, that is measured in a reflective spectroscopy setup. For intensity determination, we integrate the emission spectrum and normalize the integrated counts, on the one hand, by the laser power, in order to avoid errors by laser intensity fluctuation, and, on the other hand, by the average intensity. For compensation of the temperature dependent expansion of sample and sample holder, the microscope objective is manually re-adjusted at every temperature on the basis of the focus spot size in the camera. We observe a rather constant intensity behavior within a range of $\pm 13\%$ from the average value and conclude that the negative trend in the hysteresis curve in Figure 5.8 does not directly arise from PL intensity decrease. The inset depicts two exemplary spectra at 20°C and at 95°C . While the peak height does not change, the high-temperature PL spectrum is red-shifted. Fig-

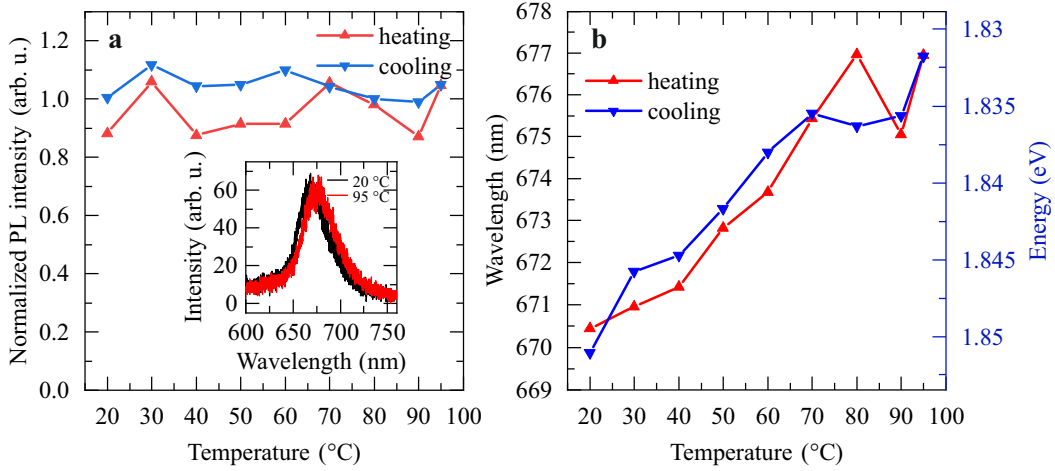


Figure 5.9.: **a** | MoS₂ PL intensity as a function of the temperature measured in reflection. The inset shows PL spectra at 20 °C and at 95 °C. While the intensity stays constant, the spectrum red-shifts by about 6 nm. **b** | MoS₂ PL peak wavelength as a function of the temperature.

Figure 5.9 **b** shows the peak wavelength as a function of the temperature. As expected from conventional semiconductors [169] and also measured for MoS₂ [100, 170], the band gap energy is reduced at higher temperatures, which causes a shift of the PL emission towards larger wavelengths. We measure a shift of about 7 nm over the whole temperature range. The spectral shift is another temperature dependent effect that does not rely on the VO₂ clusters, but influences the measured light intensity due to the 670 nm band-pass filter in front of the camera. Its spectral transmission band has a FWHM of 10 nm. We calculate the resulting transmission drop on the basis of the spectral measurements in Figure 5.9 to be 4% at maximum. In order to compare this intensity decrease with our measurement results in Figure 5.8 **b**, we determine the slope of the linear decrease by fitting the measurement points ≤ 70 °C in the heating arm of the hysteresis. The fit yields a slope of $-6.9 \times 10^{-4} \text{ } ^\circ\text{C}^{-1}$. Furthermore, we estimate the effect of a 4% intensity drop on the contrast by employing Equation (5.2): On the basis of the profile at 20 °C (in the heating branch), we determine both the contrast of the measured minimum I_{\min} and maximum intensity I_{\max} (which is a measurement point in Figure 5.8 **b**) and, as a second point, we calculate the contrast by replacing I_{\max} with $0.96I_{\max}$, indicating a 4% intensity drop in the maximum. This yields a decrease of $-2.6 \times 10^{-4} \text{ } ^\circ\text{C}^{-1}$. This estimation is in the same order of magnitude as the measured decrease, which indicates the strong contribution of the linewidth shift to this effect.

Far-field emission of 2D materials

In this subsection, we want to discuss possible origins of the differences between the intensity profiles of off-chip and on-chip illumination.

The far-field emission characteristics of monolayer MoS₂ PL has been investigated by Schuller *et al.* [171]. The direction of highest emission intensity is not perpendicular to the monolayer, but contains significant k -vector components parallel to it. Furthermore, Schuller *et al.* conclude from polarization measurements that the predominant amount of MoS₂ PL originates from in-plane oriented dipoles. This is the basis on which we simulate monolayer MoS₂ emission in our substrate.

Figure 5.10 **a** shows the magnitude of the electric field emitted from a layer of 20 dipoles (x and y polarized) that are positioned at $z = -500 \mu\text{m}$ incident on a FZP lens at $z = -100 \text{ nm}$. The dipole emitters are fully coherent since their emission pulses start simultaneously. The SiO₂ substrate is located at $-500 \mu\text{m} \geq z \geq 0 \mu\text{m}$. The full simulation area is shown in panel **c**, in which the area of panel **a** is indicated by the white dashed rectangle. All values are normalized with respect to the excitation amplitude. The FZP lens with a diameter of $20.05 \mu\text{m}$ is not visible, but shows a refractive index contrast between active and deactivated zones of $n_{\text{active}} = 1.3n$ (see also Figure 3.4 **b**). The simulated x range and the excitation area are a few microns larger than the FZP lens diameter. This setting corresponds to the measurement setup since the laser-illuminated MoS₂ area has been adjusted to be slightly larger than the FZP lens in the camera. As expected, we observe that the maximum field magnitude of the wave incident on the FZP lens is not at $x = 0$. It increases with larger distance from the optical axis until it decreases again at a distance of $7.5 \mu\text{m}$. This intensity modulation leads to an inhomogeneous illumination and, therefore, an unequal contribution of different zone plates to the focusing. In general, the focusing efficiency is decreased.

For comparison, Figure 5.10 **b** shows the electric field magnitude of an incident plane wave excited at position $z = -20 \mu\text{m}$. In order to adapt the color scale to panel **a**, we equate the maximum values of the incident wave along the x axis slightly beneath the FZP lens in both panels. We observe that the FZP lens is illuminated much more homogeneously and, also, that diffracted light from the FZP lens edges is much more dominant.

Figure 5.10 **d** shows the electric field magnitude profile along the optical axis ($x = 0$) of a FZP lens for the illumination by both coherent dipole emission (solid lines) and a plane wave (dashed lines). In order to consider a lower dependence between single dipoles across the excitation area, we additionally show profiles of incoherent dipole illumination (dashed-dotted lines). The reduction in so-called ‘‘transverse coherence’’ has been achieved by gradually enhancing the time offset of the emission pulses from the center to the outer edges of the excitation area by $\sim 1.1 \text{ fs}$, which corresponds to the travel time of approximately half a wavelength. The FZP lenses have the same contrast settings as in Figure 3.4 featuring $n_{\text{active}} = 0.7n$ (black lines) and $n_{\text{active}} = 1.3n$ (red

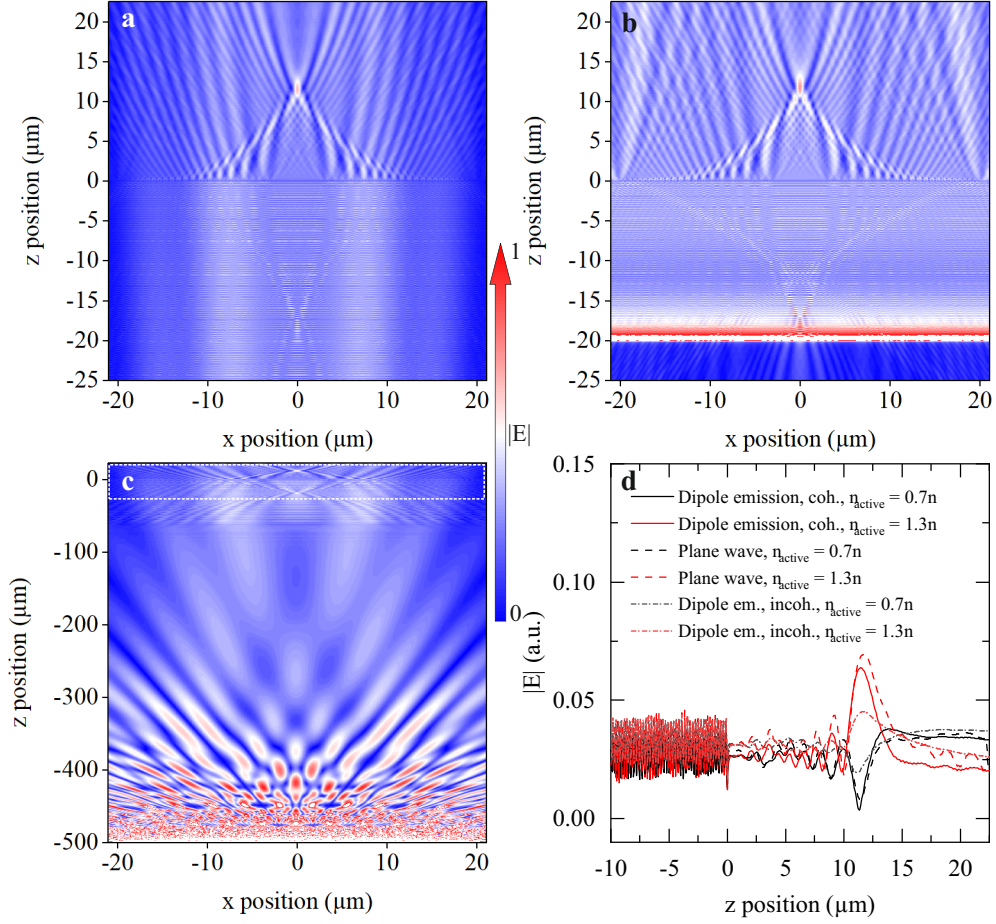


Figure 5.10.: **a** | Electric field magnitude of radiation emitted by coherent in-plane dipoles at $z = -500 \mu\text{m}$ incident on a FZP lens at $z = -100 \text{ nm}$. The refractive index of deactivated FZPs is n and the index of active FZPs is $n_{\text{active}} = 1.3n$. **b** | Electric field magnitude of a plane wave incident on an equal FZP lens as in **a**. The wave excitation takes place at $z = -20 \mu\text{m}$. **c** | Electric field magnitude of radiation emitted by coherent in-plane dipoles at $z = -500 \mu\text{m}$. The area indicated by the white dashed rectangle is magnified in **a**. **d** | Electric field magnitude as a function of z at position $x = 0$ for coherent dipole (solid lines), plane wave (dashed lines), and incoherent dipole illumination as well as the refractive index contrasts $n_{\text{active}} = 0.7n$ (black lines) and $n_{\text{active}} = 1.3n$ (red lines).

lines). Although the general behavior of coherent dipole and plane wave illumination is similar, we observe slight deviations like a shift of the solid curves towards smaller z values. A reduced coherence leads to significantly reduced extrema. For $n_{\text{active}} = 0.7n$, we observe, in all three cases, an inverting of the profile with respect to $n_{\text{active}} = 1.3n$. This stands in contrast to the MoS₂ PL measurements below and above the VO₂ MIT that show no inversion, but only a contrast reduction.

In conclusion, we contribute most of the observed differences in on-chip (MoS₂ PL emission) and off-chip (LED) illumination experiments - being the profile asymmetry as well as the differences in distance and width of the extrema - to an inhomogeneous excitation of the MoS₂ area beneath the FZP lens. The elliptic shape of the laser spot as well as possible imperfections in the monolayer could contribute to an inhomogeneous, and, especially, non-centrosymmetric illumination of the FZP lens. A certain degree of incoherence of the PL emission additionally reduces the focal spot intensity and broadens the extrema. Furthermore, fabrication imperfections could enhance shifting effects leading to an overlapping (in case of the real focus) or a distancing (in case of the virtual focus) of minima and maxima. Additionally, the low signal-to-noise ratio, that requires long exposure times, plays a major role for the broadening of the profile extrema. Such effects could also prevent a complete inverting of the extrema at the MIT, reducing it to a smaller contrast change. In order to fully explain the asymmetry between virtual and real focus spot, further investigations on a larger number of devices are necessary. Such investigations are needed to determine whether this is a general effect or especially related to this single device only.

5.4. Conclusion

In this chapter, we investigate temperature dependent light focusing of Fresnel zone plate lenses consisting of alternating zones of active and deactivated VO₂ nanoclusters. Bulk or film VO₂ shows a metal-insulator transition at the critical temperature $T_c = 68^\circ\text{C}$, whereas VO₂ nanoclusters show different phase change temperatures depending on the initial phase. This causes a hysteresis in every observable (when measured as a function of temperature) that depends on the material phase. This is, for example, applicable in the case of the refractive index. This hysteresis is reproduced in the focusing abilities of our fabricated FZP lenses. We perform measurements with three different light sources: two LEDs with wavelengths 940 nm and 670 nm and PL emission from monolayer MoS₂ that has been grown onto the opposite side of the transparent substrate.

The refractive index contrast between the VO₂ high-T phase and low-T phase is higher in the infrared than in the visible regime. Being in the high-T phase, we observe, accordingly, distinct interference minima and maxima in the intensity distribution on the optical axis of a FZP lens under infrared illumination. These features appear near the nominal focal lengths on both sides of the FZP lens, representing real and virtual focuses. In the low-T phase, however, there are no observable extrema, which indicates the low

refractive index contrast between active and deactivated VO₂ nanoclusters. This effect changes with LED illumination at 670 nm since adjacent minima and maxima are visible in both the high-T and low-T phase. However, these extrema change positions during the MIT yielding basically an inverse profile. We can reproduce these effects qualitatively in simulations and find that the profile inversion can be attributed to a change in the refractive index ratio of active to deactivated nanoclusters from $n_{\text{active}}/n > 1$ to < 1 . This means, in particular, that active nanoclusters show a larger refractive index than deactivated nanoclusters in the low-T phase and vice versa in the high-T phase. Further simulations show that the observed interference patterns solely arise from the real part of the refractive index, whereas the extinction coefficient does not contribute significantly.

In the last section of this chapter, we show that our FZP lenses are able to focus on-chip generated MoS₂ PL. In contrast to the measurements with LED sources, we only observe intensity maxima and minima of the virtual focus. Furthermore, extrema are slightly more extended and show larger distances between each other unlike our observations under LED illumination. We attribute all these findings to an inhomogeneous illumination originating from the mid- and far-field emission characteristics of monolayer MoS₂, that is enforced by an elliptic shape of the excitation spot as well as fabrication imperfections and a low signal-to-noise ratio. Although we don't observe an inversion of maxima and minima at the MIT, like in off-chip illumination, the contrast still shows a hysteresis as a function of temperature. The hysteresis curve depicts a negative linear trend that seems to superimpose the data. This is also reproduced by plotting maximal slopes and curvatures of the intensity profiles as a function of temperature. This trend can be ascribed to a temperature dependent PL wavelength red-shift, that reduces the measured intensity by shifting out of the transmission band of the employed spectral filter. Furthermore, we exclude temperature dependent PL intensity fluctuations by measurements.

5.5. Outlook

Although we have successfully focused monolayer MoS₂ PL emission and have demonstrated fundamental temperature control, there are approaches that could significantly improve our device.

A major parameter that might be optimized is the PL wavelength. We employ MoS₂ due to its advanced and most established growth techniques that allows for high-quality sample sized layers. However, we expect that wavelengths in the telecom regime would significantly improve the temperature switching since FZP lenses in the low-T phase become completely invisible in this regime. Hence, telluride compounds like MoTe₂ or WTe₂ (see Table 2.1) would be much more favorable.

Alternative wavelength regimes might be also generated by using the non-linearity of TMD crystals. Second order harmonics generation, for example, requires a pump laser of

double the wavelength of the desired output wavelength. In order to achieve the emission wavelength of telluride compounds, a laser wavelength $\lambda > 2 \mu\text{m}$ is necessary.

An extension of Fresnel zone plates are metasurfaces or holographic patterns. Those are able to reproduce 3D images or arbitrary intensity patterns, even on the micrometer scale. In principle, a holography pattern corresponds to the Fourier transform of the desired reproduction image. Vividly, we can fragment an 3D image into single points that are generated by FZP lenses of various position and focal length. An holographic pattern can be assumed as superposition of these single FZP lenses. The combination of flat optics and flat light emitters is especially interesting for thin holographic displays that could be employed in cellphones or other devices in which small thicknesses are crucial. For such or similar future applications, in general, electrical pumping of monolayer TMDs will be substantial.

A dedicated application for implanted VO_2 nanoclusters is a temperature sensor with integrated memory functionality. If a temperature fluctuation occurs that exceeds the MIT, the devices switches to the high-T phase and stays there as long as it is not reset by trespassing the low-temperature MIT. The state of such a sensor could be read out optically or electrically.

6 | Conclusion and Outlook

In this thesis, we have demonstrated the use of CVD-grown monolayer MoS₂ in two different kinds of optical devices, photonic crystal cavities (PCCs) and Fresnel zone plate (FZP) lenses consisting of VO₂ nanoclusters.

When coupled with SiO₂ PCCs, the emission spectrum of monolayer MoS₂ features three to four mode peaks. The modes are strongly transverse-electric polarized, spatially confined within the center of the PCC, and show Q -factors between $Q = 1000$ and 4000 for almost all investigated devices. The modes can be linearly tuned over the whole MoS₂ emission spectrum by changing the crystal periodicity.

In the second experimental part of this thesis, monolayer MoS₂ is employed as on-chip light source to investigate the temperature dependent focusing abilities of FZP lenses that consist of implanted VO₂ nanoclusters. VO₂ nanoclusters characteristically show a refractive index hysteresis as a function of temperature during a heating and cooling cycle. This hysteresis is based on a phase change of the material, a metal-insulator transition (MIT), at specific temperatures. The FZP lenses are fabricated by the deactivation of every second Fresnel zone. We observed clear focusing of the MoS₂ PL emission and, also, a hysteresis in the intensity contrast of bright and dark areas on the optical axis. However, the MIT is not as distinct as in off-chip illumination measurements.

As an outlook of this thesis, we want to draw a line from Chapter 5 to Chapter 4. Using FZP lenses, we have demonstrated that VO₂ nanoclusters allow for temperature dependent control of the optical properties of a whole integrated system. This can be also applicable to PCCs. A decrease of the refractive index would reduce the photonic bandgap (see Section 2.2 and [109]). This could lead to a decreased number of photonic modes that would “fit” into the photonic band gap (cf. Figure 2.6). Simultaneously, an increase of the extinction coefficient would lead to higher absorption and, hence, higher losses in the cavity. In this case, we would expect a broadening of observed mode peaks and a decrease in Q -factor. Thus, far-reaching mode control, e. g. by temperature or laser power, would be possible in combination with a memory effect arising from the nanocluster hysteresis.

The fabrication of a VO₂ implanted PCC would be similar to the fabrication process described in Section 4.1, except that the substrate had to be implanted in advance. Similar PCCs with integrated CdSe nanoclusters have been fabricated by M. Mangold [117].

A | Appendix

A.1. Fabrication parameters

Procedure	Parameters
Cleaning	10 min ultrasonic bath in acetone (no MoS ₂ samples) IPA rinse (no MoS ₂ samples) N ₂ purge
Spin-coating	4+4 drops ZEP (during ramp-up and at full speed) 500 rpm, 5 s, ramp-up time 1 s 2500 rpm, 30 s, ramp-up time 1 s
Prebake on hotplate	3 min at 186 °C
e-beam exposure	30 kV acceleration voltage 7.5 μm aperture diameter Area dose: 100 μAcm ⁻² , area step size: 20 nm Line dose: 100 μAcm ⁻¹ , line step size: 10 nm Dot dose: 0.1 pAs
Development	100 s MIBK:Pentylacetat (50:50) 90 s MIBK (stopping) 30 s IPA (rinsing)
Hardbake on hotplate	4 min at 96 °C 5 min at 116 °C (incl. warm-up time)

Table A.1.: e-beam lithography recipe for ZEP resist

Procedure	Parameters
Chamber conditioning	3× etching process at 20 °C (see below)
Sample insertion	use silicone oil as heat contact
Cooling	Temperature 3 °C Cooling time 15 min Helium backing: pressure 10 Torr, max. fluence 10 sccm
Pressure stability	40 sccm CHF ₃ fluence 1 sccm O ₂ fluence pressure 25 mTorr 1 min
Etching	40 sccm CHF ₃ fluence 1 sccm O ₂ fluence pressure 10 mTorr (low pressure strike 25 mTorr) 103 s
Warm-up	1 min

Table A.2.: ICP-RIE recipe

Parameter	Value
Number of etch cycles	3
Etching time per cycle	40 s
Pressure	2 Torr
N ₂ /XeF ₂ ratio	0 %

Table A.3.: XeF₂ etching parameters. The etching system automatically purges the main chamber (containing the sample) and expansion chamber (for gas pressure control) before every etch procedure.

Procedure	Parameters
O ₂ plasma ashing	500 mTorr O ₂ pressure 180 W 3 min
Cr evaporation	120 nm at 1 Ås ⁻¹ rate
Wet etching	80 s Cr etch 18
Mask removal (after implant)	120 s Cr etch 18 water rinse 60 s water bath

Table A.4.: Cr hard mask fabrication.

Element	Energy	Fluence
Vanadium	100 keV	$9 \times 10^{16} \text{ cm}^{-2}$
Oxygen	36 keV	$1.8 \times 10^{17} \text{ cm}^{-2}$
Argon (only SD)	80 keV	$7 \times 10^{15} \text{ cm}^{-2}$

Table A.5.: VO₂ implant parameters.

Parameter	Value
Ar purge (in advance)	2 min
Ar fluence	3 sccm
Temperature	950 °C
Duration	10 min
Ramp-up	17 s
Ramp-down	1 min

Table A.6.: RTA parameters.

A.2. PCC sample layout

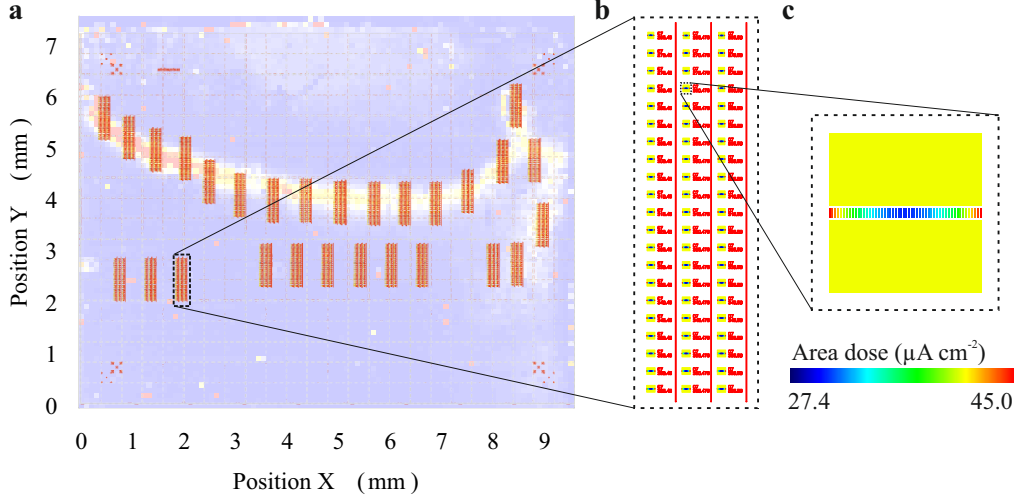


Figure A.1.: **a** | Overlay of a typical MoS₂ PL map and its PCC e-beam pattern. The PCCs are arranged in boxes. **b** | Magnification of a single box containing three columns of 21 PCCs. **c** | A single PCC e-beam pattern. The color code indicates the area dose.

Figure A.1 **a** shows the PL map of a typical MoS₂ sample in overlay with its PCC e-beam pattern (red structures). This particular sample has been employed in all optical measurements in Chapter 4. The PL map is depicted in Figure 3.6 as well. All PCCs are arranged in boxes that have been distributed on the sample to match the areas of highest PL as well as possible. Figure A.1 **b** shows a box in magnification. Each box contains three columns with PCCs of periods in the range $p = 265 \text{ nm}$ to 365 nm . Their nominal width $w = xp$ within each column is slightly different and varies by the factors $x = 4.5, 4.75$ and 5 . Figure A.1 **c** depicts the e-beam pattern of a single PCC. The color code indicates the area dose (see also Figure 3.7).

A.3. Type 2 Fresnel zone plate lenses

Type 2 FZP lenses have an inverse pattern of type 1 lenses. Since we solely show the analysis data of type 1 lenses in the main part, measurement results for type 2 FZP lenses are depicted in Figure A.2 (infrared LED illumination) and Figure A.3 (red LED illumination).

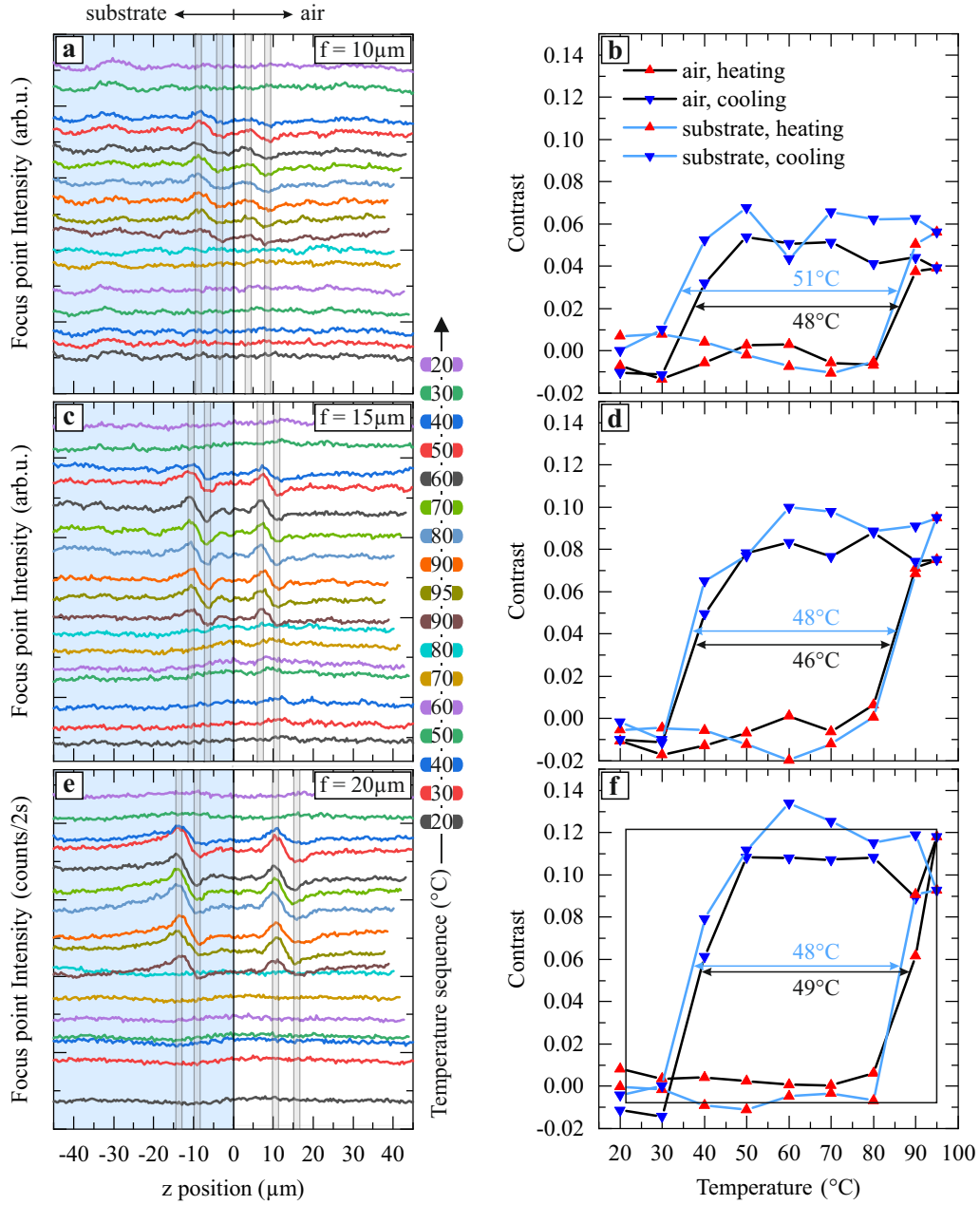


Figure A.2.: **a** | Intensity distribution on the optical axis (z axis) of a type 2 FZP lens with focal length $10\ \mu\text{m}$ for $\lambda = 940\ \text{nm}$ LED illumination at various temperatures. Coordinate system and color codes are identical with Figure 5.5. As observed at type 1 lenses, minima and maxima (indicated by the gray bars) only emerge in the VO_2 high-T phase, however, their positions are exchanged. **b** | Intensity contrast as a function of temperature for the “air” half space (black line) and the “substrate” half space (blue line). The two branches consisting of the heating sequence (red symbols) and the cooling sequence (blue symbols) clearly depict a hysteresis in temperature. **c** and **d** | Intensity profiles and temperature dependent intensity contrasts for a FZP lens with focal length $f = 15\ \mu\text{m}$. **e** and **f** | Equivalent to **c** and **d**, but with $f = 20\ \mu\text{m}$.

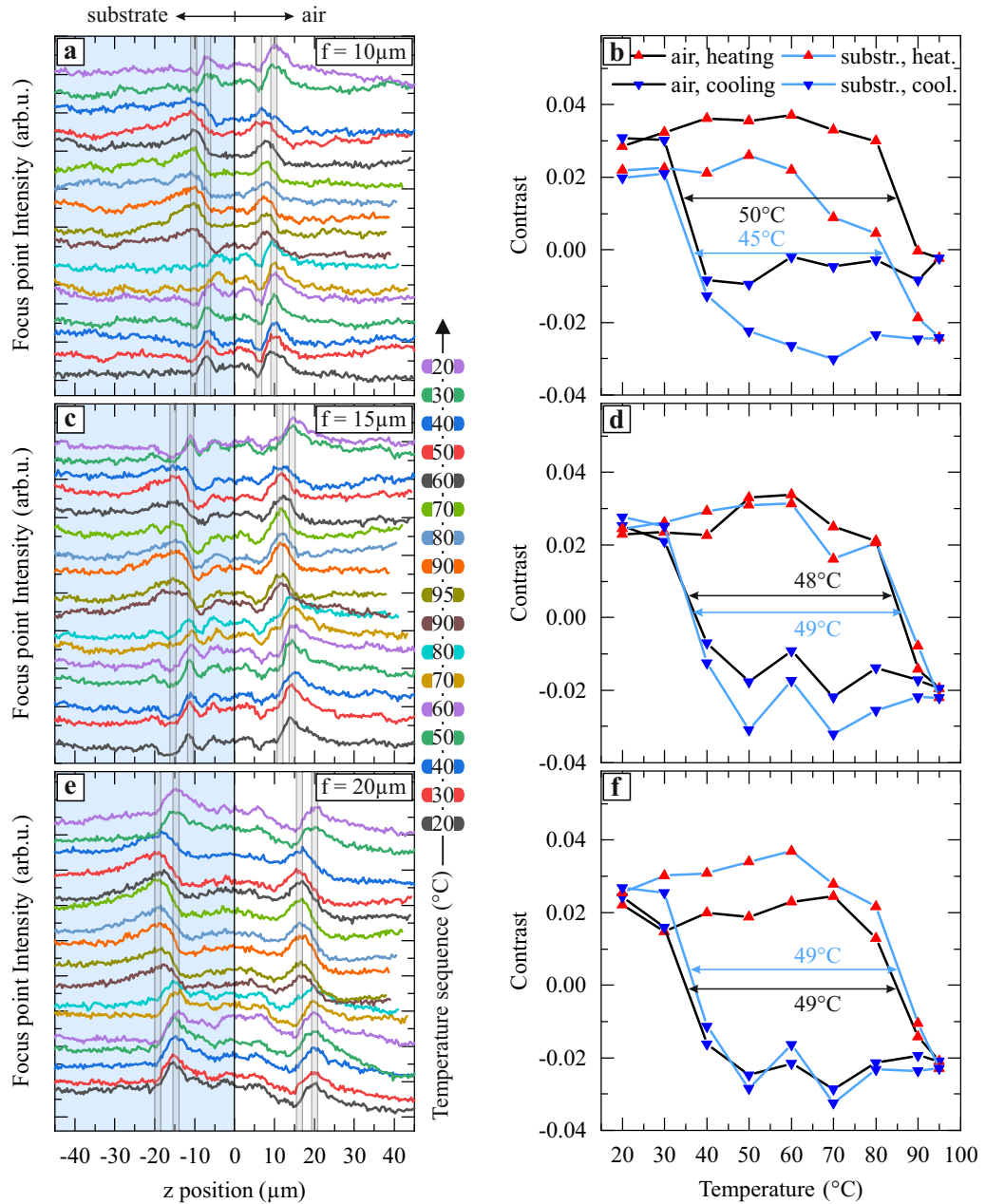


Figure A.3.: **a** | Intensity distribution on the optical axis (z axis) of a type 2 FZP lens with focal length $10\ \mu\text{m}$ for $\lambda = 670\ \text{nm}$ LED illumination at various temperatures. Coordinate system and color codes are identical with Figure 5.5. As observed at type 1 lenses, minima and maxima (indicated by the gray bars) exchange their positions in the VO_2 high-T phase. **b** | Intensity contrast as a function of temperature for the “air” half space (black line) and the “substrate” half space (blue line). The two branches consisting of the heating sequence (red symbols) and the cooling sequence (blue symbols) clearly depict a hysteresis in temperature. **c** and **d** | Intensity profiles and temperature dependent intensity contrasts for a FZP lens with focal length $f = 15\ \mu\text{m}$. **e** and **f** | Equivalent to **c** and **d**, but with $f = 20\ \mu\text{m}$.

Bibliography

1. Avouris, P. & Xia, F. Graphene applications in electronics and photonics. *MRS Bulletin* **37**, 1225–1234. ISSN: 0883-7694. doi:10.1557/mrs.2012.206 (2012).
2. Britnelli, L., Gorbachev, R. V., Jalil, R., Belle, B. D., Schedin, F., Mishchenko, A., Georgiou, T., Katsnelson, M. I., Eaves, L., Morozov, S. V., Peres, N. M. R., Leist, J., Geim, A. K., Novoselov, K. S. & Ponomarenko, L. A. Field-Effect Tunneling Transistor Based on Vertical Graphene Heterostructures. *Science* **335**, 947–950. doi:10.1126/science.1215193 (2012).
3. Bao, W., Cai, X., Kim, D., Sridhara, K. & Fuhrer, M. S. High mobility ambipolar MoS₂ field-effect transistors: Substrate and dielectric effects. *Applied Physics Letters* **102**, 042104. ISSN: 0003-6951. doi:10.1063/1.4789365 (2013).
4. Chen, Y., Wang, X., Wang, P., Huang, H., Wu, G., Tian, B., Hong, Z., Wang, Y., Sun, S., Shen, H., Wang, J., Hu, W., Sun, J., Meng, X. & Chu, J. Optoelectronic Properties of Few-Layer MoS₂ FET Gated by Ferroelectric Relaxor Polymer. *ACS Applied Materials & Interfaces* **8**, 32083–32088. doi:10.1021/acsami.6b10206 (2016).
5. He, Y.-M., Clark, G., Schaibley, J. R., He, Y., Chen, M.-C., Wei, Y.-J., Ding, X., Zhang, Q., Yao, W., Xu, X., Lu, C.-Y. & Pan, J.-W. Single quantum emitters in monolayer semiconductors. *Nature Nanotechnology* **10**, 497–502. doi:10.1038/nnano.2015.75 (2015).
6. Chakraborty, C., Kinnischtzke, L., Goodfellow, K. M., Beams, R. & Vamivakas, A. N. Voltage-controlled quantum light from an atomically thin semiconductor. *Nature Nanotechnology* **10**, 507–511. doi:10.1038/nnano.2015.79 (2015).
7. Koperski, M., Nogajewski, K., Arora, A., Cherkez, V., Mallet, P., Veuillen, J.-Y., Marcus, J., Kossacki, P. & Potemski, M. Single photon emitters in exfoliated WSe₂ structures. *Nature Nanotechnology* **10**, 503–506. doi:10.1038/nnano.2015.67 (2015).
8. Srivastava, A., Sidler, M., Allain, A. V., Lembke, D. S., Kis, A. & Imamoglu, A. Optically active quantum dots in monolayer WSe₂. *Nature Nanotechnology* **10**, 491–496. doi:10.1038/nnano.2015.60 (2015).
9. Tonndorf, P., Schmidt, R., Schneider, R., Kern, J., Buscema, M., Steele, G. A., Castellanos-Gomez, A., van der Zant, H. S. J., Michaelis de Vasconcellos, S. & Bratschitsch, R. Single-photon emission from localized excitons in an atomically thin semiconductor. *Optica* **2**, 347–352. doi:10.1364/OPTICA.2.000347 (2015).

10. Liu, C.-H., Clark, G., Fryett, T., Wu, S., Zheng, J., Hatami, F., Xu, X. & Majumdar, A. Nanocavity Integrated van der Waals Heterostructure Light-Emitting Tunneling Diode. *Nano Letters* **17**, 200–205. doi:10.1021/acs.nanolett.6b03801 (2017).
11. Lopez-Sanchez, O., Lembke, D., Kayci, M., Radenovic, A. & Kis, A. Ultrasensitive photodetectors based on monolayer MoS₂. *Nature Nanotechnology* **8**, 497–501. doi:10.1038/nnano.2013.100 (2013).
12. Tan, H., Xu, W., Sheng, Y., Lau, C. S., Fan, Y., Chen, Q., Tweedie, M., Wang, X., Zhou, Y. & Warner, J. H. Lateral Graphene-Contacted Vertically Stacked WS₂/MoS₂ Hybrid Photodetectors with Large Gain. *Advanced Materials* **29**, 1702917. doi:10.1002/adma.201702917 (2017).
13. Akama, T., Okita, W., Nagai, R., Li, C., Kaneko, T. & Kato, T. Schottky solar cell using few-layered transition metal dichalcogenides toward large-scale fabrication of semitransparent and flexible power generator. *Scientific Reports* **7**, 11967. ISSN: 2045-2322. doi:10.1038/s41598-017-12287-6 (2017).
14. Pospischil, A., Furchi, M. M. & Mueller, T. Solar-energy conversion and light emission in an atomic monolayer p-n diode. *Nature Nanotechnology* **9**, 257–261. doi:10.1038/nnano.2014.14 (2014).
15. Boulesbaa, A., Babicheva, V. E., Wang, K., Kravchenko, I. I., Lin, M.-W., Mahjouri-Samani, M., Jacobs, C. B., Puretzky, A. A., Xiao, K., Ivanov, I., Rouleau, C. M. & Geohegan, D. B. Ultrafast Dynamics of Metal Plasmons Induced by 2D Semiconductor Excitons in Hybrid Nanostructure Arrays. *ACS Photonics* **3**, 2389–2395. ISSN: 2330-4022. doi:10.1021/acsphotonics.6b00618 (2016).
16. Butun, S., Tongay, S. & Aydin, K. Enhanced light emission from large-area monolayer MoS₂ using plasmonic nanodisc arrays. *Nano Letters* **15**, 2700–2704. doi:10.1021/acs.nanolett.5b00407 (2015).
17. Liu, T., Qiu, H., Yin, T., Huang, C., Liang, G., Qiang, B., Shen, Y., Liang, H., Zhang, Y., Wang, H., Shen, Z., Hewak, D. W. & Wang, Q. J. Enhanced light-matter interaction in atomically thin MoS₂ coupled with 1D photonic crystal nanocavity. *Optics Express* **25**, 14691–14696. ISSN: 1094-4087. doi:10.1364/OE.25.014691 (2017).
18. Hammer, S., Mangold, H. M., Nguyen, A. E., Martinez-Ta, D., Naghibi Alvillar, S., Bartels, L. & Krenner, H. J. Scalable and Transfer-Free Fabrication of MoS₂/SiO₂ Hybrid Nanophotonic Cavity Arrays with Quality Factors Exceeding 4000. *Scientific Reports* **7**, 7251. ISSN: 2045-2322. doi:10.1038/s41598-017-07379-2 (2017).
19. Gan, X., Gao, Y., Fai Mak, K., Yao, X., Shiue, R.-J., van der Zande, A., Trusheim, M. E., Hatami, F., Heinz, T. F., Hone, J. & Englund, D. Controlling the spontaneous emission rate of monolayer MoS₂ in a photonic crystal nanocavity. *Applied Physics Letters* **103**, 181119. ISSN: 0003-6951. doi:10.1063/1.4826679 (2013).

-
20. Liu, X., Galfsky, T., Sun, Z., Xia, F., Lin, E.-c., Lee, Y.-H., Kéna-Cohen, S. & Menon, V. M. Strong light–matter coupling in two-dimensional atomic crystals. *Nature Photonics* **9**, 30–34. doi:10.1038/nphoton.2014.304 (2015).
 21. Noori, Y. J., Cao, Y., Roberts, J., Woodhead, C., Bernardo-Gavito, R., Tovee, P. & Young, R. J. Photonic Crystals for Enhanced Light Extraction from 2D Materials. *ACS Photonics* **3**, 2515–2520. ISSN: 2330-4022. doi:10.1021/acsp Photonics.6b00779 (2016).
 22. Schwarz, S., Dufferwiel, S., Walker, P. M., Withers, F., Trichet, A. A. P., Sich, M., Li, F., Chekhovich, E. A., Borisenko, D. N., Kolesnikov, N. N., Novoselov, K. S., Skolnick, M. S., Smith, J. M., Krizhanovskii, D. N. & Tartakovskii, A. I. Two-Dimensional Metal-Chalcogenide Films in Tunable Optical Microcavities. *Nano Letters* **14**, 7003–7008. doi:10.1021/nl503312x (2014).
 23. Li, Y., Zhang, J., Huang, D., Sun, H., Fan, F., Feng, J., Wang, Z. & Ning, C. Z. Room-temperature continuous-wave lasing from monolayer molybdenum ditelluride integrated with a silicon nanobeam cavity. *Nature Nanotechnology* **12**, 987–992. doi:10.1038/nnano.2017.128 (2017).
 24. Salehzadeh, O., Djavid, M., Tran, N. H., Shih, I. & Mi, Z. Optically Pumped Two-Dimensional MoS₂ Lasers Operating at Room-Temperature. *Nano Letters* **15**, 5302–5306. doi:10.1021/acs.nanolett.5b01665 (2015).
 25. Wu, S., Buckley, S., Jones, A. M., Ross, J. S., Ghimire, N. J., Yan, J., Mandrus, D. G., Yao, W., Hatami, F., Vučković, J., Majumdar, A. & Xu, X. Control of two-dimensional excitonic light emission via photonic crystal. *2D Materials* **1**, 011001. doi:10.1088/2053-1583/1/1/011001 (2014).
 26. Wu, S., Buckley, S., Schaibley, J. R., Feng, L., Yan, J., Mandrus, D. G., Hatami, F., Yao, W., Vučković, J., Majumdar, A. & Xu, X. Monolayer semiconductor nanocavity lasers with ultralow thresholds. *Nature* **520**, 69–72. doi:10.1038/nature14290 (2015).
 27. Ye, Y., Wong, Z. J., Lu, X., Ni, X., Zhu, H., Chen, X., Wang, Y. & Zhang, X. Monolayer excitonic laser. *Nature Photonics* **9**, 733–737. doi:10.1038/nphoton.2015.197 (2015).
 28. Malard, L. M., Alencar, T. V., Barboza, A. P. M., Mak, K. F. & de Paula, A. M. Observation of intense second harmonic generation from MoS₂ atomic crystals. *Physical Review B: Condensed Matter* **87**, 201401. ISSN: 0921-4526. doi:10.1103/PhysRevB.87.201401 (2013).
 29. Wang, G., Marie, X., Gerber, I., Amand, T., Lagarde, D., Bouet, L., Vidal, M., Balocchi, A. & Urbaszek, B. Giant Enhancement of the Optical Second-Harmonic Emission of WSe₂ Monolayers by Laser Excitation at Exciton Resonances. *Physical Review Letters* **114**, 097403. doi:10.1103/PhysRevLett.114.097403 (2015).
-

30. Seyler, K. L., Schaibley, J. R., Gong, P., Rivera, P., Jones, A. M., Wu, S., Yan, J., Mandrus, D. G., Yao, W. & Xu, X. Electrical control of second-harmonic generation in a WSe₂ monolayer transistor. *Nature Nanotechnology* **10**, 407–411. doi:10.1038/nnano.2015.73 (2015).
31. Fryett, T. K., Seyler, K. L., Zheng, J., Liu, C.-H., Xu, X. & Majumdar, A. Silicon photonic crystal cavity enhanced second-harmonic generation from monolayer WSe₂. *2D Materials* **4**, 015031. doi:10.1088/2053-1583/4/1/015031 (2017).
32. Salehzadeh, O., Tran, N. H., Liu, X., Shih, I. & Mi, Z. Exciton kinetics, quantum efficiency, and efficiency droop of monolayer MoS₂ light-emitting devices. *Nano Letters* **14**, 4125–4130. doi:10.1021/nl5017283 (2014).
33. Mann, J., Ma, Q., Odenthal, P. M., Isarraraz, M., Le, D., Preciado, E., Barroso, D., Yamaguchi, K., von Son Palacio, G., Nguyen, A., Tran, T., Wurch, M., Nguyen, A., Klee, V., Bobek, S., Sun, D., Heinz, T. F., Rahman, T. S., Kawakami, R. & Bartels, L. 2-Dimensional Transition Metal Dichalcogenides with Tunable Direct Band Gaps: MoS₂(_{1-x})Se_{2x} Monolayers. *Advanced Materials* **26**, 1399–1404. doi:10.1002/adma.201304389 (2014).
34. Xu, X., Yao, W., Di Xiao & Heinz, T. F. Spin and pseudospins in layered transition metal dichalcogenides. *Nature Physics* **10**, 343–350. ISSN: 1745-2473. doi:10.1038/nphys2942 (2014).
35. Jones, A. M., Yu, H., Ghimire, N. J., Wu, S., Aivazian, G., Ross, J. S., Zhao, B., Yan, J., Mandrus, D. G., Di Xiao, Yao, W. & Xu, X. Optical generation of excitonic valley coherence in monolayer WSe₂. *Nature Nanotechnology* **8**, 634–638. doi:10.1038/nnano.2013.151 (2013).
36. Mak, K. F., He, K., Shan, J. & Heinz, T. F. Control of valley polarization in monolayer MoS₂ by optical helicity. *Nature Nanotechnology* **7**, 494–498. doi:10.1038/nnano.2012.96 (2012).
37. Xiao, D., Liu, G.-B., Feng, W., Xu, X. & Yao, W. Coupled spin and valley physics in monolayers of MoS₂ and other group-VI dichalcogenides. *Physical Review Letters* **108**, 196802. doi:10.1103/PhysRevLett.108.196802 (2012).
38. Zeng, H., Dai, J., Yao, W., Xiao, D. & Cui, X. Valley polarization in MoS₂ monolayers by optical pumping. *Nature Nanotechnology* **7**, 490–493. doi:10.1038/nnano.2012.95 (2012).
39. Mak, K. F., Lee, C., Hone, J., Shan, J. & Heinz, T. F. Atomically Thin MoS₂: A New Direct-Gap Semiconductor. *Physical Review Letters* **105**, 136805. doi:10.1103/PhysRevLett.105.136805 (2010).
40. Splendiani, A., Sun, L., Zhang, Y., Li, T., Kim, J., Chim, C.-Y., Galli, G. & Wang, F. Emerging Photoluminescence in Monolayer MoS₂. *Nano Letters* **10**, 1271–1275. doi:10.1021/nl903868w (2010).

-
41. Almeida, K., Wurch, M., Geremew, A., Yamaguchi, K., Empante, T. A., Valentin, M. D., Gomez, M., Berges, A. J., Stecklein, G., Rumyantsev, S., Martinez, J., Balandin, A. A. & Bartels, L. High-Vacuum Particulate-Free Deposition of Wafer-Scale Mono-, Bi-, and Trilayer Molybdenum Disulfide with Superior Transport Properties. *ACS Applied Materials & Interfaces* **10**, 33457–33463. doi:10.1021/acsami.8b10857 (2018).
 42. Chen, J., Zhao, X., Tan, S. J. R., Xu, H., Wu, B., Liu, B., Fu, D., Fu, W., Geng, D., Liu, Y., Liu, W., Tang, W., Li, L., Zhou, W., Sum, T. C. & Loh, K. P. Chemical Vapor Deposition of Large-Size Monolayer MoSe₂ Crystals on Molten Glass. *Journal of the American Chemical Society* **139**, 1073–1076. doi:10.1021/jacs.6b12156 (2017).
 43. Kang, K., Xie, S., Huang, L., Han, Y., Huang, P. Y., Mak, K. F., Kim, C.-J., Muller, D. & Park, J. High-mobility three-atom-thick semiconducting films with wafer-scale homogeneity. *Nature* **520**, 656–660. doi:10.1038/nature14417 (2015).
 44. Lee, Y.-H., Zhang, X.-Q., Zhang, W., Chang, M.-T., Lin, C.-T., Chang, K.-D., Yu, Y.-C., Wang, J. T.-W., Chang, C.-S., Li, L.-J. & Lin, T.-W. Synthesis of Large-Area MoS₂ Atomic Layers with Chemical Vapor Deposition. *Advanced Materials* **24**, 2320–2325. doi:10.1002/adma.201104798 (2012).
 45. Tao, L., Chen, K., Chen, Z., Chen, W., Gui, X., Chen, H., Li, X. & Xu, J.-B. Centimeter-Scale CVD Growth of Highly Crystalline Single-Layer MoS₂ Film with Spatial Homogeneity and the Visualization of Grain Boundaries. *ACS Applied Materials & Interfaces* **9**, 12073–12081. doi:10.1021/acsami.7b00420 (2017).
 46. Wang, Q. H., Kalantar-Zadeh, K., Kis, A., Coleman, J. N. & Strano, M. S. Electronics and optoelectronics of two-dimensional transition metal dichalcogenides. *Nature Nanotechnology* **7**, 699–712. doi:10.1038/nnano.2012.193 (2012).
 47. Yore, A. E., Smithe, K. K. H., Jha, S., Ray, K., Pop, E. & Newaz, A. K. M. Large array fabrication of high performance monolayer MoS₂ photodetectors. *Applied Physics Letters* **111**, 043110. ISSN: 0003-6951. doi:10.1063/1.4995984 (2017).
 48. Kopp, C., Bernabé, S., Bakir, B. B., Fedeli, J., Orobtcouk, R., Schrank, F., Porte, H., Zimmermann, L. & Tekin, T. Silicon Photonic Circuits: On-CMOS Integration, Fiber Optical Coupling, and Packaging. *IEEE Journal of Selected Topics in Quantum Electronics* **17**, 498–509. ISSN: 1077-260X. doi:10.1109/JSTQE.2010.2071855 (2011).
 49. Weinberg, Z. A., Rubloff, G. W. & Bassous, E. Transmission, photoconductivity, and the experimental band gap of thermally grown Si O₂ films. *Physical Review B* **19**, 3107–3117. ISSN: 1098-0121. doi:10.1103/PhysRevB.19.3107 (1979).
 50. Yu, N. & Capasso, F. Flat optics with designer metasurfaces. *Nature Materials* **13**, 139–150. ISSN: 1476-1122. doi:10.1038/nmat3839 (2014).
-

51. Colburn, S., Zhan, A., Bayati, E., Whitehead, J., Ryou, A., Huang, L. & Majumdar, A. Broadband transparent and CMOS-compatible flat optics with silicon nitride metasurfaces [Invited]. *Optical Materials Express* **8**, 2330. doi:10.1364/OME.8.002330 (2018).
52. Lin, D., Fan, P., Hasman, E. & Brongersma, M. L. Dielectric gradient metasurface optical elements. *Science* **345**, 298–302. doi:10.1126/science.1253213 (2014).
53. Lu, B.-R., Chen, Y., Wang, S.-W., Huq, E., Rogers, E., Kao, T. S., Qu, X.-P., Liu, R. & Zheludev, N. I. A novel 3D nanolens for sub-wavelength focusing by self-aligned nanolithography. *Microelectronic Engineering* **87**, 1506–1508. ISSN: 01679317. doi:10.1016/j.mee.2009.11.064 (2010).
54. Rogers, E. T. F., Lindberg, J., Roy, T., Savo, S., Chad, J. E., Dennis, M. R. & Zheludev, N. I. A super-oscillatory lens optical microscope for subwavelength imaging. *Nature Materials* **11**, 432–435. ISSN: 1476-1122. doi:10.1038/nmat3280 (2012).
55. Wang, Q., Rogers, E. T. F., Gholipour, B., Wang, C.-M., Yuan, G., Teng, J. & Zheludev, N. I. Optically reconfigurable metasurfaces and photonic devices based on phase change materials. *Nature Photonics* **10**, 60–65. doi:10.1038/nphoton.2015.247 (2016).
56. Wuttig, M. & Yamada, N. Erratum: Phase-change materials for rewriteable data storage. *Nature Materials* **6**, 1004. ISSN: 1476-1122. doi:10.1038/nmat2077 (2007).
57. Lee, B.-S., Abelson, J. R., Bishop, S. G., Kang, D.-H., Cheong, B.-k. & Kim, K.-B. Investigation of the optical and electronic properties of Ge₂Sb₂Te₅ phase change material in its amorphous, cubic, and hexagonal phases. *Journal of Applied Physics* **97**, 093509. ISSN: 0038-5654. doi:10.1063/1.1884248 (2005).
58. Gholipour, B., Zhang, J., MacDonald, K. F., Hewak, D. W. & Zheludev, N. I. An All-Optical, non-volatile, Bidirectional, Phase-Change Meta-Switch. *Advanced Materials* **25**, 3050–3054. doi:10.1002/adma.201300588 (2013).
59. Morin, F. J. Oxides Which Show a Metal-to-Insulator Transition at the Neel Temperature. *Physical Review Letters* **3**, 34–36. doi:10.1103/PhysRevLett.3.34 (1959).
60. Kana Kana, J. B., Ndjaka, J. M., Vignaud, G., Gibaud, A. & Maaza, M. Thermally tunable optical constants of vanadium dioxide thin films measured by spectroscopic ellipsometry. *Optics Communications* **284**, 807–812. ISSN: 00304018. doi:10.1016/j.optcom.2010.10.009 (2011).
61. Bai, L., Li, Q., Corr, S. A., Meng, Y., Park, C., Sinogeikin, S. V., Ko, C., Wu, J. & Shen, G. Pressure-induced phase transitions and metallization in VO₂. *Physical Review B* **91**, 1. ISSN: 1098-0121. doi:10.1103/PhysRevB.91.104110 (2015).
62. Joushaghani, A., Kruger, B. A., Paradis, S., Alain, D. S., Aitchison, J. & Poon, J. K. S. Sub-volt broadband hybrid plasmonic-vanadium dioxide switches. *Applied Physics Letters* **102**, 061101. ISSN: 0003-6951. doi:10.1063/1.4790834 (2013).

-
63. Becker, M. F., Buckman, A. B., Walser, R. M., Lépine, T., Georges, P. & Brun, A. Femtosecond laser excitation dynamics of the semiconductor–metal phase transition in VO₂. *Journal of Applied Physics* **79**, 2404–2408. ISSN: 0038-5654. doi:10.1063/1.361167 (1996).
 64. Cavalleri, A., Dekorsy, T., Chong, H. H. W., Kieffer, J. C. & Schoenlein, R. W. Evidence for a structurally-driven insulator-to-metal transition in VO₂ : A view from the ultrafast timescale. *Physical Review B: Condensed Matter* **70**, 161102. ISSN: 0921-4526. doi:10.1103/PhysRevB.70.161102 (2004).
 65. Rini, M., Cavalleri, A., Schoenlein, R. W., López, R., Feldman, L. C., Haglund, R. F., Boatner, L. A. & Haynes, T. E. Photoinduced phase transition in VO₂ nanocrystals: ultrafast control of surface-plasmon resonance. *Optics Letters* **30**, 558. doi:10.1364/OL.30.000558 (2005).
 66. Jostmeier, T., Zimmer, J., Karl, H., Krenner, H. J. & Betz, M. Optically imprinted reconfigurable photonic elements in a VO₂ nanocomposite. *Applied Physics Letters* **105**, 071107. ISSN: 0003-6951. doi:10.1063/1.4893570 (2014).
 67. Zimmer, J., Wixforth, A., Karl, H. & Krenner, H. J. Ion beam synthesis of nano-thermochromic diffraction gratings with giant switching contrast at telecom wavelengths. *Applied Physics Letters* **100**, 231911. ISSN: 0003-6951. doi:10.1063/1.4728110 (2012).
 68. Jostmeier, T. *GaN- and VO₂-Based Nanostructures: Physics and Photonic Applications* Dissertation (Technische Universität Dortmund, Dortmund, Germany, 2016). 144 pp.
 69. Chang, T.-C., Cao, X., Bao, S.-H., Ji, S.-D., Luo, H.-J. & Jin, P. Review on thermochromic vanadium dioxide based smart coatings: from lab to commercial application. *Advances in Manufacturing* **6**, 1–19. ISSN: 2095-3127. doi:10.1007/s40436-017-0209-2 (2018).
 70. Granqvist, C. G. Recent progress in thermochromics and electrochromics: A brief survey. *Thin Solid Films* **614**, 90–96. ISSN: 00406090. doi:10.1016/j.tsf.2016.02.029 (2016).
 71. Sun, G., Cao, X., Zhou, H., Bao, S. & Jin, P. A novel multifunctional thermochromic structure with skin comfort design for smart window application. *Solar Energy Materials and Solar Cells* **159**, 553–559. ISSN: 09270248. doi:10.1016/j.solmat.2016.09.045 (2017).
 72. Zhou, Y., Cai, Y., Hu, X. & Long, Y. Temperature-responsive hydrogel with ultra-large solar modulation and high luminous transmission for “smart window” applications. *Journal of Materials Chemistry A* **2**, 13550–13555. ISSN: 2050-7488. doi:10.1039/C4TA02287D (2014).

73. Ke, Y., Balin, I., Wang, N., Lu, Q., Tok, A. I. Y., White, T. J., Magdassi, S., Abdulhalim, I. & Long, Y. Two-Dimensional SiO₂/VO₂ Photonic Crystals with Statically Visible and Dynamically Infrared Modulated for Smart Window Deployment. *ACS Applied Materials & Interfaces* **8**, 33112–33120. doi:10.1021/acsami.6b12175 (2016).
74. Cao, J., Fan, W., Zhou, Q., Sheu, E., Liu, A., Barrett, C. & Wu, J. Colossal thermal-mechanical actuation via phase transition in single-crystal VO₂ microcantilevers. *Journal of Applied Physics* **108**, 083538. ISSN: 0038-5654. doi:10.1063/1.3501052 (2010).
75. Karl, H. & Peyinghaus, S. C. Tailoring of the thermomechanical performance of VO₂ nanowire bimorph actuators by ion implantation. *Nuclear Instruments and Methods in Physics Research Section B: Beam Interactions with Materials and Atoms* **365**, 75–78. ISSN: 0168583X. doi:10.1016/j.nimb.2015.04.027 (2015).
76. Yang, Z. & Ramanathan, S. Breakthroughs in Photonics 2014: Phase Change Materials for Photonics. *IEEE Photonics Journal* **7**, 1–5. doi:10.1109/JPHOT.2015.2413594 (2015).
77. Rajendra Kumar, R. T., Karunagaran, B., Mangalaraj, D., Narayandass, S., Manoravi, P., Joseph, M. & Gopal, V. Pulsed laser deposited vanadium oxide thin films for uncooled infrared detectors. *Sensors and Actuators A: Physical* **107**, 62–67. ISSN: 09244247. doi:10.1016/S0924-4247(03)00233-4 (2003).
78. Strelcov, E., Lilach, Y. & Kolmakov, A. Gas Sensor Based on Metal-Insulator Transition in VO₂ Nanowire Thermistor. *Nano Letters* **9**, 2322–2326. doi:10.1021/nl900676n (2009).
79. Attwood, D. T., Sakdinawat, A. & Geniesse, L. *X-rays and extreme ultraviolet radiation. Principles and applications / David Attwood (University of California, Berkeley), Anne Sakdinawat (SLAC National Accelerator Laboratory) ; illustrations by Linda Geniesse* 2nd ed. ISBN: 1107062896 (Cambridge University Press, Cambridge, United Kingdom and New York, NY, 2016).
80. Lu, B.-R., Li, J.-X., Guo, H.-B., Gao, C., Huq, E., Qu, X.-P., Chen, Y. & Liu, R. Dielectric Fresnel zone plates on optical fibers for micro-focusing applications. *Microelectronic Engineering* **88**, 2650–2652. ISSN: 01679317. doi:10.1016/j.mee.2011.02.010 (2011).
81. Fuster, J. M., Candelas, P., Castiñeira-Ibáñez, S., Pérez-López, S. & Rubio, C. Analysis of Fresnel Zone Plates Focusing Dependence on Operating Frequency. *Sensors* **17**. doi:10.3390/s17122809 (2017).
82. Benameur, M. M., Radisavljevic, B., Héron, J. S., Sahoo, S., Berger, H. & Kis, A. Visibility of dichalcogenide nanolayers. *Nanotechnology* **22**, 125706. doi:10.1088/0957-4484/22/12/125706 (2011).
83. Manzeli, S., Ovchinnikov, D., Pasquier, D., Yazyev, O. V. & Kis, A. 2D transition metal dichalcogenides. *Nature Reviews Materials* **2**, 17033. doi:10.1038/natrevmats.2017.33 (2017).

-
84. Kuc, A., Zibouche, N. & Heine, T. Influence of quantum confinement on the electronic structure of the transition metal sulfide TS_2 . *Physical Review B: Condensed Matter* **83**, 245213. ISSN: 0921-4526. doi:10.1103/PhysRevB.83.245213 (2011).
 85. Jin, W., Yeh, P.-C., Zaki, N., Zhang, D., Sadowski, J. T., Al-Mahboob, A., van der Zande, A. M., Chenet, D. A., Dadap, J. I., Herman, I. P., Sutter, P., Hone, J. & Osgood, R. M. Direct Measurement of the Thickness-Dependent Electronic Band Structure of MoS_2 Using Angle-Resolved Photoemission Spectroscopy. *Physical Review Letters* **111**, 106801. doi:10.1103/PhysRevLett.111.106801 (2013).
 86. Zhu, Z. Y., Cheng, Y. C. & Schwingenschlögl, U. Giant spin-orbit-induced spin splitting in two-dimensional transition-metal dichalcogenide semiconductors. *Physical Review B: Condensed Matter* **84**, 153402. ISSN: 0921-4526. doi:10.1103/PhysRevB.84.153402 (2011).
 87. Funke, S., Miller, B., Parzinger, E., Thiesen, P., Holleitner, A. W. & Wurstbauer, U. Imaging spectroscopic ellipsometry of MoS_2 . *Journal of Physics: Condensed Matter* **28**, 385301. ISSN: 0953-8984. doi:10.1088/0953-8984/28/38/385301 (2016).
 88. Yazyev, O. V. & Kis, A. MoS_2 and semiconductors in the flatland. *Materials Today* **18**, 20–30. ISSN: 13697021. doi:10.1016/j.mattod.2014.07.005 (2015).
 89. Mak, K. F. & Shan, J. Photonics and optoelectronics of 2D semiconductor transition metal dichalcogenides. *Nature Photonics* **10**, 216–226. doi:10.1038/nphoton.2015.282 (2016).
 90. Li, X., Tao, L., Chen, Z., Fang, H., Li, X., Wang, X., Xu, J.-B. & Zhu, H. Graphene and related two-dimensional materials: Structure-property relationships for electronics and optoelectronics. *Applied Physics Reviews* **4**, 021306. doi:10.1063/1.4983646 (2017).
 91. Chernikov, A., Berkelbach, T. C., Hill, H. M., Rigosi, A., Li, Y., Aslan, O. B., Reichman, D. R., Hybertsen, M. S. & Heinz, T. F. Exciton Binding Energy and Nonhydrogenic Rydberg Series in Monolayer WS_2 . *Physical Review Letters* **113**, 076802. doi:10.1103/PhysRevLett.113.076802 (2014).
 92. Zhang, C., Johnson, A., Hsu, C.-L., Li, L.-J. & Shih, C.-K. Direct Imaging of Band Profile in Single Layer MoS_2 on Graphite: Quasiparticle Energy Gap, Metallic Edge States, and Edge Band Bending. *Nano Letters* **14**, 2443–2447. doi:10.1021/nl501133c (2014).
 93. Hill, H. M., Rigosi, A. F., Roquelet, C., Chernikov, A., Berkelbach, T. C., Reichman, D. R., Hybertsen, M. S., Brus, L. E. & Heinz, T. F. Observation of Excitonic Rydberg States in Monolayer MoS_2 and WS_2 by Photoluminescence Excitation Spectroscopy. *Nano Letters* **15**, 2992–2997. doi:10.1021/nl504868p (2015).

94. Klots, A. R., Newaz, A. K. M., Wang, B., Prasai, D., Krzyzanowska, H., Lin, J., Caudel, D., Ghimire, N. J., Yan, J., Ivanov, B. L., Velizhanin, K. A., Burger, A., Mandrus, D. G., Tolk, N. H., Pantelides, S. T. & Bolotin, K. I. Probing excitonic states in suspended two-dimensional semiconductors by photocurrent spectroscopy. *Scientific Reports* **4**, 6608. ISSN: 2045-2322. doi:10.1038/srep06608 (2014).
95. Goto, T., Kato, Y., Uchida, K. & Miura, N. Exciton absorption spectra of MoS₂ crystals in high magnetic fields up to 150 T. *Journal of Physics: Condensed Matter* **12**, 6719–6723. ISSN: 0953-8984. doi:10.1088/0953-8984/12/30/304 (2000).
96. Nam, S. B., Reynolds, D. C., Litton, C. W., Almassy, R. J., Collins, T. C. & Wolfe, C. M. Free-exciton energy spectrum in GaAs. *Physical Review B* **13**, 761–767. ISSN: 1098-0121. doi:10.1103/PhysRevB.13.761 (1976).
97. Ye, Z., Cao, T., O'Brien, K., Zhu, H., Yin, X., Wang, Y., Louie, S. G. & Zhang, X. Probing excitonic dark states in single-layer tungsten disulphide. *Nature* **513**, 214–218. doi:10.1038/nature13734 (2014).
98. Wurstbauer, U., Miller, B., Parzinger, E. & Holleitner, A. W. Light–matter interaction in transition metal dichalcogenides and their heterostructures. *Journal of Physics D: Applied Physics* **50**, 173001. ISSN: 0022-3727. doi:10.1088/1361-6463/aa5f81 (2017).
99. Mattheiss, L. F. Band Structures of Transition-Metal-Dichalcogenide Layer Compounds. *Physical Review B* **8**, 3719–3740. ISSN: 1098-0121. doi:10.1103/PhysRevB.8.3719 (1973).
100. Korn, T., Heydrich, S., Hirmer, M., Schmutzler, J. & Schüller, C. Low-temperature photocarrier dynamics in monolayer MoS₂. *Applied Physics Letters* **99**, 102109. ISSN: 0003-6951. doi:10.1063/1.3636402 (2011).
101. Rigosi, A. F., Hill, H. M., Li, Y., Chernikov, A. & Heinz, T. F. Probing Inter-layer Interactions in Transition Metal Dichalcogenide Heterostructures by Optical Spectroscopy: MoS₂/WS₂ and MoSe₂/WSe₂. *Nano Letters* **15**, 5033–5038. doi:10.1021/acs.nanolett.5b01055 (2015).
102. Castellanos-Gomez, A., Buscema, M., Molenaar, R., Singh, V., Janssen, L., van der Zant, H. S. J. & Steele, G. A. Deterministic transfer of two-dimensional materials by all-dry viscoelastic stamping. *2D Materials* **1**, 011002. doi:10.1088/2053-1583/1/1/011002 (2014).
103. Coleman, J. N., Lotya, M., O'Neill, A., Bergin, S. D., King, P. J., Khan, U., Young, K., Gaucher, A., De, S., Smith, R. J., Shvets, I. V., Arora, S. K., Stanton, G., Kim, H.-Y., Lee, K., Kim, G. T., Duesberg, G. S., Hallam, T., Boland, J. J., Wang, J. J., Donegan, J. F., Grunlan, J. C., Moriarty, G., Shmeliov, A., Nicholls, R. J., Perkins, J. M., Grieveson, E. M., Theuwissen, K., McComb, D. W., Nellist, P. D. & Nicolosi, V. Two-Dimensional Nanosheets Produced by Liquid Exfoliation of Layered Materials. *Science* **331**, 568–571. doi:10.1126/science.1194975 (2011).

-
104. Kelly, A. G., Hallam, T., Backes, C., Harvey, A., Esmaily, A. S., Godwin, I., Coelho, J., Nicolosi, V., Lauth, J., Kulkarni, A., Kinge, S., Siebbeles, L. D. A., Duesberg, G. S. & Coleman, J. N. All-printed thin-film transistors from networks of liquid-exfoliated nanosheets. *Science* **356**, 69–73. doi:10.1126/science.aal4062 (2017).
 105. Chhowalla, M., Shin, H. S., Eda, G., Li, L.-J., Loh, K. P. & Zhang, H. The chemistry of two-dimensional layered transition metal dichalcogenide nanosheets. *Nature Chemistry* **5**, 263–275. doi:10.1038/nchem.1589 (2013).
 106. Zeng, Z., Yin, Z., Huang, X., Li, H., He, Q., Lu, G., Boey, F. & Zhang, H. Single-Layer Semiconducting Nanosheets: High-Yield Preparation and Device Fabrication. *Angewandte Chemie (International ed. in English)* **50**, 11093–11097. doi:10.1002/anie.201106004 (2011).
 107. Mann, J., Sun, D., Ma, Q., Chen, J.-R., Preciado, E., Ohta, T., Diaconescu, B., Yamaguchi, K., Tran, T., Wurch, M., Magnone, K., Heinz, T. F., Kellogg, G. L., Kawakami, R. & Bartels, L. Facile growth of monolayer MoS₂ film areas on SiO₂. *The European Physical Journal B* **86**, 226. ISSN: 1434-6028. doi:10.1140/epjb/e2013-31011-y (2013).
 108. Miwa, J. A., Dendzik, M., Grønberg, S. S., Bianchi, M., Lauritsen, J. V., Hofmann, P. & Ulstrup, S. Van der Waals Epitaxy of Two-Dimensional MoS₂-Graphene Heterostructures in Ultrahigh Vacuum. *ACS Nano* **9**, 6502–6510. doi:10.1021/acsnano.5b02345 (2015).
 109. Joannopoulos, J. D. *Photonic Crystals. Molding the Flow of Light* 2nd ed. xiv, 286. ISBN: 0691124566 (Princeton University Press, Princeton, 2008).
 110. Zinth, W. & Zinth, U. *Optik : Lichtstrahlen – Wellen – Photonen* 2nd ed. 1 online resource. ISBN: 978-3486588019 (De Gruyter Oldenbourg, München, 2008).
 111. Saleh, B. E. A. & Teich, M. C. *Fundamentals of Photonics* 2nd ed. 1 online resource (1202. ISBN: 978-0-471-35832-9 (Wiley, Chichester, 2013).
 112. Kittel, C. *Introduction to Solid State Physics* 7th ed. 673 s. ISBN: 0471111813 (Wiley, New York, 1996).
 113. Fox, M. *Quantum Optics. An Introduction* xvii, 378. ISBN: 0198566735 (Oxford University Press, Oxford and New York, 2006).
 114. Pavarini, E., Andreani, L., Soci, C., Galli, M., Marabelli, F. & Comoretto, D. Band structure and optical properties of opal photonic crystals. *Physical Review B* **72**, 045102. ISSN: 1098-0121. doi:10.1103/PhysRevB.72.045102 (2005).
 115. Gross, R. & Marx, A. *Festkörperphysik* 1 online resource. ISBN: 978-3-486-71294-0 (De Gruyter Oldenbourg, München, 2012).
 116. Gong, Y. *Silicon-based Photonic, Plasmonic, and Optomechanic Devices* Dissertation (Stanford University, Stanford, California, 2010). 158 pp.

117. Mangold, H. M. *Positionsgenaue Ionenstrahlsynthese von CdSe Nanokristalliten und deren Kopplung an nanophotonische Resonatoren* Dissertation (Universität Augsburg, Augsburg, Germany, 2016). 145 pp.
118. Chen, Y.-J., Cain, J. D., Stanev, T. K., Dravid, V. P. & Stern, N. P. Valley-polarized exciton–polaritons in a monolayer semiconductor. *Nature Photonics* **11**, 431–435. doi:10.1038/nphoton.2017.86 (2017).
119. Lagarde, D., Bouet, L., Marie, X., Zhu, C. R., Liu, B. L., Amand, T., Tan, P. H. & Urbaszek, B. Carrier and polarization dynamics in monolayer MoS₂. *Physical Review Letters* **112**, 047401. doi:10.1103/PhysRevLett.112.047401 (2014).
120. Nag, J. & Haglund Jr, R. F. Synthesis of vanadium dioxide thin films and nanoparticles. *Journal of Physics: Condensed Matter* **20**, 264016. ISSN: 0953-8984. doi:10.1088/0953-8984/20/26/264016 (2008).
121. Goodenough, J. B. The Two Components of the Crystallographic Transition in VO₂. *Journal of Solid State Chemistry* **3**, 490–500. ISSN: 00224596. doi:10.1016/0022-4596(71)90091-0 (1971).
122. Qazilbash, M. M., Li, Z. Q., Podzorov, V., Brehm, M., Keilmann, F., Chae, B. G., Kim, H. T. & Basov, D. N. Electrostatic modification of infrared response in gated structures based on VO₂. *Applied Physics Letters* **92**, 241906. ISSN: 0003-6951. doi:10.1063/1.2939434 (2008).
123. Chae, B.-G., Kim, H.-T., Youn, D.-H. & Kang, K.-Y. Abrupt metal–insulator transition observed in VO₂ thin films induced by a switching voltage pulse. *Physica B: Condensed Matter* **369**, 76–80. ISSN: 09214526. doi:10.1016/j.physb.2005.07.032 (2005).
124. Lysenko, S., Rua, A. J., Vikhnin, V., Jimenez, J., Fernandez, F. & Liu, H. Light-induced ultrafast phase transitions in VO₂ thin film. *Applied Surface Science* **252**, 5512–5515. ISSN: 01694332. doi:10.1016/j.apsusc.2005.12.137 (2006).
125. Verleur, H. W., Barker, A. S. & Berglund, C. N. Optical Properties of VO₂ between 0.25 and 5 eV. *Physical Review* **172**, 788–798. ISSN: 0031-899X. doi:10.1103/PhysRev.172.788 (1968).
126. Gray, A. X., Jeong, J., Aetukuri, N. P., Granitzka, P., Chen, Z., Kukreja, R., Higley, D., Chase, T., Reid, A. H., Ohldag, H., Marcus, M. A., Scholl, A., Young, A. T., Doran, A., Jenkins, C. A., Shafer, P., Arenholz, E., Samant, M. G., Parkin, S. S. P. & Dürr, H. A. Correlation-Driven Insulator-Metal Transition in Near-Ideal Vanadium Dioxide Films. *Physical Review Letters* **116**, 116403. doi:10.1103/PhysRevLett.116.116403 (2016).
127. Eyert, V. The metal-insulator transitions of VO₂: A band theoretical approach. *Annalen der Physik* **11**, 650–704. ISSN: 00033804. doi:10.1002/1521-3889(200210)11:9<650::AID-ANDP650>3.0.CO;2-K (2002).

-
128. Rafe, K. *Influence of Implantation Energy and Fluence on Vanadium (IV) Oxide Nano-Cluster Size and Semiconductor to Metal Transition* Master's thesis (Augsburg University, Augsburg, Germany, 2011). 67 pp.
129. Appavoo, K., Lei, D. Y., Sonnefraud, Y., Wang, B., Pantelides, S. T., Maier, S. A. & Haglund, R. F. Role of Defects in the Phase Transition of VO₂ Nanoparticles Probed by Plasmon Resonance Spectroscopy. *Nano Letters* **12**, 780–786. doi:10.1021/nl203782y (2012).
130. Jostmeier, T., Mangold, M., Zimmer, J., Karl, H., Krenner, H. J., Ruppert, C. & Betz, M. Thermochromic modulation of surface plasmon polaritons in vanadium dioxide nanocomposites. *Optics Express* **24**, 17321–17331. ISSN: 1094-4087. doi:10.1364/OE.24.017321 (2016).
131. Zimmer, J. *Nanothermochrome optische Elemente auf Basis Ionenstrahl-synthetisierter Vanadiumdioxid Nanokristallite* Dissertation (Universität Augsburg, Augsburg, Germany, 2016). 120 pp.
132. Bass, M., van Stryland, E. W., Williams, D. R. & Wolfe, W. L. *Handbook of Optics* 2nd ed. 4 bd. ISBN: 0-07-047740-7 (McGraw-Hill, New York and London, 1995).
133. Sussman, M. Elementary Diffraction Theory of Zone Plates. *American Journal of Physics* **28**, 394–398. ISSN: 0002-9505. doi:10.1119/1.1935811 (1960).
134. Hecht, E. *Optics* 4th Intern. ed. VI, 698 Seiten. ISBN: 0-321-18878-0 (Addison-Wesley, San Francisco, 2010).
135. Yee, K. S. Numerical Solution of Initial Boundary Value Problems Involving Maxwell's Equations in Isotropic Media. *IEEE Transactions on Antennas and Propagation* **14**, 302–307. ISSN: 0018-926X. doi:10.1109/TAP.1966.1138693 (1966).
136. Taflove, A. & Hagness, S. C. *Computational electrodynamics. The finite-difference time-domain method* 3rd ed. XXII, 1006 Seiten. ISBN: 978-1580538320 (Artech House, Boston, Mass., 2005).
137. Lumerical Inc. *Quality factor calculations* https://apps.lumerical.com/diffractive_optics_cavity_q_calculation.html (2019).
138. Sun, L., Leong, W. S., Yang, S., Chisholm, M. F., Liang, S.-J., Ang, L. K., Tang, Y., Mao, Y., Kong, J. & Yang, H. Y. Concurrent Synthesis of High-Performance Monolayer Transition Metal Disulfides. *Advanced Functional Materials* **27**, 1605896. ISSN: 1616301X. doi:10.1002/adfm.201605896 (2017).
139. Bilgin, I., Liu, F., Vargas, A., Winchester, A., Man, M. K. L., Upmanyu, M., Dani, K. M., Gupta, G., Talapatra, S., Mohite, A. D. & Kar, S. Chemical Vapor Deposition Synthesized Atomically Thin Molybdenum Disulfide with Optoelectronic-Grade Crystalline Quality. *ACS Nano* **9**, 8822–8832. doi:10.1021/acs.nano.5b02019 (2015).
140. Bhushan, B. *Springer Handbook of Nanotechnology* xxxvi, 1222. ISBN: 3540012184 (Springer, Berlin and London, 2004).
-

141. Zeon Corporation. *ZEP520A Technical Report. High Resolution Positive Electron Beam Resist* version Ver.1.01. ZEONREX Electronic Chemicals, 2003.
142. *Handbook of Microlithography, Micromachining, and Microfabrication. Volume 1: Microlithography* (ed Rai-Choudhury, P.) Rai-Choudhury, P., (editor.) (SPIE Optical Engineering Press, Bellingham, Washington, 1997). 1 online resource (viii, 768. ISBN: 9781510607965).
143. Raith GmbH. *NanoPECSTM Software Description* version Version 1.0. Dortmund, Germany: Raith GmbH, 2008.
144. Raith GmbH. *e_LINE (Version 5.0 SP 15.2). Ultra-High Resolution E-Beam Lithography and Nanoengineering Workstation* Dortmund, Germany, 2007.
145. Stevens, L., Jonckheere, R., Froyen, E., Decoutere, S. & Lanneer, D. Determination of the proximity parameters in electron beam lithography using doughnut-structures. *Microelectronic Engineering* **5**, 141–150. ISSN: 01679317. doi:10.1016/0167-9317(86)90040-7 (1986).
146. CORIAL. *Inductively Coupled Plasma – Reactive Ion Etching (ICP-RIE)* <https://www.corial.com/en/technologies/icp-rie-inductively-coupled-plasma-reactive-ion-etching/> (2019).
147. Winters, H. F. & Coburn, J. W. The etching of silicon with XeF₂ vapor. *Applied Physics Letters* **34**, 70–73. ISSN: 0003-6951. doi:10.1063/1.90562 (1979).
148. SPTS Technologies Ltd. *XeF₂ Etch for MEMS Release. Application Brief* 2016. <https://www.orbotech.com/assets/media/xef2-intro-usletter-q1-16.pdf>.
149. Veyan, J.-F., Aureau, D., Gogte, Y., Campbell, P., Yan, X.-M. & Chabal, Y. J. Comparative time-resolved study of the XeF₂ etching of Mo and Si. *Journal of Applied Physics* **108**, 114913. ISSN: 0038-5654. doi:10.1063/1.3520653 (2010).
150. Huang, Y., Wu, J., Xu, X., Ho, Y., Ni, G., Zou, Q., Koon, G. K. W., Zhao, W., Castro Neto, A. H., Eda, G., Shen, C. & Özyilmaz, B. An innovative way of etching MoS₂: Characterization and mechanistic investigation. *Nano Research* **6**, 200–207. ISSN: 1998-0124. doi:10.1007/s12274-013-0296-8 (2013).
151. Karl, H., Großhans, I. & Stritzker, B. Combinatorial ion beam synthesis of semiconductor nanoclusters. *Measurement Science and Technology* **16**, 32–40. ISSN: 0957-0233. doi:10.1088/0957-0233/16/1/005 (2005).
152. Ziegler, J. F. *SRIM - The Stopping and Range of Ions in Matter* 2013. www.srim.org.
153. Fox, M. *Optical Properties of Solids XII*, 305 str. ISBN: 0198506139 (Oxford University Press, Oxford, 2001).
154. Gywat, O., Berezovsky, J. & Krenner, H. J. *Spins in Optically Active Quantum Dots. Concepts and methods* 1 online resource (x, 209. ISBN: 978-3-527-40806-1. doi:10.1002/9783527611065. <http://site.ebrary.com/lib/alltitles/docDetail.action?docID=10303753> (Wiley-VCH, Weinheim, 2010).

-
155. Bae, J. J., Jeong, H. Y., Han, G. H., Kim, J., Kim, H., Kim, M. S., Moon, B. H., Lim, S. C. & Lee, Y. H. Thickness-dependent in-plane thermal conductivity of suspended MoS₂ grown by chemical vapor deposition. *Nanoscale* **9**, 2541–2547. doi:10.1039/c6nr09484h (2017).
156. Miller, B., Parzinger, E., Vernickel, A., Holleitner, A. W. & Wurstbauer, U. Photogating of mono- and few-layer MoS₂. *Applied Physics Letters* **106**, 122103. ISSN: 0003-6951. doi:10.1063/1.4916517 (2015).
157. Klein, J., Kuc, A., Nolinder, A., Altzschner, M., Wierzbowski, J., Sigger, F., Kreppl, F., Finley, J. J., Wurstbauer, U., Holleitner, A. W. & Kaniber, M. Robust Valley Polarization of Helium Ion Modified Atomically Thin MoS₂. *2D Materials* **5**, 011007. doi:10.1088/2053-1583/aa9642 (2018).
158. Yu, P. Y. & Cardona, M. *Fundamentals of Semiconductors. Physics and Materials Properties* 1. ed., corr. print. XIV, 617 Seiten. ISBN: 3540583076 (Springer, Berlin, 1996).
159. Molina-Sánchez, A. & Wirtz, L. Phonons in single-layer and few-layer MoS₂ and WS₂. *Physical Review B* **84**. ISSN: 1098-0121. doi:10.1103/PhysRevB.84.155413 (2011).
160. Uchinokura, K., Sekine, T. & Matsuura, E. Raman Scattering by Silicon. *Solid State Communications* **11**, 47–49. doi:10.1016/0038-1098(72)91127-1 (1972).
161. Schilbe, P. Raman scattering in VO₂. *Physical Review B: Condensed Matter* **316-317**, 600–602. ISSN: 0921-4526. doi:10.1016/S0921-4526(02)00584-7 (2002).
162. Pan, M., Liu, J., Zhong, H., Wang, S., Li, Z.-f., Chen, X. & Lu, W. Raman study of the phase transition in VO₂ thin films. *Journal of Crystal Growth* **268**, 178–183. ISSN: 00220248. doi:10.1016/j.jcrysgro.2004.05.005 (2004).
163. Czaplewski, D. A., Tallant, D. R., Patrizi, G. A., Wendt, J. R. & Montoya, B. Improved etch resistance of ZEP 520A in reactive ion etching through heat and ultraviolet light treatment. *Journal of Vacuum Science & Technology B: Microelectronics and Nanometer Structures* **27**, 581–584. ISSN: 10711023. doi:10.1116/1.3086721 (2009).
164. Guilmain, M., Jaouad, A., Ecoffey, S. & Drouin, D. SiO₂ shallow nanostructures ICP etching using ZEP electroresist. *Microelectronic Engineering* **88**, 2505–2508. ISSN: 01679317. doi:10.1016/j.mee.2011.02.032 (2011).
165. Rivera, P., Schaibley, J. R., Jones, A. M., Ross, J. S., Wu, S., Aivazian, G., Klement, P., Seyler, K., Clark, G., Ghimire, N. J., Yan, J., Mandrus, D. G., Yao, W. & Xu, X. Observation of long-lived interlayer excitons in monolayer MoSe₂-WSe₂ heterostructures. *Nature Communications* **6**, 6242. doi:10.1038/ncomms7242 (2015).
166. Kapfinger, S., Reichert, T., Lichtmannecker, S., Müller, K., Finley, J. J., Wixforth, A., Kaniber, M. & Krenner, H. J. Dynamic acousto-optic control of a strongly coupled photonic molecule. *Nature Communications* **6**, 8540. doi:10.1038/ncomms9540 (2015).
-

167. Rivoire, K., Buckley, S. & Vučković, J. Multiply resonant photonic crystal nanocavities for nonlinear frequency conversion. *Optics Express* **19**, 22198–22207. ISSN: 1094-4087. doi:10.1364/OE.19.022198 (2011).
168. Petzak, T. M. *Siliziumdioxid-basierte photonische Nanoresonatoren mit maßgeschneiderten Polarisations-eigenschaften* Master's Thesis (Universität Augsburg, Augsburg, Germany, 2017). 79 pp.
169. Varshni, Y. P. Temperature dependence of the energy gap in semiconductors. *Physica* **34**, 149–154. ISSN: 00318914. doi:10.1016/0031-8914(67)90062-6 (1967).
170. Dey, P., Paul, J., Wang, Z., Stevens, C. E., Liu, C., Romero, A. H., Shan, J., Hilton, D. J. & Karaickaj, D. Optical Coherence in Atomic-Monolayer Transition-Metal Dichalcogenides Limited by Electron-Phonon Interactions. *Physical Review Letters* **116**, 127402. doi:10.1103/PhysRevLett.116.127402 (2016).
171. Schuller, J. A., Karaveli, S., Schiros, T., He, K., Yang, S., Kymissis, I., Shan, J. & Zia, R. Orientation of luminescent excitons in layered nanomaterials. *Nature Nanotechnology* **8**, 271–276. doi:10.1038/nnano.2013.20 (2013).

Acronyms

1D one-dimensional

2D two-dimensional

3D three-dimensional

Ar argon

ARPES angle-resolved photoemission spectroscopy

CB conduction band

CdSe cadmium selenide

CHF₃ fluoroform

CO₂ carbon dioxide

CVD chemical vapor deposition

DBR distributed Bragg reflector

DC direct current

DOS density of states

DS directly synthesized

e-beam electron beam

eV electron volt

FDTD finite-difference time-domain

FFT fast Fourier transform

FWHM full width at half maximum

FZP Fresnel zone plate

GaAs gallium arsenide

Ge germanium

GST germanium antimony telluride

HCl hydrochloric acid

IPA	isopropyl alcohol
LED	light-emitting diode
MIBK	methyl isobutyl ketone
MIT	metal-insulator transition
Mo	molybdenum
MoO₂	molybdenum dioxide
MoS₂	molybdenum disulfide
MoSe₂	molybdenum diselenide
MoTe₂	molybdenum telluride
NA	numerical aperture
ND	neutral density
PCC	photonic crystal cavity
PL	photoluminescence
PML	perfectly matched layer
PMMA	polymethyl methacrylate
<i>Q</i>-factor	quality factor
ICP-RIE	inductively coupled plasma reactive ion etching
RTA	rapid thermal annealing
S	sulfur
SD	selectively deactivated
Se	selenium
SEM	scanning electron microscope
Si	silicon
SiN	silicon nitride
SiO₂	silicon dioxide
SO₂	sulfur dioxide
SPAD	single photon avalanche diode
Te	tellurium
TE	transverse-electric

TEM transmission electron microscope

TMD transition metal dichalcogenide

μ -PL micro-photoluminescence

VB valence band

vdW van-der-Waals

VO₂ vanadium dioxide

W tungsten

WS₂ tungsten disulfide

WSe₂ tungsten diselenide

WTe₂ tungsten telluride

XeF₂ xenon difluoride

ZEP ZEP-520A

Acknowledgments

Finally, I would like to thank all the people that have contributed to this work by both intellectually and mentally supporting me over the last few years. In particular, I want to thank

- Hubert Krenner for giving me the opportunity to write this theses and supporting me in every situation
- Helmut Karl for the great collaboration in the topic of ion implantation and Wolfgang Brückner for fabricating the VO₂ nanocluster samples
- Achim Wixforth for fruitful conversations - about science, the past and the future
- Ludwig Bartels and the members of his group - in particular, Michelle Wurch, Edwin Preciado, Kortney Almeida, Koichi Yamaguchi, Ariana Nguyen, Sahar Naghibi Alvillar, Velveth Klee, David Barroso, Dominic Martinez-Ta, and Daniel Lu - for constant supply of CVD-grown TMD samples, for their hospitality, and for my wonderful stays in California
- Moritz Mangold for introducing me into the secrets of photonic crystal fabrication
- Tobias Petzak and Anna-Lena Jäger for providing measurement data and their support during their Master's and Bachelor's theses
- the rest of the Hoobgroup: Lisa Janker, Emeline Nysten, Matthias Weiß, Max Sonner, Benjamin Mayer, and (of course) Alexander Hupfer for enlightening intra- and inter-office conversations and unforgettable activities
- Andreas Hörner, Sidonie Lieber, Adrian Mainka, Olga Ustinov, and Andreas Spörhase for helping out in every stressful situation that occurs whenever PhD students work with complex machines and dangerous chemicals
- Funda Cevic for caring of all organization issues and a great karaoke partner
- all the chair members of EP1 - working at EP1 was an extraordinary experience including legendary chair seminars, rafting on the Olympic track or the countless informal discussions in the coffee room
- last, but not least, Annette Hammer and Stefan Münch as well as my parents Claudia and Rainer Hammer for giving me support in so many ups and downs. It always feels good to come home.

I thank Nanosystems Initiative Munich (NIM), the Bavaria California Technology Center (BaCaTeC) and the Deutsche Forschungsgemeinschaft (DFG) for their financial support.